A Search for the Charged Higgs: Using Tau Polarimetry with Proton-Proton Collisions at the ATLAS Detector

A Dissertation

Presented to the Faculty of the Graduate School

of

Yale University

in Candidacy for the Degree of

Doctor of Philosophy

by

Susie Bedikian

Dissertation Director: Dr. Sarah Demers

March 2013

Acknowledgements

First and foremost, I would like to thank my colleagues for many fruitful discussions and generous technical and conceptual support throughout my graduate years at ATLAS. To George Lewis, Josh Cogan, Dan Guest, and Larry Lee; their patience and excitement for the field leave me indebted to their kindness. I thank Jake Searcy, Allison McCarn, Jen Godfrey, and Noel Dawe for having the collaborative spirit that is refreshing in this field. The physics results presented in this thesis would not have been possible without their collaboration. I look forward to following their accomplishments in science and beyond.

I extend my deepest gratitude to Sarah Demers for her encouragement and mentorship. She has provided me with so many great opportunities to grow as a scientist.

I thank Max Scherzer for his pedagogical ways. His coaching and tireless efforts to make me the best physicist I could become leave me in complete admiration.

My lifelong friendships have bestowed me a lifetime of treasured memories. I thank Emily and Jaime for our quests of adventure. I am grateful to have Christine, Emma, and Markie; they are my sisters at heart.

Most warmly I thank Eitan for profoundly shaping the person that I am and for believing in my talent. Thy eternal summer shall not fade.

Finally, I thank my grandparents and courageous parents for teaching me the value of grit, dedication, and above all, exceptional kindness.

Abstract

A Search for the Charged Higgs: Using Tau Polarimetry with Proton-Proton Collisions at the ATLAS Detector

Susie Bedikian

March 2013

A search for a 130 GeV charged Higgs boson $H^{\pm}$ in $t\bar{t}$ events containing a τ lepton is presented. Tau polarimetry is used in order to distinguish the signal, t $\rightarrow H^{\pm}b \rightarrow \tau\nu_{\tau}b$, from the dominant Standard Model background, t $\rightarrow W^{\pm}b \rightarrow \tau\nu_{\tau}b$. The signal extraction is performed by a log-likelihood template fit. The dataset corresponds to an integrated luminosity of 4.6 fb^{-1} of $\sqrt{s}$ =7 TeV proton-proton collisions collected with the ATLAS detector in 2011 at the Large Hadron Collider. Assuming the $H^{\pm}$ decays exclusively to $\tau\nu_{\tau}$, a limit is placed on the $BR(t \rightarrow H^{\pm}b)$ of less than 16% at the 95% confidence level. This is the first search for physics beyond the Standard Model to use τ polarimetry at a hadron collider.

To my loving parents

Contents

List of Tables

List of Figures

Measure what is measurable, and make measurable what is not so.

-G. Galilei

Chapter 1

Introduction

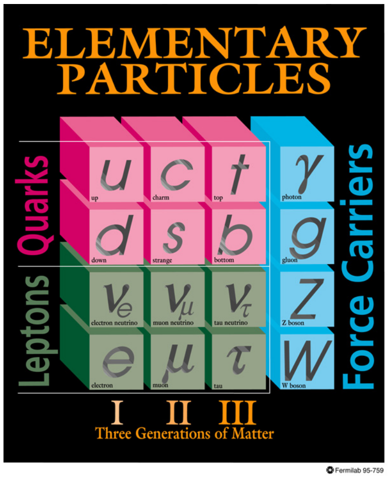

Figure 1.1: Particle content of the Standard Model, including 3 generations of quarks and leptons, and gauge bosons as force carriers of Electromagnetic (photons), Weak (W and Z bosons), and Strong (gluons) interactions.

Particle physics is the study of the basic structure of nature. It attempts to describe the most elementary constituents of matter and their fundamental interactions. This thesis demonstrates a new method to place limits on these allowed interactions and constituents beyond what has already been experimentally observed.

The technique employs information previously underdeveloped by physicists: spin effects in processes with τs in the final state. Tau polarimetry is a long-understood technique but has not been employed at hadron colliders, where a new variable was necessary to extract the information. Tau polarimetry at hadron colliders is an area of research that is not yet fully explored and can extend the physics reach of the Large Hadron Collider.

Tau polarimetry is possible because τs decay in the detector. They are the only leptons to do so. The energy distributions of their decay products depend on the helicity of the parent τ. Furthermore, τ polarization can be measured with a single observable that provides a powerful analysis tool.

The Standard Model, Figure 1.1, has withstood rigorous testing but leaves some unresolved questions in particle physics. Beyond the Standard Model searches for theoretically-motivated extensions, such as SUperSYmmetry (SUSY), are therefore important to explore.

How do physicists go about doing a SUSY search? Usual searches involve high-multiplicity jet signatures or searches for large amounts of missing energy. However this thesis uses another approach; probing the extended Higgs sector for evidence of SUSY, the charged Higgs. This thesis looks within $t\bar{t}$ events for a charged scalar, rather than looking at production directly from the hard scatter, due to the key property that the Higgs sector couples to mass.

ATLAS has placed strong limits on a charged Higgs based on event yields in a kinematic parameter space defined by p_T and missing E_T. This thesis develops an orthogonal method, which can be used in conjunction with current techniques.

Chapter 2 details the theoretical motivation of the charged Higgs search. Chapters 3, 4 and 5 describe the experimental techniques and identification methods that make such a search possible. Chapter 6 develops a powerful multivariate discriminant between electrons and τs used in this analysis. Finally, Chapters 7 and 8 describe this new use of τ polarimetry at ATLAS.

Chapter 2

Particle Physics and the Standard Model

2.1 The Standard Model

The Standard Model(SM) is a robust theory categorizing and relating fundamental constituents of matter and their interactions. In some ways it is to High Energy Physics what the Periodic Table of Elements is to chemistry.

The Standard Model has 58 elementary particles that come in the flavors of fermions, with $\frac{1}{2}$-integer spin, and bosons, with integer spin. The SM divides fermionic matter into two types: quarks and leptons [1]. The forces that exist between particles are mediated by gauge bosons. Of the four known fundamental forces, three are encompassed by the SM: the Strong force, the Weak force and the Electromagnetic force. These are shown along with their relative strengths in Table 2.1. Table 2.2 gives some properties of the six quark flavors. Table 2.3 gives some properties of the charged leptons. The three generations of neutral leptons, the neutrinos, are not shown in the table as the mixing between generations is significantly large. This large mixing results in the mass eigenstates being different than the flavor eigenstates. The MNS matrix quantifies the mixing between the three neutrino generations and is explained in further detail in [3].

Interaction	Theory	Relative Strength	Mediator	Range (m)
Strong	QCD	1	g_i, $i \in 1, ..., 8$	10^{-15}
Electromagnetic	QED	10^{-3}	γ	∞
Weak	Electroweak Theory	10^{-14}	$W^{\pm}, Z$	10^{-18}
Gravity	Relativity	10^{-43}	graviton*	∞

Table 2.1: Properties of the four fundamental forces and associated bosons. Note that the strengths of these interactions are variable and have multiple dependencies; values of the strengths are approximate. This table provides the average values at low energies. All the force mediators have spin=1 except for the hypothesized graviton which has spin=2. All the force mediators are electrically neutral except for the $W^{\pm}$ bosons which have charge $\pm 1e$ [1].

Quark	Electric Charge	Mass
up	$+\frac{2}{3}$e	$2.3^{+0.7}_{-0.5}$ MeV
down	$-\frac{1}{3}$e	3.2-4.4 MeV
strange	$-\frac{1}{3}$e	95±5 MeV
charm	$+\frac{2}{3}$e	1.275±0.025 GeV
bottom	$-\frac{1}{3}$e	4.65± 0.03 GeV
top	$+\frac{2}{3}$e	173.5±0.6±0.8 GeV

Table 2.2: The table shows the six quark flavors, their electric charge, and their mass. Each quark has a corresponding anti-quark with the opposite electric charge. These quarks are seen in nature in color-neutral combinations. All values are from the 2012 Particle Data Group [2].

Lepton	Electric Charge	Mass	Mean Lifetime	Lepton Number
e	-1e	0.511 MeV	stable	+1
μ	-1e	105.7 MeV	2.2 10^{-6} s	+1
τ	-1e	1.777 GeV	2.9 $10^{-}13$ s	+1

Table 2.3: Properties of the three generations of charged leptons are shown in this table. The anti-particles of these leptons have opposite electric charge and lepton number L = -1 [1, 3].

Interactions within the SM fundamentally conserve a number of quantities:

- Electric charge
- Energy: is conserved globally. Energy conservation can be temporarily violated within loops of Feynman diagrams.
- Flavor: is conserved in Electromagnetic and Strong-nuclear forces. Flavor-changing neutral currents are suppressed in interactions mediated with a Z boson, and allowed in interactions mediated with a W boson.
- Lepton Number, L: All leptons have L = +1 and all anti-leptons have $L = -1$. This can be further subdivided by flavor, so that there is a lepton number L_i for i $\in$ { e, μ, τ}, with each lepton number conserved.
- Baryon Number, B: All baryons have B = +1 and all anti-baryons have $B = -1$. Mesons have B = 0. Proton decay is forbidden as a result of the conservation of Baryon number.
- Color: each strong interaction vertex must be color-neutral.

2.1.1 Quantum Electrodynamics and the Weak Force

The Electromagnetic force is described by Quantum Electrodynamics (QED). The fundamental vertex of QED, which can be used to describe all interactions in Electromagnetism, is shown in Figure 2.1.

The Weak force, mediated by the $W^{\pm}$, Z bosons, is responsible for some radioactive decays of atomic particles and for β decay. The W boson, important in the context of this thesis, decays to 9 final states each with roughly equal branching ratio, as shown in Table 2.4.

A phenomenological aspect of the Weak force is that unlike other forces it does not produce bound states. In contrast, gravity does so on an astronomical scale, the

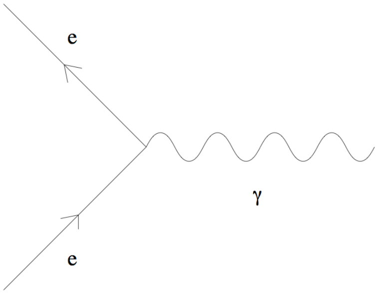

Figure 2.1: The Feynman diagram shows the fundamental vertex of QED, with time progressing from left to right. Shown is the diagram for an electron-positron pair, but any same-flavored quark-antiquark pair or same generation lepton-antilepton pair could replace the electron-positron in this diagram [3].

Process	Branching Ratio
W → $e\nu_e$	10.8±0.1 %
W → $\mu\nu_\mu$	10.6±0.2 %
W → $\tau\nu_\tau$	11.2±0.2%
W → ud	11%, for each of the 3 color-anticolor pairings
W → cs	11%, for each of the 3 color-anticolor pairings

Table 2.4: The branching ratios of the 9 W decay possibilities [2]. Charge is conserved in all decays.

Electromagnetic force does so at the atomic level, and the Strong force does so inside nuclei and baryons.

At high energy scales, the Weak force appears at the same strength as the Electromagnetic force. At scales at or below the scale of the Z, the massiveness of the W and Z bosons reduce its observed strength. The force is short-ranged as a result of spontaneous symmetry breaking, by which the W and Z bosons acquire masses of 80.4 GeV and 91.2 GeV, respectively. This is the Glasow-Weinberg-Salam model and is described in detail in [1]. Because of the large mass of the W and Z bosons, processes via Weak decays occur on a longer time scale than those via Strong force interactions. For example, μ decay occurs in 10^{-6} s, whereas hadronization occurs on the order of 10^{-24}s.

2.1.2 Electroweak Unification

Electromagnetism and the Weak force merge to an integrated description, the SU(2)xU(1) gauge theory with hidden symmetry. This becomes evident at scales above 10^2 GeV. The special unitary group of order 2, SU(2), has dimension 3 so three degrees of freedom emerge from the symmetry: W_1, W_2, W_3. U(1) has dimension 1 and the degree of freedom emerging is B^0. The three W bosons of weak isospin and the single B^0 boson from weak hypercharge are the four gauge bosons that form the observable mediators of the Electroweak force, as shown in Table 2.1:

$$\begin{aligned} W^+ &= W_1 \\ W^- &= W_2 \\ Z &= W_3 \cos\theta_W - B^0 \sin\theta_W \\ \gamma &= W_3 \sin\theta_W + B^0 \cos\theta_W \end{aligned}$$

The angle θ_W is the weak mixing angle. The $W^{\pm}$ bosons have a different mass than the Z boson, because the charged bosons are eigenstates of electroweak unification while the Z is a rotation in the (B^0, W_3) plane. The mass of the Z boson is given as a function of the weak mixing angle: $M_Z = \frac{M_W}{\cos\theta_W}$.

2.1.3 Strong Force and Quantum Chromodynamics

The Strong force is described by Quantum Chromodynamics (QCD). The fundamental tree-level verticies of QCD are shown in Figure 2.2.

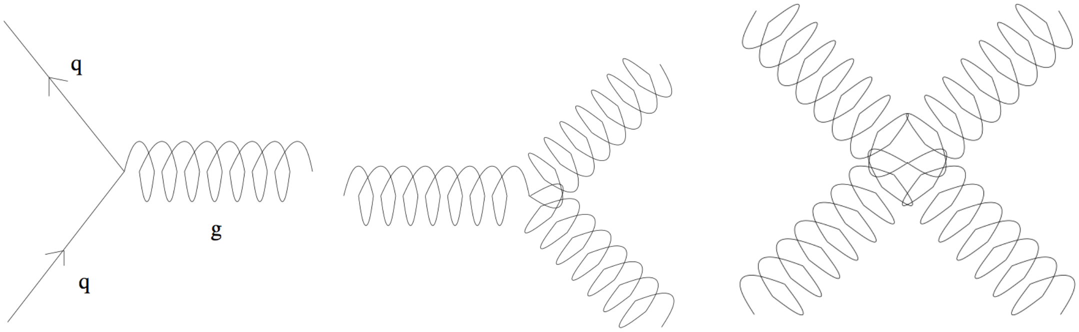

Figure 2.2: The Feynman diagrams show the fundamental verticies of QCD.

The gluons in QCD both mediate the force and carry color charge, the latter which results in gluon-gluon interactions [3, 17]. There are 8 color charge (red, green, blue) combinations of the gluon. The strength of the Strong force increases with distance, allowing free movement at short distance scales, which gives rise to asymptotic freedom. Due to confinement, if quarks are separated from each other, additional quarks emerge from the vacuum so that no bare quarks exist. A state called the quark-gluon plasma occurs when quarks can exist independently from each other [1]. Color charge and flavor are always conserved in QCD interactions. The discrete C (charge), P (parity), T (time), and CPT symmetries are also obeyed. A thorough description of this is in [17].

2.1.4 Successes and Shortcomings of the Standard Model

The Standard Model is a theory in agreement with almost all experimental results to date, and has repeatedly held up to rigorous experimental testing. However it may be an incomplete theory. Some of the phenomenological and theoretical limitations are listed:

- CP violation: CP violation in the SM is orders of magnitude too small to account for the matter-antimatter asymmetry of the Universe.

- Cosmology and Gravity: The particles in the SM comprise “baryonic matter” and make up less than 5% of the Universe. The SM does not explain the apparent 23% dark matter and 72% dark energy composition of the Universe.

- The Hierarchy problem: Quantum corrections to the Higgs boson mass result in quadratic divergences. An unnatural fine-tuned cancellation must be imposed to get $m_H \sim 10^2$ GeV instead of $m_H \sim \Lambda$, where Λ is the Planck scale on the order of 10^{19} GeV.

2.2 Charged Higgs and SUSY and MSSM

In light of the limitations of SM there have been alternative theories which serve to ameliorate some of these shortcomings. One such theory is SUperSYmmetry (SUSY). SUSY posits a super-partner boson for each fermion in the SM and vice versa; therefore every SM particle has a partner that has yet to be discovered. There are a number of variations of SUSY, one of which is the Minimal Supersymmetric Standard Model (MSSM). The charged Higgs particle exists within this theory and its observation would be evidence of physics beyond the Standard Model.

The MSSM is the minimal extension to SUSY in that the least number of extra particles must be added to the Standard Model. Since the MSSM has R-parity, the lightest supersymmetric superpartner particle is stable in the decay chain. The MSSM can provide a solution to the hierarchy problem in the Standard Model. If there are scalar particles with a symmetry that relate their couplings to the couplings of the standard fermions, the quadratic divergence to the Higgs boson mass disappears, and resolves the hierarchy problem. The Higgs boson mass is thus protected by this supersymmetry [4].

The MSSM has two doublets of complex scalar fields, rather than just the one in the ordinary Standard Model. The two complex Higgs doublets have opposite hypercharge and break electroweak symmetry. The two Higgs doublets result in five physical Higgs bosons after electroweak symmetry breaking: two neutral CP-even states h and H, one neutral CP-odd state A, and two charged scalars $H^{\pm}$. The tree-level MSSM Higgs sector can be entirely determined by $m_{H^{\pm}}$ and $\tan\beta$ [18]. The two doublets are described mathematically as:

$$H_1 = \begin{pmatrix} H_1^0 \\ H_1^- \end{pmatrix} \text{ with } Y_{H_1} = -1 \quad , \quad H_2 = \begin{pmatrix} H_2^+ \\ H_2^0 \end{pmatrix} \text{ with } Y_{H_2} = +1$$

Breaking electroweak symmetry also means breaking SUSY, as described in Section 1.2.1 of [4]. In SUSY this breaking occurs more naturally and elegantly than in the SM since only radiative corrections need to be applied in MSSM, while in the SM an unnatural choice of $\mu^2 < 0$ must be made after the matter.

The vacuum expectation values of the charged components of the two doublet Higgs fields, H_1^- and H_2^+, can be set to zero since the minimum value of the potential that satisfies $\frac{\partial V_H}{\partial H_2^+} = 0$ must also have H_1^-=0. The complement is also true: the minimum value of the potential that satisfies $\frac{\partial V_H}{\partial H_1^-} = 0$ must also have H_2^+=0. This means that at the minimum of the potential electromagnetism is unbroken, since the charged components of the Higgs scalars cannot get non-zero vacuum expectation values [19]. The neutral components of the two Higgs fields have vacuum expectation values given as:

$$\langle H_1^0 \rangle = \frac{v_1}{\sqrt{2}} \quad , \quad \langle H_2^0 \rangle = \frac{v_2}{\sqrt{2}}$$

From this definition, the ratio of the two vacuum expectation values can be defined, $\tan\beta \equiv \frac{\langle H_2^0 \rangle}{\langle H_1^0 \rangle} = \frac{v_2}{v_1}$. This useful parameter, $\tan\beta$, is referenced multiple times in this thesis, and its value has an impact on the final states and experimental techniques required to detect SUSY.

To calculate the masses of the MSSM Higgs bosons, first the scalar potential at the electroweak minimum is minimized with respect to each H_1^0 and H_2^0 : $\frac{\partial V_H}{\partial H_{1,2}^0} = 0$. The complete derivation is in [4].

The mass of the pseudoscalar CP-odd Higgs m_A is:

$$M_A^2 = -\bar{m}_3^2(\tan\beta + \cot\beta) = -\frac{2\bar{m}_3^2}{\sin 2\beta}$$

with $\bar{m}_3{}^2 \equiv B\mu$. $B\mu$ has been calculated previously by finding the minimum of the Higgs field and is:

$$B\mu = \frac{(m_{H_1}^2 - m_{H_2}^2)\tan 2\beta + M_Z^2 \sin 2\beta}{2}$$

The neutral CP-even MSSM Higgs bosons (H, h) are rotations of the mixing angle α of (H_1^0, H_2^0):

$$\begin{pmatrix} H \\ h \end{pmatrix} = \begin{pmatrix} \cos\alpha & \sin\alpha \\ -\sin\alpha & \cos\alpha \end{pmatrix} \begin{pmatrix} H_1^0 \\ H_2^0 \end{pmatrix}$$

where α is defined as:

$$\sin 2\alpha = -\sin 2\beta \frac{M_H^2 + M_h^2}{M_H^2 - M_h^2}$$

The masses of the neutral light CP-even Higgs, h, and the heavy CP-even Higgs, H, are functions of the parameters known or given above– the functional forms of M_A, M_Z, and β are given as:

$$M_{h,H}^2 = \frac{1}{2}\left[M_A^2 + M_Z^2 \mp \sqrt{(M_A^2 + M_Z^2)^2 - 4M_A^2 M_Z^2 \cos^2 2\beta}\right]$$

and the Charged Higgs masses are given as:

$$M_{H^\pm}^2 = M_A^2 + M_W^2$$

The branching ratios of the charged Higgs particles are shown in Figure 2.3 for two cases: low and high $\tan\beta$.

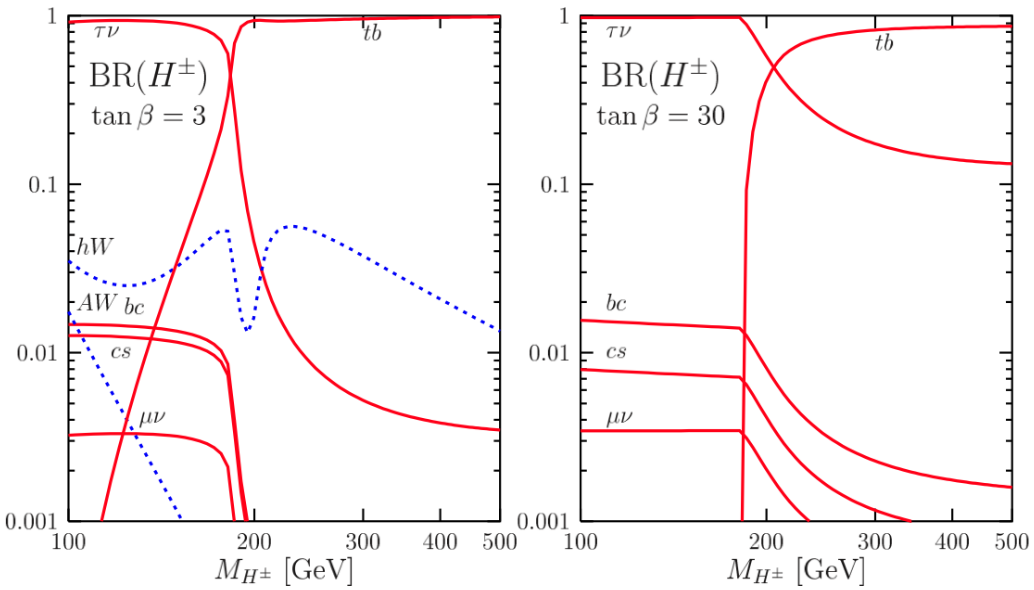

Figure 2.3: The decay branching ratios of the charged MSSM Higgs particles as a function of their mass for the two values $\tan\beta = 3$ (left) and $\tan\beta = 30$ (right) [4].

2.2.1 The effect of SM-like Higgs boson on the MSSM Higgs sector

In July 2012, both the ATLAS and CMS experiments at the LHC announced the discovery of a new boson consistent with a SM Higgs boson of mass, according to ATLAS, 126.0 ±0.4(statistical)±0.4(systematic) GeV with 5 σ significance. The observed signal was strongest in the Higgs to $\gamma\gamma$ and ZZ decay channels. The discovery of a boson at 126 GeV with a potential excess of H→ $\gamma\gamma$ events splits the MSSM Higgs parameter space into two regions.

In the "decoupling" region the neutral CP-even Higgs, h has a mass $m_h \approx 125$ GeV, and the other 4 MSSM Higgs (A,H,$H^\pm$) are all heavier [18].

The "non-decoupling" region specifies one of the MSSM Higgs masses $m_A \leq 130$ GeV. This region has the neutral light CP-even h and the neutral CP-odd state A nearly mass-degenerate and close to m_Z: $m_h \approx m_A \approxeq m_Z$. The two charged Higgs, $H^\pm$, and the neutral CP-even H are heavier and close to 125 GeV. The non-decoupling region is of interest in this thesis and is the one considered in [18].

If the MSSM theory is valid at the LHC the A,h,H MSSM bosons would be produced primarily via gluon fusion like so: gg → A,h,H , and the $H^{\pm}$ via top pair production: pp → $t\bar{t}$, where $t \rightarrow H^{\pm}b$. Much of the MSSM parameter space is excluded as a result of the 125 GeV SM-like Higgs boson discovery [5].

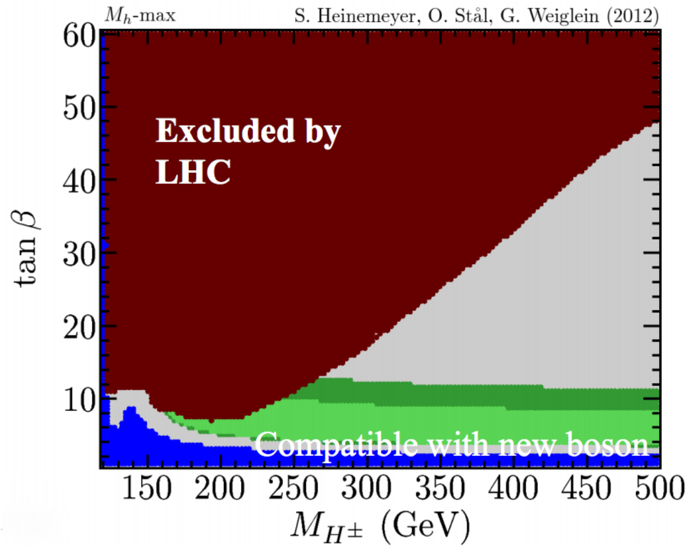

Figure 2.4: The parameter space of conservative lower limits on $\tan\beta$ as a function of $m_{H^{\pm}}$ is shown. The regions excluded by LEP are shown in blue. The regions excluded by the Tevatron and LHC experiments are in red. The gray area is the allowed parameter space before the July 2012 LHC results. The remaining green bands show the region where the m_h from the MSSM Higgs sector is compatible with the SM-like Higgs signal. The dark green band corresponds to a ±1 σ variation on the mass of the top quark. The parameters entered into the calculations of this figure hold for a general MSSM theory [5].

2.2.2 Limitations of MSSM

Though the introduction of the charged Higgs through SUSY theory is elegant, the area of SUSY and MSSM that can exist in a high $\tan\beta$ regime is heavily constrained.

In November 2012, the LHCb experiment at the LHC announced the latest results on the search for the decays of $B_s \rightarrow \mu^+\mu^-$ and found them to be consistent with SM expectation [20]. These rare decays are highly suppressed in the SM due to the suppression of flavor changing neutral currents, and as a result are sensitive to possible contributions from as-yet undiscovered particles. The $B_s \to \mu^+\mu^-$ amplitude is of order $\mathcal{O}(\tan\beta)^3$ and branching ratio is of order $\mathcal{O}(\tan\beta)^6$. Thus, the lack of an observed excess constrains $\tan\beta$ to low values.

2.3 Top Pair Production

At a proton-proton collider like the LHC and within the framework of the SM, top quarks are produced primarily through gluon fusion. The Feynman diagrams for the main processes are shown in Figure 2.5. The resultant top and anti-top quark pair produced is referred to as a $t\bar{t}$ event. The $t\bar{t}$ pair decays nearly instantaneously and the full $t\bar{t}$ cross section, $\sigma_{t\bar{t}}$, is 164.7 pb at next-to next-to leading order (NNLO) in perturbative QCD [2, 21].

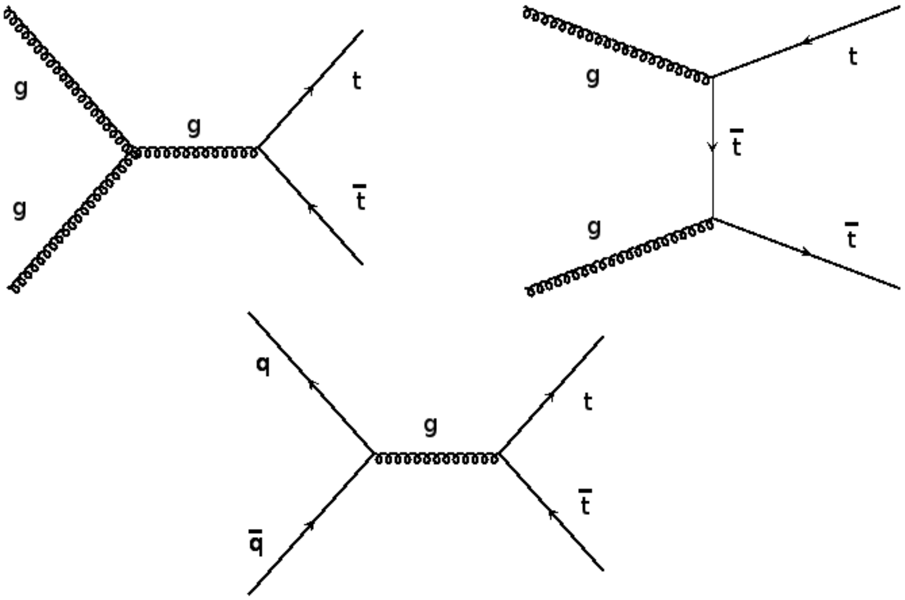

Figure 2.5: The dominant tree level diagrams for top production. Proton-proton collisions at the LHC result in initial-state modes with gluons preferred [6].

According to the Standard Model, the branching ratio BR($t \to Wb$)= 100%. Each W from the $t\bar{t}$ event can decay to three leptonic final states, W $\to l\nu_l$ with

$l \in \{e, \mu, \tau\}$ and 6 hadronic final states with W → q q'. Experimentally, the cases where the τ decays leptonically to lighter leptons belong to other signal lepton channels as they are difficult to separate from a direct $W \rightarrow e\nu_e$ $(\mu\nu_\mu)$ decay. The full set of top pair decay channels is shown in Figure 2.6.

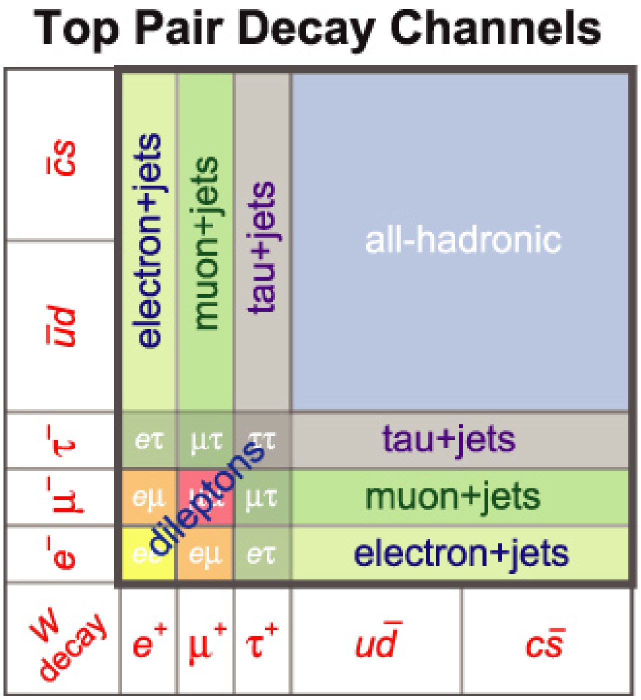

Figure 2.6: The full set of Standard Model top pair production channels

2.4 The Tau Lepton

The τ lepton was discovered at the Stanford Linear Accelerator [22], when center-of-mass energies reached 4 GeV, with the observation of:

> "sixty-four events of the form $e^+ + e^- \rightarrow e^\pm + \mu^\mp + \geq 2$ undetected particles for which we have no conventional explanation."

The explanation turned out to be an indirect detection of the third-generation lepton, the τ. The $e - \mu$ production were explained by $e^+ + e^- \rightarrow \tau^+ + \tau^-$ events followed by the near-immediate leptonic tau decays:

$$\tau^{\pm} \rightarrow e^{\pm}\nu_e\nu_\tau$$

$$\tau^{\mp} \rightarrow \mu^{\mp}\nu_\mu\nu_\tau \ .$$

The τ has similar mass to the $D^{\pm}$−meson, $m_{D^{\pm}} = 1.869$ GeV, and thus its existence was initially difficult to verify.

The τ is a spin-$\frac{1}{2}$ lepton with charge -1e. It is the heaviest observed lepton, with mass 1.777 GeV, and is the only lepton massive enough to decay hadronically. The τ, being three orders of magnitude more massive than the stable electron, has a mean decay length of 87 μm and a mean lifetime of 2.9 x 10^{-13} seconds. This short lifetime means that τs decay well before the innermost part of the Inner Detector and the lifetime is not sufficient for powerful discrimination based on a displaced vertex of the decay [22].

The τ can decay leptonically, to lighter leptons like the e or μ and associated νs, or hadronically to a number of neutral and charged hadrons and a ν_τ. The decay modes are given in Figure 2.7. All τ decay modes have an odd number of charged decay products, "daughters".

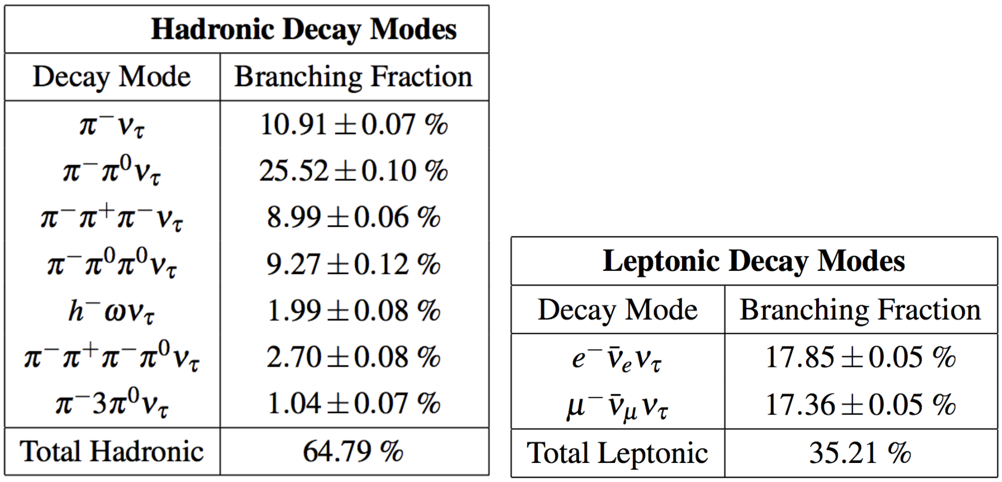

Hadronic Decay Modes

Decay Mode	Branching Fraction
$\pi^-\nu_\tau$	10.91 ± 0.07 %
$\pi^-\pi^0\nu_\tau$	25.52 ± 0.10 %
$\pi^-\pi^+\pi^-\nu_\tau$	8.99 ± 0.06 %
$\pi^-\pi^0\pi^0\nu_\tau$	9.27 ± 0.12 %
$h^-\omega\nu_\tau$	1.99 ± 0.08 %
$\pi^-\pi^+\pi^-\pi^0\nu_\tau$	2.70 ± 0.08 %
$\pi^-3\pi^0\nu_\tau$	1.04 ± 0.07 %
Total Hadronic	64.79 %

Leptonic Decay Modes

Decay Mode	Branching Fraction
$e^-\bar{\nu}_e\nu_\tau$	17.85 ± 0.05 %
$\mu^-\bar{\nu}_\mu\nu_\tau$	17.36 ± 0.05 %
Total Leptonic	35.21 %

Figure 2.7: The branching ratios for the hadronic and leptonic τ decay modes are shown [2].

The leptonic decays of τs are not discussed in this thesis because of the experimental challenge of selecting electrons and muons as coming from tau decays rather than directly from a boson. Additionally, τ decays with leptonic final states have multiple neutrinos that reduce sensitivity to the tau polarization as described in Section 2.5.

Hadronically-decaying τs decay mostly to $\pi^{\pm}$ hadrons, but also can decay to other charged hadrons such as $K^{\pm}$. Hadronic τs are classified by the number of charged daughters: 85% 1-prong, 15% 3-prong, and more rarely 5-prong.

Jet production from decays of W bosons overwhelms τ production by 6+ orders of magnitude. Given a typical rejection factor of $\mathcal{O}(1000)$ against jets from ATLAS tau identification, it is clear that achieving good signal purity in signatures with hadronically decaying taus is a significant challenge. The power of studying τs at ATLAS is contingent on the power of τ identification methods described in Chapter 5, and techniques used to separate signal and background specific to the analysis in question.

2.4.1 Processes with Taus in the Decay Chain

There is significant theoretical motivation to work with τs at ATLAS, in spite of the technical challenges and overwhelming backgrounds. There are a number of interesting already-discovered and theorized decay processes with τs in the final state

H$\rightarrow \tau\tau$: The coupling of the SM Higgs is proportional to the mass of the particle it couples to and is stronger to τs than to the other leptons because of the high mass of the τ.

$Z' \rightarrow \tau\tau$: The theorized Z' boson could primarily decay to τs, as there are many scenarios in which couplings to new physics would be enhanced in τ states over lighter-generation leptons.

$t\bar{t} \rightarrow \tau_{had} + l +$ bb $\nu\nu$: The process is of interest in part, and is the subject of this thesis, due to the third generation particles in the decay chain. If there is something special about the third, and heaviest, generation this channel is promising place in which to search. The decay chain can occur through the SM process

$$t\bar{t} \rightarrow W^+W^-bb \rightarrow \tau_{had} + l + \text{bb } \nu\nu$$

or through a SUSY model, where one or both of the W bosons are replaced with a charged Higgs boson:

$$t\bar{t} \rightarrow H^{\pm}W^{\mp}bb \rightarrow \tau_{had} + l + \text{bb } \nu\nu \ .$$

For $\tan\beta > 3$, charged Higgs bosons $H^{\pm}$ decay mainly to τ final states. In this thesis, BR($H^{\pm} \rightarrow \tau\nu$) = 1 is assumed when setting the limit. The LEP experiment set a lower bound on the mass $m_{H^{\pm}} > 90$ GeV. Up to 2009, the Tevatron found no evidence for charged Higgs boson production and placed upper limits of $BR(t \rightarrow H^{\pm}b) < 15\%$ to 20% [23].

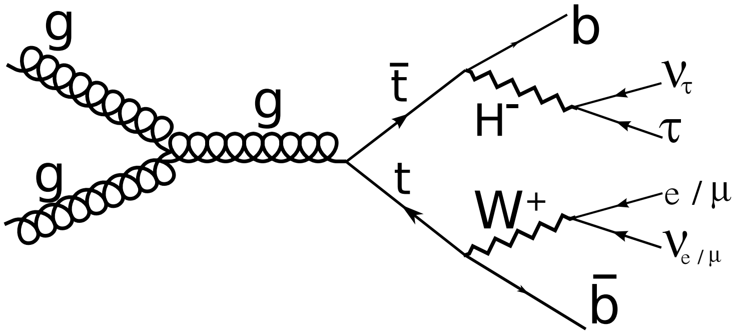

Figure 2.8: The Feynman diagram showing the $t\bar{t} \rightarrow H^{\pm}W^{\mp}bb \rightarrow \tau_{had}+ \ l+$ bb $\nu\nu$ process with l$\in \{e, \mu\}$.

2.5 Tau Polarimetry

Tau polarization, $P_\tau \equiv \frac{\sigma_L - \sigma_R}{\sigma_L + \sigma_R}$, is the relative difference between the right-handed and left-handed τ production cross sections and provides a measure of parity violation in τ production [7, 24]. Access to this quantity provides a potential discriminant in searches for physics beyond the Standard Model, particularly where identical final states involving τs are predicted with different polarizations depending on the model.

This section explains the process to distinguish a population of left-handed (τ_L) and right-handed (τ_R) 1-prong τs, from the initial $W^\pm$ and $H^\pm$ boson decays all the way to the final detector observable at ATLAS.

Helicity, h, is the projection of the spin $\vec{s}$ onto the direction of momentum, $\vec{p}$: $h \equiv \vec{s} \cdot \vec{p}$. Massive spin-$\frac{1}{2}$ fermions like τs have either positive or negative helicity; the handedness of the τ is its helicity. In this thesis, the physics described is at the relativistic limit where the positive helicity state coincides with the right-handed chiral state and the negative helicity state coincides with the left-handed chiral state. Within SM theory there exist only neutrinos with left-handed chirality and anti-neutrinos with right-handed chirality. Therefore, there exist only left-handed τ neutrinos, $\nu_{\tau,L}$, and right-handed τ anti-neutrinos, $\bar{\nu}_{\tau,R}$.

Particle	$\lvert Spin \rvert$	Lepton Number	Charge
$H^\pm$	0	0	±1
$W^\pm$	1	0	±1
ν_L, $\bar{\nu_R}$	1/2	+1	0
$\bar{\nu_R}$	1/2	-1	0
τ^-	1/2	+1	-1
τ^+	1/2	-1	+1

Table 2.5: Properties of bosons and leptons

According to theory, $W^\pm$ boson decays produce exclusively left-handed τs and right-handed anti-τs. Also according to theory, $H^\pm$ boson decays produce exclusively τ_R^-, or equivalently τ_L^+. This can be deduced by adhering to the conservation of angular momentum, lepton number, and the spin of the particular boson, as shown in Table 2.5. The diagrams in Figure 2.9 and Figure 2.10 show $W^\pm \to \tau_L \nu$ and $H^\pm \to \tau_R \nu$ decays.

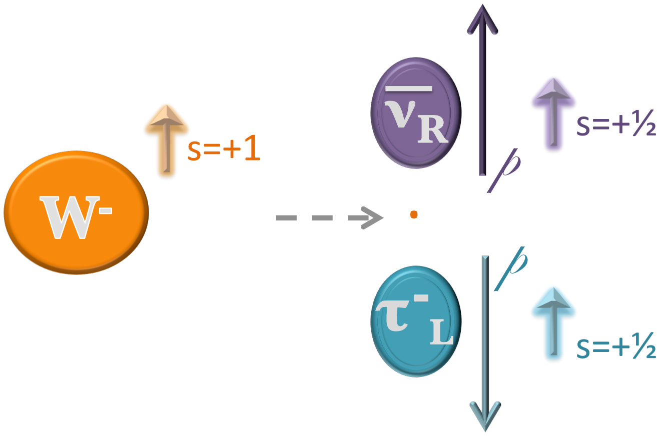

Figure 2.9: The $W^- \to \tau_L^- \bar{\nu_\tau}$ decay, in the rest frame of the boson. The W boson has spin=1, therefore the $\frac{1}{2}$-spin directions of the resulting leptons must be aligned. As the state of the ν is fixed by nature, this dictates the spin direction of the τ^- to be in the direction opposite to the direction of travel.

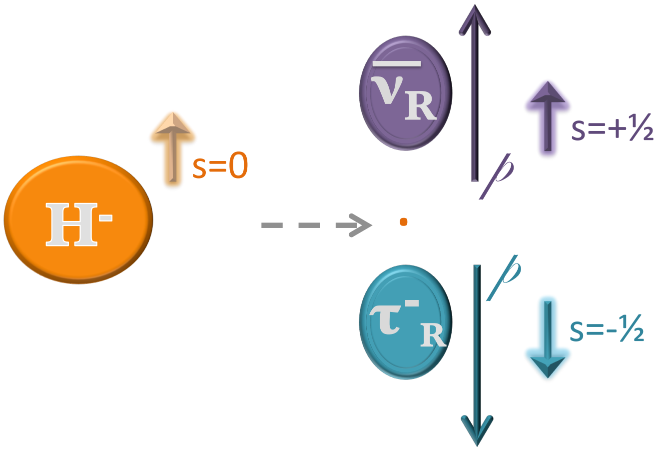

Figure 2.10: The $H^- \to \tau_R^- \nu_{\tau,R}^-$ decay is shown with the decay products in the rest frame of the boson. The $H^\pm$ boson has spin=0, therefore the spin values of the resulting leptons must be in opposite directions.

The helicity of the τ gives rise to an angular dependence of its visible decay products. The case for $\tau \rightarrow \pi^{\pm}\nu$ decay is shown in Figure 2.11.

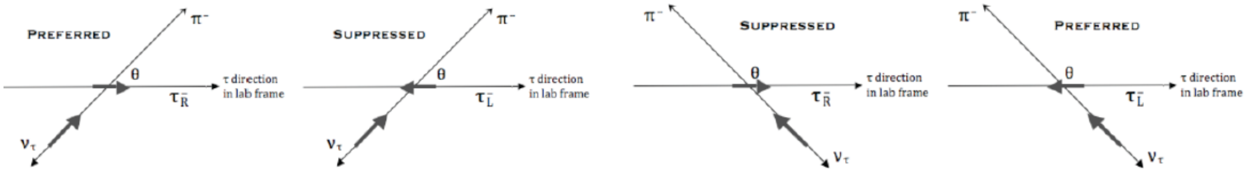

Figure 2.11: For right-handed τs, the charged pion is preferentially emitted along the line of flight of the τ whereas the opposite is true for left-handed τs. The figures show the angle θ between the τ line-of-flight and the momentum direction of the visible decay products in the preferred and suppressed scenarios [7].

The decay angle θ shown cannot be directly measured since only the hadronic decay products are observed in the ATLAS detector and neither the τ direction nor the the direction of the ν from the τ decay are determined. In the relativistic limit, $E >> m_\tau$, the relation between θ and $\frac{E_{visible}}{E_\tau}$ is given as:

$$\cos\theta = \frac{2E_{\text{vis}}/E_\tau - 1 - m_{\text{vis}}^2/m_\tau^2}{1 - m_{\text{vis}}^2/m_\tau^2}$$

where $E_{visible}$ and $m_{visible}$ refer to the visible, non-ν, τ_{had} decay products and E_τ , m_τ is the full τ energy and mass including the ν_τs.

In a majority of cases however, the τ decays through intermediate vector mesons, as shown in Figure 2.7. The more complicated cases of non-direct decays to πs must also be considered.

For the case of a $\tau \rightarrow \rho\nu_\tau$ decay, a τ_R preferentially decays to a longitudinally-polarized ρ ("ρ_{Long}") while a τ_L decays preferentially to a transversely-polarized ρ ("ρ_{Tr}"). The same holds for other intermediate vector-mesons like the a_1.

A massive vector particle, such as the ρ, has a polarization vector $\vec{\epsilon}$ with three spin states: $\{+1, 0, -1\}$. The ρ_{Tr} has two orthonormal polarizations and the ρ_{Long}

has a single polarization state in the z direction, as shown in Figure 2.12.

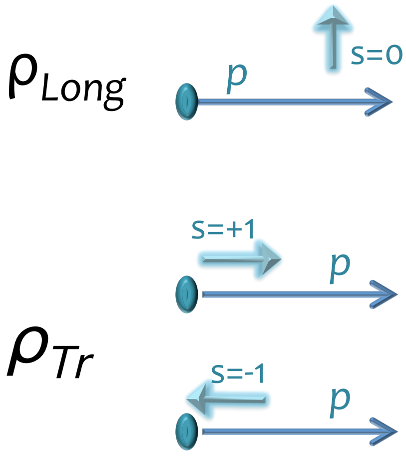

Figure 2.12: The ρ has a single longitudinal state, with the spin perpendicular to the direction of travel, and two transverse states, with the spin parallel or anti-parallel to the direction of travel.

In a coordinate system in which the ρ momentum vector is parallel to $\hat{z}$, the polarization states of the ρ are given as:

$$\vec{\epsilon}_{\rho_{Transverse}} = \tfrac{1}{\sqrt{2}}(\hat{x} \pm i\hat{y}),$$
$$\vec{\epsilon}_{\rho_{Longitunal}} = \hat{z}$$

The ρ decays to one neutral and one charged π, and in the rest frame of the ρ they are back-to-back. Given the polarization $\vec{\epsilon}_\rho$ of a ρ and the momentum of a π^+, $\vec{p}_{\pi^+}$:

$$\vec{p}_{\pi^\pm} = p(\hat{x}\sin\alpha\cos\phi + \hat{y}\sin\alpha\sin\phi + \hat{z}\cos\alpha),$$

where α is the angle between the line of flight of the ρ and the $\pi^\pm$ in the lab frame, the unique rotationally invariant scattering amplitude is constructed as:

$$\mathcal{M} = A\vec{\epsilon_\rho} \cdot \vec{p}_{\pi^\pm} \quad ,$$

where A is some constant [25]. The relation is shown in Figure 2.13.

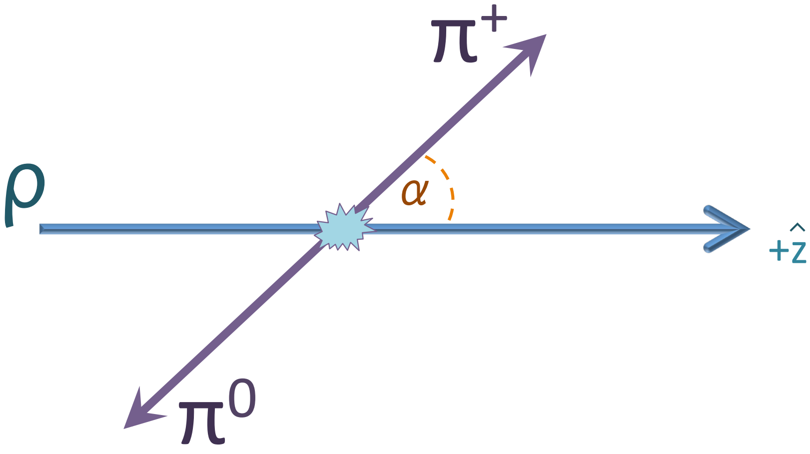

Figure 2.13: A ρ decay in the laboratory frame. The polar angle α is between the direction of travel of the ρ and the π^+. Different polarizations of ρs result in different angular distributions of $\pi^\pm$ *and* π^0. The ρ_{Tr} decays to charged and neutral πs with comparable energies while ρ_{Long} results in an asymmetry in energy sharing. This energy sharing between the charged and neutral πs is indicative of the polarization of the ρ, which is itself a discriminator between τ_L and τ_R.

The scattering amplitude, or decay rate, is defined with respect to the variable $x{:=}E_{\pi^\pm}/E_\rho$ [26]. The variable x quantifies the energy imparted on the charged π with respect to the full energy available for the ρ decay products. The decay rate for ρ_{Long} is:

$$\partial\Gamma(\rho_{Long} \to \pi^\pm\pi^0)/\partial x \;\propto\; |\mathcal{M}_{\rho_{Long}}|^2 \;=\; A^2 p^2_{\pi^\pm}\cos^2\alpha$$

After combining the two transverse polarizations of the ρ the azimuthal angle, ϕ, dependence drops out leaving the decay rate for ρ_{Tr} as:

$$\partial\Gamma(\rho_{Tr} \to \pi^\pm\pi^0)/\partial x \;\propto\; |\mathcal{M}_{\rho_{Tr}}|^2 \;=\; A^2 p^2_{\pi^\pm}\sin^2\alpha.$$

The decay rate for $\rho_{Tr} \to \pi^\pm\pi^0$ is maximal for $\alpha \approx 90^\circ$. Neither of the πs are preferentially boosted along the line of flight of the ρ_{Tr}; this results in comparable energy-sharing between the neutral and charged πs. Thus the $\rho_{Tr} \rightarrow \pi^{\pm}\pi^{0}$ decay produces πs with $p_{\pi^{\pm}} \approxeq E_{\pi^{0}}$.

The decay rate for $\rho_{Long} \rightarrow \pi^{\pm}\pi^{0}$ is maximal for $\alpha \approx 0^{\circ}$ and $\alpha \approx 180^{\circ}$. In these cases, either the π^{0} or the $\pi^{\pm}$ is boosted along the line of flight of the ρ_{Long}; this results in an unequal energy-sharing between the neutral and charged πs. Thus the $\rho_{Long} \rightarrow \pi^{\pm}\pi^{0}$ decay produces πs with either $p_{\pi^{\pm}} > E_{\pi^{0}}$ or $p_{\pi^{\pm}} < E_{\pi^{0}}$ [25, 26].

A spin analysis with the intermediate vector meson provides the detector observable at ATLAS. The angular dependence of Ψ between the ρ and π^{-} in the rest frame of the ρ is constructed. The energies of the the charged and neutral pions in the decay are related to Ψ by

$$\cos\psi = \frac{m_{\mathrm{V}}}{\sqrt{m_{\mathrm{V}^2} - 4m_{\pi}^{2}}} \frac{E_{\pi^-} - E_{\pi^0}}{|\mathbf{p}_{\pi^-} + \mathbf{p}_{\pi^0}|}$$

Though $\cos\theta$ distribution is difficult to measure, the $\cos\Psi$ distribution is related to the kinematics of the charged and neutral pions. The main detector observable at ATLAS, the "charged asymmetry", is [24]:

$$\Upsilon = \frac{E_{\mathrm{T}}^{\pi^-} - E_{\mathrm{T}}^{\pi^0}}{|\mathbf{p}_{\mathrm{T}}^{\pi^-} + \mathbf{p}_{\mathrm{T}}^{\pi^{\mathbf{0}}}|} = \frac{p_{\mathrm{T}}^{\mathrm{trk}} - (E_{\mathrm{T}} - p_{\mathrm{T}}^{\mathrm{trk}})}{E_{\mathrm{T}}} = 2\frac{p_{\mathrm{T}}^{\mathrm{trk}}}{E_{\mathrm{T}}} - 1$$

where $E_{T}^{\pi^{\pm}}$ and $E_{T}^{\pi^{0}}$ are the transverse energies of the pions, and $\mathbf{p}_{\mathbf{Tr}}^{\pi^{\pm}}$, $\mathbf{p}_{\mathbf{Tr}}^{\pi^{\mathbf{0}}}$ are the momenta of the visible τ decay products in the τ decay.

Chapter 3

The ATLAS Experiment within the Large Hadron Collider

The Energy Frontier of particle physics is driven by a need for increasingly higher-energy collisions. A fundamental goal of the experimental program at CERN is to make the first direct exploration of completely new regions of energies and distance scales. The higher energies allow for the production of more massive particles and the study of shorter-range interactions. CERN, the LHC, and ATLAS are the most advanced tools and experimental apparatuses to date that answer the theoretical questions posed in the previous chapters.

This chapter describes the CERN complex, the LHC, and the ATLAS detector.

3.1 The CERN Accelerator Complex

The accelerator chain at CERN is located underground in France and Switzerland. It is a series of increasingly powerful accelerators culminating with the Large Hadron Collider(LHC) ring that, in 2011, brought protons up to an operational energy of 3.5 TeV per beam. A schematic of the accelerator complex is shown in Figure 3.1. Initially, hydrogen atoms are fed, in a controlled rate, into the source chamber of a LINear ACcelerator(LINAC).

Electrons are stripped from the hydrogen atoms in a regime where the pressure is $\simeq$ 2 millibar and the extraction potential is 92 kV. Protons are accelerated by an sinusoidal electric field in the drift tubes. The peaks of the electric field occur in a regular pattern. With each successive drift tube, the particles are moving faster than before, and so the series of drift tubes get successively longer and placed further apart. The protons exit the LINAC traveling at one-third c, with an energy of 50 MeV.

The Proton Synchrotron Booster (PSB) is the second stage in the accelerator chain. It is the first and smallest circular proton accelerator, at 157 meters in circumference. The booster has four rings, and the proton beam is temporarily separated into four components for acceleration. The PSB receives protons from the LINAC and accelerates them to energies of 1.4 GeV. By the time the protons exit the PSB, they are traveling at 90% c.

The Proton Synchrotron(PS) accelerates the protons until they reach 99.9 % c and have energies of 26 GeV. Next, the protons are fed into the Super Proton Synchrotron (SPS), the final stage before the LHC, where they reach energies of 450 GeV. The protons in each beam then enter the LHC and are accelerated until their energies are increased to 3500 GeV in 2011. Though in 2011 the LHC collided these protons at center of mass energy, $\sqrt{s}$, of 7 TeV, the design $\sqrt{s}$ is 14 TeV. The design instantaneous luminosity, defined in Equation 3.1, is 10^{34} cm^{-2} s^{-1}.

The proton beams at the LHC are not continuous streams of particles; they are regularly-spaced proton bunches. The bunches are injected from the SPS ring into the main LHC ring with careful timing so that they are placed in the desired buckets by the controllers. The LHC was designed to operate with 2808 bunches per beam, with 10^{11} protons per bunch, with beam dump gaps reserved for safety. This results in a minimum time between bunch crossings at each of the interaction points of 25 ns. The synchrotrons in the accelerator chain grow successively larger and each is capable of accepting multiple injections from the previous accelerator.

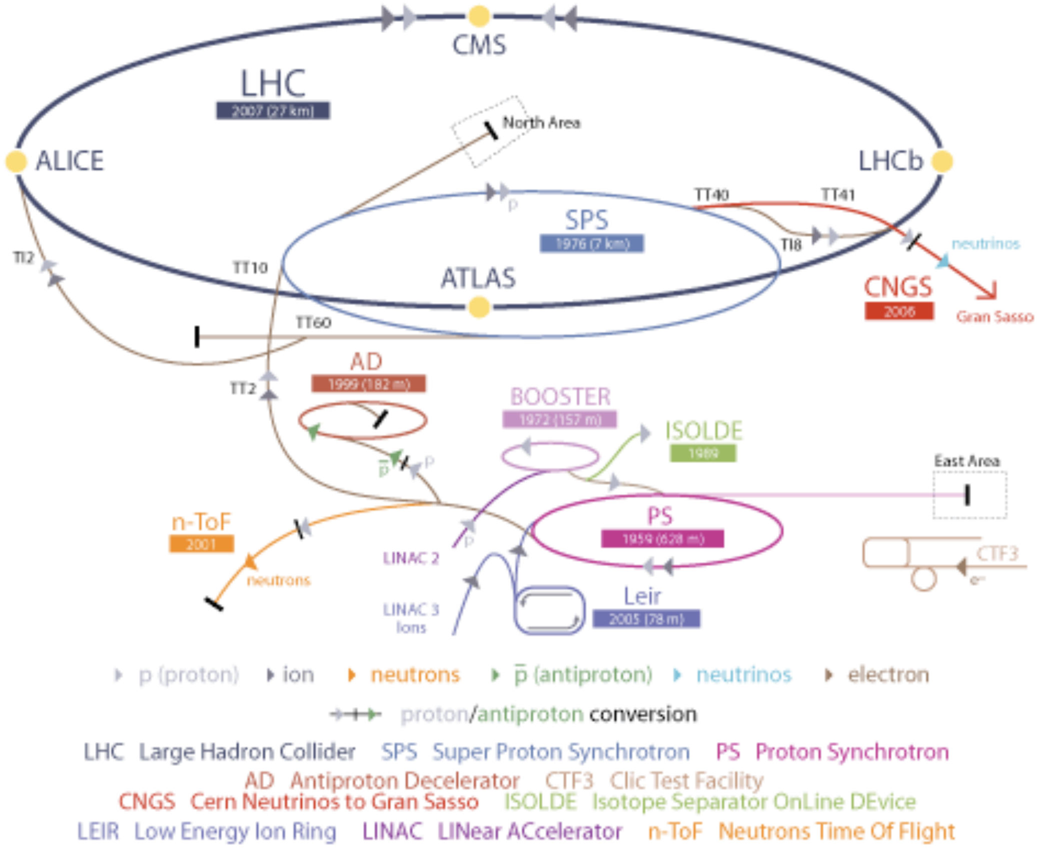

Figure 3.1: Schematic of the CERN accelerator chain complex. Image Courtesy: CERN

The schematic drawing of the nominal proton-proton bunch pattern is shown in Figure 3.2. In 2011, the minimum bunch spacing was 50 ns.

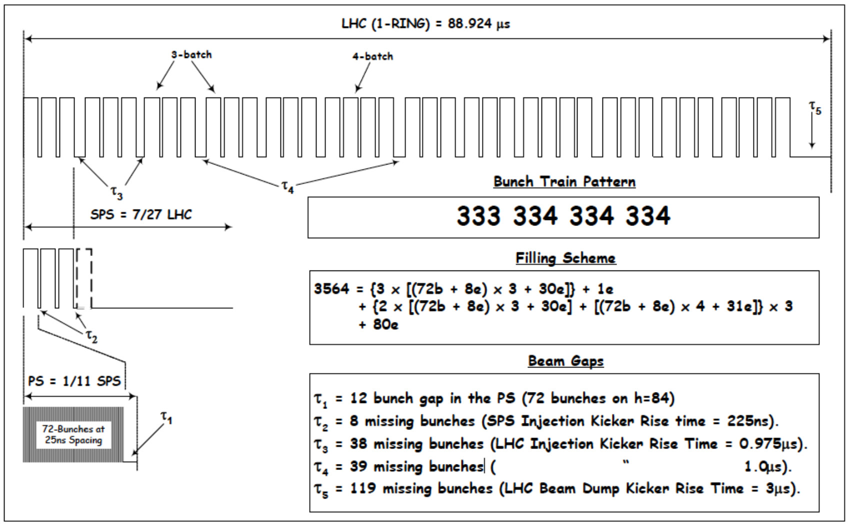

Figure 3.2: A schematic drawing of the bunch filling scheme used for nominal proton-proton collisions at the LHC [8]. One LHC fill corresponds to 12 SPS fills; 1 SPS fill can correspond to 2 PS fills; 1 PS fill corresponds to 72 filled and 12 empty bunches.

3.2 The Large Hadron Collider

The Large Hadron Collider (LHC) is the most recent and largest addition to CERN's accelerator chain. The LHC was built in the 27 km-long circular tunnel that held the Large Electron Positron(LEP) Collider. It accelerates two oppositely-circulating beams of protons, each in its own beam pipe. Those beams intersect at four interaction points, producing highly energetic collisions [27, 28].

A low-emittance particle beam confines particles to have nearly the same momenta and be within a small region. In a colliding beam accelerator, keeping the emittance small results in a greater probability of particle interactions and therefore a higher luminosity.

In order to reach the specifications, the proton beams at the LHC travel in opposite directions, close to the speed of light in separate but adjacent beam pipes. These beam pipes are kept under high vacuum conditions. The beams are guided around the accelerator by a strong magnetic field, which is shaped by a variety of superconducting multipole magnets. The coils of niobium-titanium electromagnets are kept in a superconducting state so that there is little resistance and loss of energy. The magnets are cooled with superfluid helium and kept at a temperature of 2 Kelvin and magnetic strength of 8.4 Tesla. There are in total 1232 dipole magnets used to direct the beams in their circular paths. There are 858 quadrupole magnets used to keep the beams in focus. These quadropoles create a magnetic field, with radially increasing magnitude, and keep the protons tightly bunched to allow for the greatest number of collisions during the beam lifetime. There are also higher order multipole magnets, such as sextupoles and octupoles, used to counteract the deterioration of the beams [27].

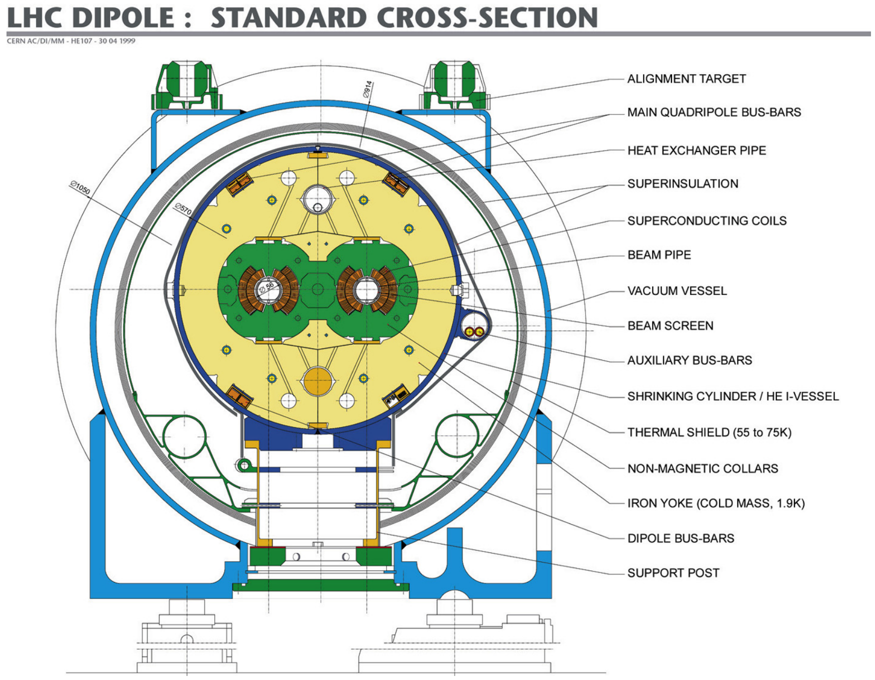

Figure 3.3: Diagram of the cross-section of an LHC ring. Image Courtesy: CERN

The instantaneous luminosity depends on the beam parameters and is given by:

$$L = \frac{N_b^2 n_b f_{rev} F \gamma}{4\pi\epsilon_n\beta} \ . \tag{3.1}$$

The design values of these parameters shown in Table 3.1 [28].

Parameter	Description	LHC Design Value
N_b	number of particles per bunch	1.15 x10^{11}
n_b	number of bunches per beam	2808
f_{rev}	revolution frequency	1.22 kHz
F	geometric luminosity reduction factor	0.836
γ	relativistic gamma factor	7461

Table 3.1: LHC beam parameters

The integrated luminosity, $\int$Ldt , is the integrated instantaneous luminosity and gives the total number of interactions over a given time period.

One of the experiments taking advantage of the LHC collisions is the ATLAS detector.

3.3 The ATLAS Detector

ATLAS (A Toroidal LHC ApparatuS) is one of two general-purpose detectors located on the LHC ring that aims to answer the questions stated in the previous chapters. The experiment is designed to take advantage of the unprecedented energy available at the LHC and observe phenomena that involve high mass particles which were not accessible at earlier lower-energy accelerators. The ATLAS detector consists of layers of different technologies with varying functions, centered around the interaction point.

3.3.1 The Coordinate System

A coordinate system is needed to uniquely define the location of interactions within the detector without ambiguity. The standard ATLAS coordinate system is a standard right-handed Cartesian system. The positive x-axis points towards the center of the LHC tunnel; the positive y-axis points up; the z-axis points along the beamline. This $\{x, y, z\}$ set of variables can be more conveniently expressed by the $\{r, \phi, \eta\}$ set of variables. The angle ϕ is the angle in the x-y plane with respect to the x-axis. The pseudorapidity, η, is motivated by the rapidity, y. The rapidity of a particle with momentum p_z and energy E is:

$$y \equiv \frac{\ln \frac{E+p_z}{E-p_z}}{2} \ . \tag{3.2}$$

The p_z of the final state system is generally nonzero and is not known because LHC collisions are between quarks and gluons, which themselves have unknown momenta. Therefore, invariant quantities must be used when describing the system. The difference of two rapidity values is invariant under boosts in the $\hat{z}$ direction. Furthermore, cross-sections are flat as a function of rapidity. However, rapidity is a function of a particle's energy and is less directly useful as a coordinate. The rapidity variable can be salvaged, since ATLAS produces high-momenta particles in the high energy regime of |p| $\gg$ m. In this high-energy limit, the pseudorapidity η is defined:

$$E^2 = m^2 + p^2 \approx p^2 \tag{3.3}$$

$$y \approx \frac{\ln \frac{1+\cos\theta}{1-\cos\theta}}{2} = -\ln\tan\frac{\theta}{2} \equiv \eta \tag{3.4}$$

where

$$|p| = p_z \cdot \cos\theta \ . \tag{3.5}$$

The angle θ is in the y-z plane measured from the z axis. The pseudorapidity approximates to y for relativistic particles, and is a function of θ alone. Figure 3.4 shows some values of η and ϕ for comparison.

Pseudorapidity is the variable commonly used to label segmented regions in the detector, since ATLAS is symmetric in ϕ. Due to the geometry of the detector subsystems the region of $|\eta| \leq 1.37$ is referred to as the "barrel," the region of

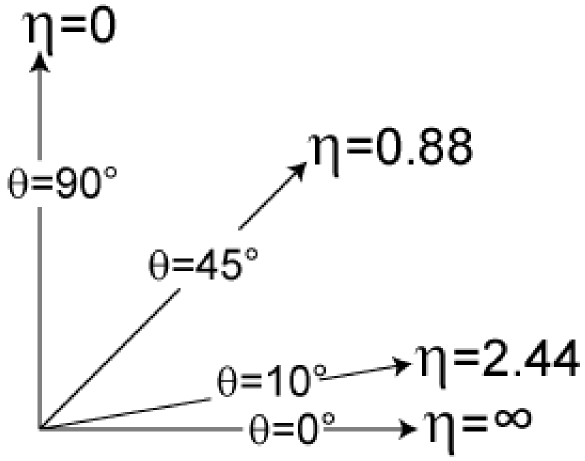

Figure 3.4: Pseudorapidity, η, is defined from 0 to ∞.

$1.37 < |\eta| < 1.52$ is referred to as the "crack," and $|\eta| \geq 1.52$ is referred to as the "endcap." The choice of variables $\{\phi, \eta\}$ also defines the commonly-used distance measure ΔR:

$$\Delta R \equiv \sqrt{\Delta\eta^2 + \Delta\phi^2}\ . \tag{3.6}$$

The following sections make extensive use of these variables and the coordinate system.

3.3.2 The Tripartite Trigger at ATLAS

Three successive levels of triggering reduce the rate of events for permanent storage from a nominal bunch-crossing rate of 40 MHz to roughly 400 Hz. The three levels are Level-1 (L1), Level-2 (L2) and the Event Filter (EF). The details of the ATLAS trigger system are shown in Figure 3.5.

L1, a hardware trigger that incorporates only calorimeter and Muon Spectrometer information, identifies Regions of Interest (ROI) and reduces the event rate from nominally 40 MHz to 75 kHz. The maximum allowed time between a collision and decision, the latency, at L1 is 2.5 μs. L2 and the EF are software triggers, and

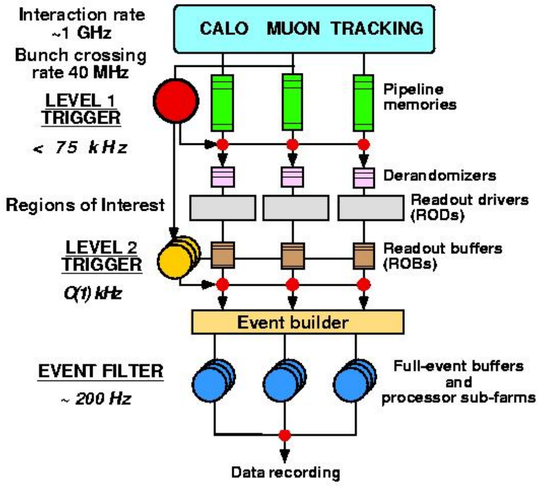

Figure 3.5: The tripartite trigger at ATLAS

combine to form the High Level Trigger (HLT). The HLT, unlike L1, has full access to all detector quantities. L2 reduces the recorded event rate to 3.5 kHz by using additional detector information and using more sophisticated algorithms for each ROI than does L1. The average decision time per event at L2 is 10 ms. If the event passes the L2 trigger, the event gets fully assembled on an event-builder node. The EF has a latency of 1 s, and evaluates the entire event to make the final trigger decision. If the event passes the HLT, it is transferred to permanent storage and analyzed by the offline reconstruction [29]. Triggers for analyses rely on a single or few specific features of an event, like the presence of a lepton, photon, a high momentum jet or large E_T^{miss}. These generic signatures can capture a wide range of physics processes. More information about the ATLAS trigger system is in [30, 29] and the Trigger section of [31].

3.3.3 Inner Detector and Tracking

The Inner Detector(ID) begins a few centimeters from the beam axis, has a total radius of 1.2 meters, and is seven meters long surrounding the beam pipe. It is immersed in a 2 T magnetic field, and this field causes charged particles to curve in proportion to the particles' momenta. The ID tracks charged particles by detecting their interactions with material at discrete points, thus providing information about the particles that pass through and their transverse momentum, p_T [10]. There are three parts of the ID: Pixels, SCT, and TRT. These three subdetectors are shown in Figure 3.6. A technical schematic of a quadrant of the ID in the r-z plane is presented in Figure 3.7.

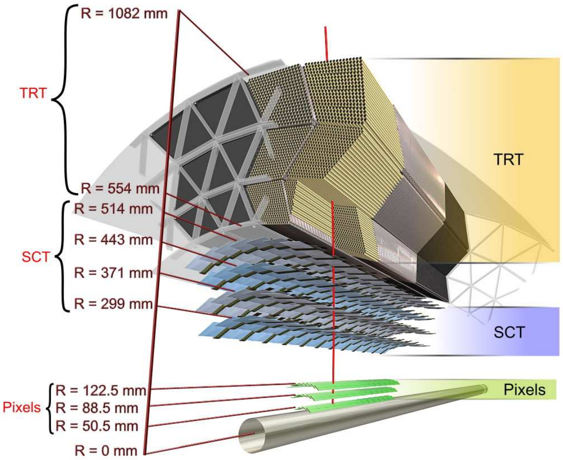

Figure 3.6: The Inner Detector of ATLAS. Image Courtesy: CERN

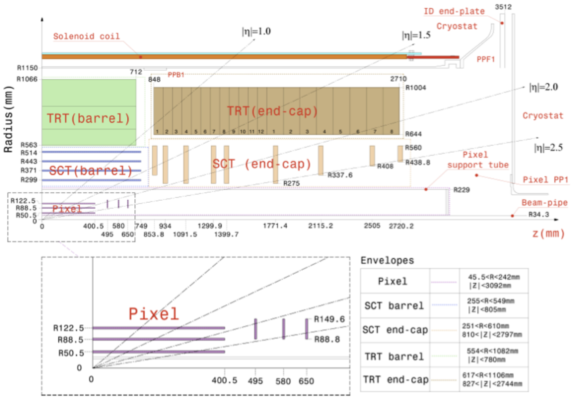

Figure 3.7: A quadrant of the Inner Detector, in the r-z plane [9]

3.3.3.1 Pixel

The Pixel Detector is the inner-most tracking detector. It has a high granularity and is close to the interaction point, thus allowing a spatial resolution of 19 μm in the transverse plane and 105 μm in the longitudinal plane.

It is composed of millions of silicon pixels that measure the ionization created by high energy charged particles. These semiconductor sensors are composed of 250 μm thick n-doped silicon bulk with n^+ and p^+ implants on opposite ends. A potential difference is applied to the p^+ side, "depleting" the bulk of free charge carriers. Electron-hole pairs are produced when a particle travels through this depleted bulk, and the current from these free electrons is collected on the sensor [10, 32].

3.3.3.2 SemiConductor Tracker

The SemiConductor Tracker (SCT) is the middle subdetector of the ID. It functions similarly to the Pixel detector but has long and narrow strips of silicon rather than small pixels and has less granularity. The barrel layers are made up of rectangular strips (6 cm by 80 μm) and the endcap layers are made up of trapezoidal strips (6 cm by an average width of 80 μm). The width of the trapezoidal strips increases with the radial distance from the beam line. The noise occupancy is on the order of 10^{-4} and the hit efficiency is 99.7%. The SCT can reconstruct electrons and μs that have $pT \geq 5$ GeV with a 95% or better efficiency. A photo of the SCT during assembly is shown in Figure 3.8.

3.3.3.3 The Transition Radiation Tracker

The Transition Radiation Tracker (TRT) is the outermost layer of the ID at ATLAS. We want to discriminate particle signatures, and the TRT is especially important because it provides information that is useful for particle identification.

The TRT is a 298,304-straw tracker, where each straw acts as a gaseous drift

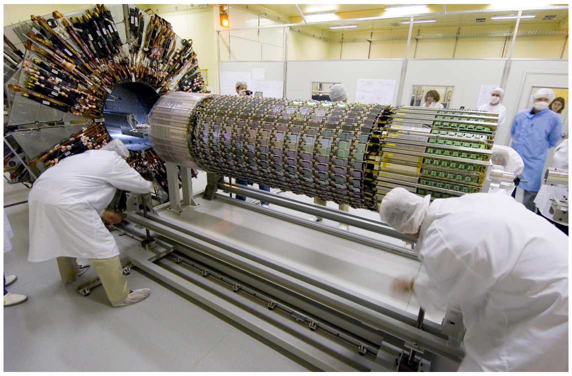

Figure 3.8: A photo of the silicon tracker being assembled. It is made up of 3 concentric cylinders that are the barrel layers, and three concentric disks on either side of the forward regions. Reprinted from [10].

chamber. In the barrel section, the cylindrical straws are arranged parallel to the direction of the beam axis. In the two endcap sections, covering 1.0 $<|\eta|<$ 2.0, the straws are perpendicular to the beam axis, arranged in wheels. The straws are each 4 mm in diameter, but vary from 40 to 150 cm in length. The straws are hollow except for 31 micrometer diameter conducting gold-plated tungsten wires along their axes; they are filled with a 70% Xe, 27% CO_2, and 3% O_2 gas mixture. For each straw, there is a nominal 1530 V potential difference between the wall and the conducting wire.

The TRT has tracking and particle identification capabilities. The TRT measures the Transition Radiation(TR) of particles, and is powerful component of ATLAS for discrimination between electrons and hadrons. When a highly relativistic charged particle with Lorentz factor $\gamma{>}10^3$ traverses the TRT, TR photons in the soft x-ray wavelength regime with energies 5 - 30 KeV, are emitted. Transition radiation is emitted whenever a charged particle passes suddenly from one medium to another. As the two media have different electromagnetic properties, the fields reorganize themselves as the particle passes through the interface. In the process of reorganization, TR is emitted. The number of TR photons emitted is dependent on $\frac{Energy}{mass}$ of the particle.

Therefore, for a given energy, electrons produce a larger amount of TR than do pions.

As particles drift toward the wires in the straws and cascade in the strong electric field, a signal is produced. The signal on each wire of each straw is amplified and discriminated against the two thresholds. The number of LT hits, with a threshold above 0.3 keV, is used to discriminate between noise and signal. The number of HT hits, with a threshold above 6-7 keV, is used to separate electrons and pions. A fairly clean electron-pion separation can be achieved by counting the number of HT hits along a reconstructed particle track [33]. The TRT front electronics provide the number of Low Threshold (LT) interactions and the number of High Threshold (HT) interactions. The HT fraction is the fraction of hits on track that exceed the high threshold; Figure 3.9 shows the HT fraction distributions for electron and pion candidates for the TRT barrel and endcap regions. Further theoretical support for the methods used by the TRT can be found in Chapter 13.7 of [34].

In this thesis, the strengths of the TRT have been well-utilized as it is one of the most powerful ways at ATLAS to discriminate between hadronic τ (such as pion) and non-τ (such as electron) signatures. This technology not mirrored by the CMS experiment.

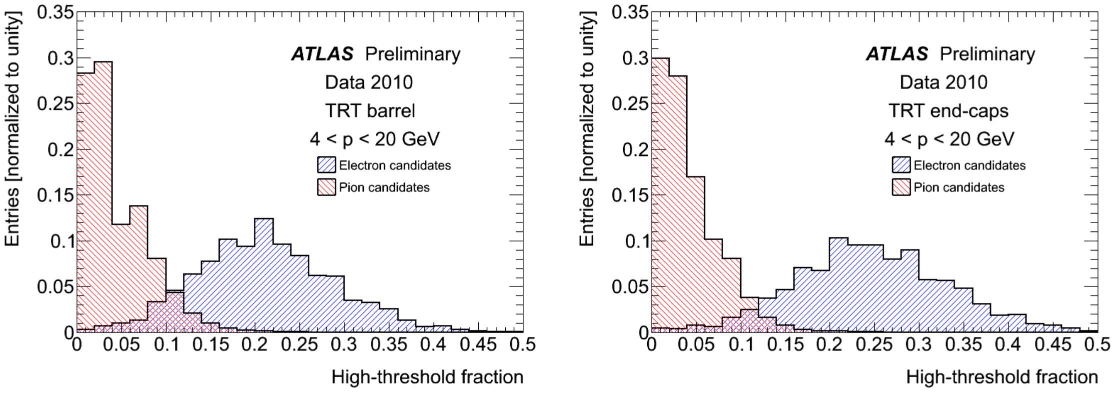

Figure 3.9: The HT fraction in the barrel(left) and endcap(right) regions with at least 20 hits for electrons and pions. The electron candidates are from photon conversions [33].

3.3.4 Calorimetry at ATLAS

The Electromagnetic and Hadronic (HCal) Calorimeters lie outside the solenoidal magnet surrounding the ID. They are designed to measure the energy of particles that exit the tracking chambers. ATLAS calorimetry is composed of four separate calorimeter systems. All four of systems are sampling calorimeters, consisting of alternating layers of absorber and active media. The incoming particles shower in the absorber medium, and the active medium measures the ionization energy of the secondary shower particles. This process is repeated until the energies of the secondary particles are too low to produce additional showers [29, 35]. The energy resolution of the calorimeters is parametrized with the following equation:

$$\frac{\sigma_E}{E} \equiv \frac{A}{\sqrt{E}} \bigoplus \frac{B}{\sqrt{E}} \bigoplus C \tag{3.7}$$

The first term takes into account the intrinsic measurement error in high numbers of particle production, as it is a stochastic process. This is the largest effect. The second term represents the contribution due to electronic and pile-up noise, and the third term represents the contribution from a non-uniform calorimeter response. Of these three effects the second is the smallest and contributes a negligible amount.

The EM calorimeter has a liquid Argon (LAr) active medium with lead absorber plates. It extends radially to an outer radius from the beam of 2.25 m. The geometry of the EM calorimeter is such that there are minimal cracks in the azimuthal direction. This is accomplished with an accordion-like arrangement of electrodes. The EM calorimeter is divided into three components: the central barrel portion $|\eta| < 1.475$, and two endcap sections with $1.375 < |\eta| < 3.2$.

The EM calorimeter is segmented in three longitudinal layers around the beam axis. The position granularity in η and ϕ vary for these layers. In addition to the three EM calorimeter layers, there is also a presampler in the region $|\eta| < 1.8$.The presampler detector is used to correct for energy losses of electrons and photons, and is located closest to the ID. The energy resolution of the EM calorimeter is $\frac{\sigma_E}{E} = \frac{10\%}{\sqrt{E}} \bigoplus 0.7\%$, as described by Equation 3.7.

Most of the energy deposition of an electromagnetically interactive particle is in the lead absorbers and LAr. However, energy is also deposited in non-instrumented material in the solenoid and cabling regions between the presampler and first layer the EM calorimeter. Some of the energy also remains undetected when particles exit the EM calorimeter. The cluster energy of a particle is calculated as the sum of the energy in each of the three layers of the EM calorimeter, each weighted by a factor. The weighting factors, called longitudinal weights, are optimized for a linear response [31].

The HCal measures the energies of hadronized quark and gluon showers, protons, and charged pions. The HCal extends radially 2.28m $<|r|<$ 4.25m. It is divided into three components: the central barrel Tile calorimeter with $|\eta|<1.7$, and two endcap calorimeters $1.5 <|\eta|< 4.9$, which provide large η coverage.

The hadronic barrel calorimeter is a sampling detector composed of "Tiles". The Tiles are the active medium and are plastic scintillator plates surrounded by steel absorber material. The spatial granularity of the HCal is courser than that of the EM calorimeter, approximately $\Delta\eta$ x $\Delta\phi = 0.1$ x 0.1. The energy resolution of the hadronic calorimeter is $\frac{\sigma_E}{E} = \frac{50\%}{\sqrt{E}} \bigoplus 3\%$ in the barrel region and $\frac{\sigma_E}{E} = \frac{100\%}{\sqrt{E}} \bigoplus 10\%$ in the forward region, as described by Equation 3.7.

The Tiles are deep enough so that they provide good containment for the hadronic showers. The response of the HCal also provides for good resolution for high-energy objects. The HCal performs crucial measurements that are important for a variety of physics signatures, including hadronically-decaying τs.

The Hadronic Endcap Calorimeter(HEC) uses LAr for the active medium and covers $1.5 < |\eta| <3.2$. The granularity is $\Delta\eta$ x $\Delta\phi = 0.1$ x 0.1 for $|\eta| < 2.5$ and $\Delta\eta$ x

$\Delta\phi = 0.2$ x 0.2 for $|\eta| > 2.5$. The HEC is sensitive to both EM and hadronic showers.

The Forward Calorimeter (FCal) covers the region $3.1 < |\eta| < 4.9$. Since it is close to the beam line, it receives a large flux of particles from collisions. There are three components in the FCal. The first is optimized for EM calorimetry and the other two for hadronic calorimetry.

3.3.5 Muon Spectrometer

Muons are minimum ionizing particles in the dense calorimeter material described above and penetrate the ATLAS detector. Therefore, the Muon Spectrometer(MS) is the outermost subdetector at ATLAS. It extends from a radius of 4.25m to 11m. In the Muon System the magnetic field is supplied by toroidal magnets.

The MS is a combination of two subdetectors for triggering, and two subdetectors for tracking. The Muon trigger system uses Resistive Plate Chambers (RPCs) in the barrel region and Thin Gap Chambers (TGCs) in the endcap regions. The barrel toroid produces a magnetic field of 0.5 T and the endcap toroid a field of 1 T. These fields are produced by coiling super conducting wire made from a Nb-Ti-Cu alloy around each ring segment. A diagram of the MS is shown in Figure 3.10.

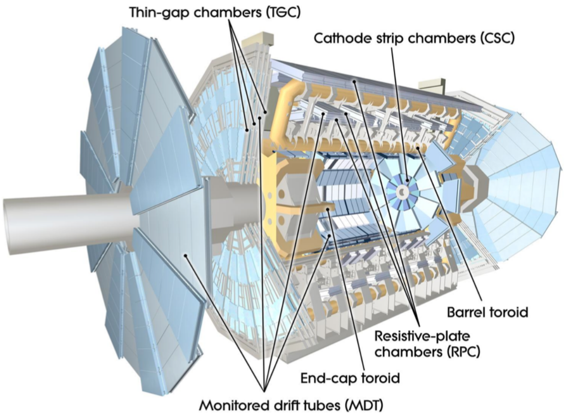

Figure 3.10: The ATLAS Muon System is shown. The triggering system, comprised of RPCs and TGCs trigger on μs with $|\eta| < 2.4$. The tracking system, comprised of the MDTs and CSCs, provides tracking up to $|\eta| < 2.7$ [10].

3.3.6 2011 Pile-up and Luminosity Conditions at ATLAS

In 2011 the LHC ran with varying numbers of protons per bunch, with a significant increase in August as shown in Figure 3.11. This increased the instantaneous luminosity and therefore increased the number of interactions in each bunch crossing. These additional interactions result in additional activity throughout the detector and are referred to as "pile-up." There are multiple processes that can contribute in a single bunch crossing. The various types of processes are the hard-scatter, minimum bias, and backgrounds such as those from detector noise, cosmic rays and beam halo interactions. Pile-up results in the presence of hits other than the hard scatter that effect reconstruction [9].

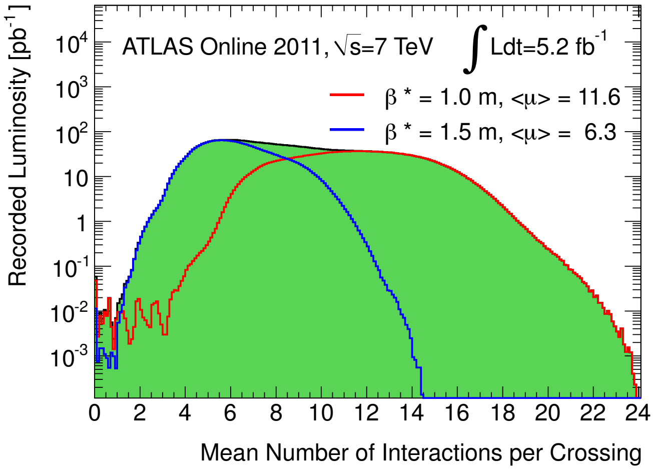

Figure 3.11: The luminosity-weighted distribution of the mean number of interactions per crossing, $< \mu >$ [9]. The plot is shown for data taken before and after a technical stop where the β was changed to provide a higher $< \mu >$. The mean number of interactions per crossing comes from a Poisson distribution on the number of interactions per crossing and is calculated from the instantaneous luminosity; see Equation 3.1.

This is different from the underlying event: in-time pile-up describes events coming from additional proton-proton interactions in a given bunch crossing, while the underlying event describes additional interactions originating from the same proton collision. Out-of-time pile-up refers to events from successive bunch crossings.

The total integrated luminosity profile collected in 2011 at ATLAS is given in Figure 3.12. The maximum instantaneous luminosities reached in 2011 are shown in Figure 3.13.

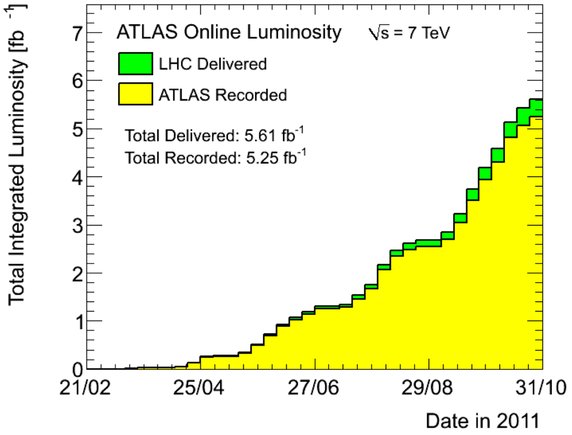

Figure 3.12: Cumulative luminosity versus date delivered to (green) and recorded by (yellow) ATLAS during stable beams and for p-p collisions at $\sqrt{s}$=7 TeV in 2011 [9].

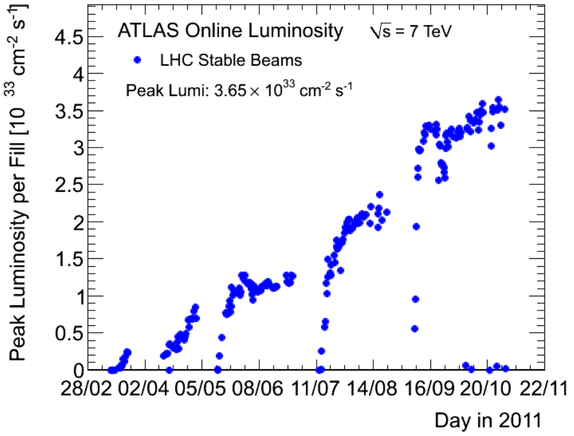

Figure 3.13: The maximum instantaneous luminosity versus day delivered to ATLAS. The luminosity determination is the same as described above for the integrated luminosity. The peak luminosities during stable beam periods is shown [9].

Chapter 4

Event and Particle Reconstruction

The reconstruction software processes the raw detector information and identifies candidate physics objects. Charged particles' tracks are reconstructed from the position hits in the Inner Detector (ID), and from the set of tracks in an event, the primary and secondary verticies are reconstructed. Muons are reconstructed from MS tracks and matched to an ID track. Electrons, photons, τs and jets are reconstructed from clusters of energy deposited in the calorimeter, and in some cases are matched with information from the ID.

4.1 Event Reconstruction

Physics analyses use both LHC and simulated data. For simulated data, event generators first simulate the initial hard processes, where the incoming and outgoing particles in the collision have a large momentum transfer.

Then the event generator evolves the outgoing particles, using the Standard Model or other physics theories being explored, to produce a sample of events with final states in relative proportions as expected from theory.

Once the physics processes are generated, they pass through ATLAS detector simulation. The results from the simulation are interpreted by the same reconstruction algorithms as data. The process of simulated event reconstruction thus allows for a direct comparison to data events. The two types of events can be considered using the same analysis methods. The process is shown as a flowchart in Figure 4.1.

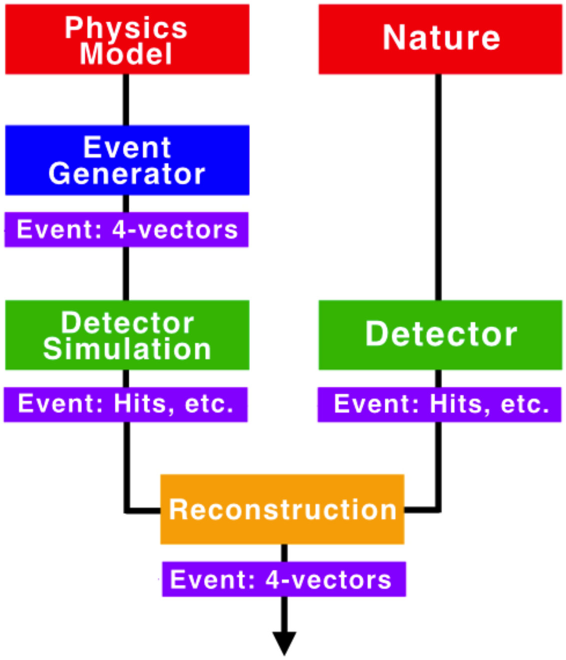

Figure 4.1: The simulated event flowchart showing an initial predicted physics model resulting in a sample of simulated events reconstructed in the same way as data from LHC proton-proton collisions. Image Courtesy: Burton DeWilde, Stony Brook

A typical process at the LHC, shown in Figure 4.2, contains a primary hard scatter subprocess, the underlying event, hadronization of bare colored quarks and gluons, and hadron formation and subsequent decay.

4.2 Electron Reconstruction

The electron algorithm used in this thesis is designed to reconstruct isolated high momentum electrons. Both calorimeter and tracking information are used to form an electron candidate object.

Each electron candidate begins as a preliminary set of seed clusters. These seed clusters, with required E_T >2.5 GeV, are combined in 3 x 5 units of $\Delta\eta$ x $\Delta\phi$ of the

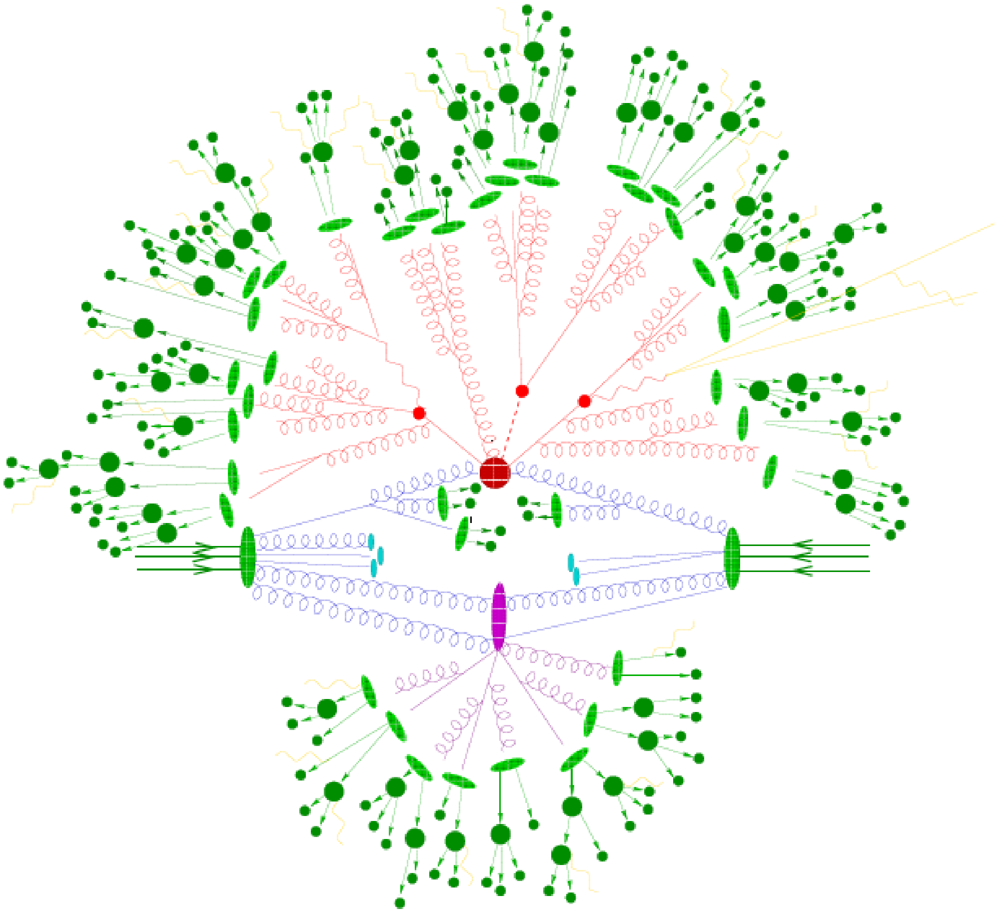

Figure 4.2: Illustration of a typical hadron-hadron collision.The red circle in the center represents the hard subprocess which occurs at the interaction point. The purple oval represents the underlying event. The light green ovals represent hadronization and the dark green circles correspond to the subsequent decays. Image Courtesy: Frank Seigert, Durham University.

middle layer of the EM Calorimeter. That second layer EM calorimeter is composed of squares of $\Delta\eta$ x $\Delta\phi = 0.025$ x 0.025 elements and is described in Chapter 3. The 3 x 5 seed cluster size is a subset of the final EM cluster [36, 35].

After the clustering, the electron four-momentum is computed using the additional track information. The electron is matched to the best nearby track from the ID within $|\eta| < 2.47$. For an electron candidate to be formed, a track from the ID must be matched to the cluster. The track is required to match the cluster position in the calorimeter within $\Delta\eta < 0.05$, and $\Delta\phi < 0.1$ in the direction toward the curvature of the track and $\Delta\phi < 0.05$ in the opposite direction of the curvature of the track.

The electron energy is computed as the weighted average between the cluster energy and the track momentum, while the η and ϕ directions are taken from the corresponding track parameters [36].

Following electron reconstruction, electron identification algorithms are applied on the reconstructed objects.

4.3 Muon Reconstruction

Four types of μ reconstruction algorithms are available at ATLAS, and this thesis uses the “combined” reconstruction algorithm. A combined reconstructed μ is one where information from both the MS and the ID are incorporated. Candidates are composed of full MS tracks and are closely matched with ID tracks. An event with a μ candidate is shown in Figure 4.3.

4.4 Tau Reconstruction and Identification

Because of the importance of τs for this thesis, τ reconstruction and identification are described in detail in Chapter 5.

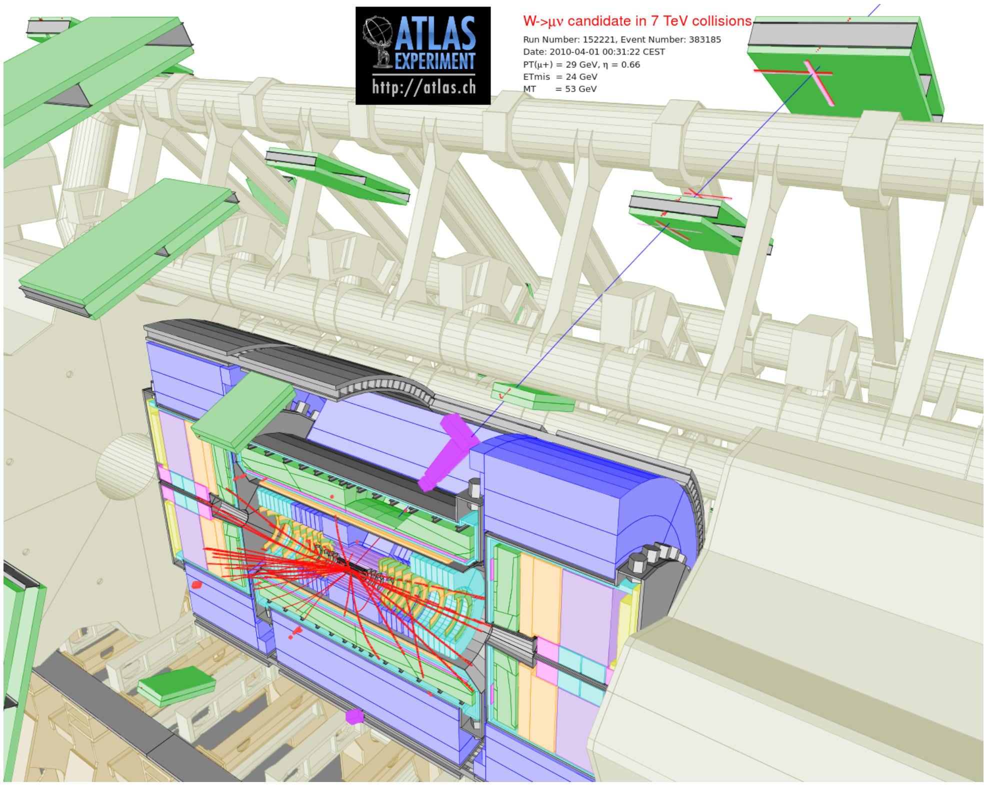

Figure 4.3: The decay results of a $W \rightarrow \mu\nu$ candidate event are shown, from early data-taking in 2010. The μ is reconstructed with the MS, as illustrated.

4.5 MET

Missing transverse energy, E_T^{miss}, can be reconstructed in all events by balancing the transverse momentum. Since the incoming partons have near-zero p_x and p_y, transverse momentum is conserved before and after the collision. Figure 4.4 shows the energy balance conserved by the direction and magnitude of E_T^{miss} for a hypothetical event at ATLAS.

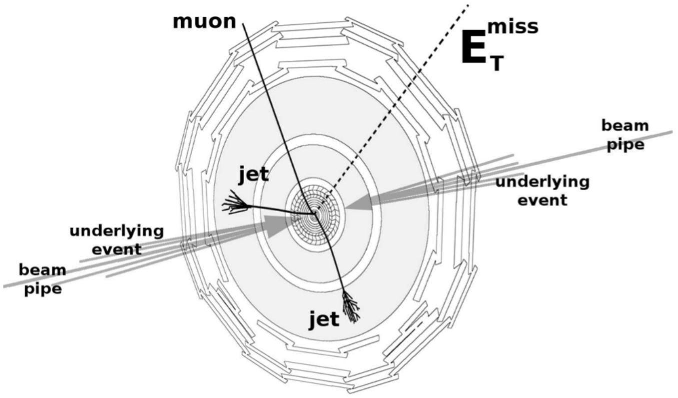

Figure 4.4: A snapshot of an event is drawn, showing the relationship of E_T^{miss} to physics objects. This diagram is modeled on a hypothetical event, where a W is balanced against jets. The E_T^{miss} takes the direction of the ν_μ (the dotted line) from the $W \to \mu\nu_\mu$ decay. Image Courtesy: Jeremiah Goodson, Stony Brook

E_T^{miss} represents the combined transverse momentum of all particles, like neutrinos, that carry away undetected momentum. The calculation of E_T^{miss} depends on the corrected energy deposited in the detector, where the corrections are dependent on the identification of candidate objects in the event.

E_T^{miss} is object-based and is calculated from topological clusters calibrated at the EM scale and corrected according to the energy scale of the associated objects. High-p_T jets that do not overlap with any electrons are calibrated at the Jet Energy Scale (JES). Muon p_T is calculated from the sum of the combined Inner Detector and Muon Spectrometer, once the μ deposition in the calorimeter has been subtracted to avoid double-counting. Electrons are taken at EM scale and low-p_T jets at the Local Cluster Weighting (LCW) scale. The remaining clusters not associated with high-p_T objects are included, at EM scale, in a CellOut term, [37].

E_T^{miss} :

$$E_{Tx,y}^{miss} = E_{x,y}^{e,\gamma} + E_{x,y}^{\mu} + E_{x,y}^{\tau} + E_{x,y}^{jets} + E_{x,y}^{low-p_T jets} + E_{x,y}^{CellOut} \tag{4.1}$$

$$E_T^{miss} \equiv \sqrt{\left(\Delta E_x^{miss}\right)^2 + \left(\Delta E_y^{miss}\right)^2} \tag{4.2}$$

The terms in the formulation of E_T^{miss}, Equation 4.1, are defined [37]:

- $E_{x,y}^{e}$ is reconstructed from cells in electrons with $p_T > 10$ GeV. The default electron calibration is used.

- $E_{x,y}^{\gamma}$ is reconstructed from cells in photons passing strict identification requirements with $p_T > 10$ GeV with the EM scale calibration

- $E_{x,y}^{\tau}$ is reconstructed from cells in τs passing strict identification requirements with $p_T > 10$ GeV with the LCW scale calibration

- $E_{x,y}^{\mu}$ is the μ p_T after the small μ deposition in the calorimeter has been subtracted out

- $E_{x,y}^{jets}$ is reconstructed from cells in jets with $p_T > 20$ GeV, with the LCW scale calibration and the jet energy scale factor applied.

- $E_{x,y}^{low-p_T jets}$ is reconstructed from cells in jets with 7 GeV $< p_T <$ 20 GeV

- $E_{x,y}^{CellOut}$ is calculated from the cells in topoclusers that are not included in the reconstructed objects

MET is used in the analysis section of this thesis, Chapter 7.

4.6 Jets and the Anti-k_T jet clustering algorithm

A typical high-energy collision produces a large number of energy deposits in the ATLAS calorimeter. The method of grouping a set of energy clusters together to form a single physics object can have a visible impact on the resulting physics. One common clustering algorithm used by ATLAS, anti-k_T, simplifies the structure of hadronic collisions and produces well-shaped conical jets that are infrared safe. Particle clustering algorithms generally define two distances, d_{ij} between entities (particles, pseudojets) i and j and d_{iB} between entity i and the beam (B) :

$$\begin{aligned} d_{ij} &= \min(k_{ti}^{2p}, k_{tj}^{2p})\frac{\Delta_{ij}^2}{R^2} \\ d_{iB} &= k_{ti}^{2p}, \end{aligned}$$

where $\Delta_{ij}^2 = (y_i - y_j)^2 + (\phi_i - \phi_j)^2$ and k_{ti}, y_i, ϕ_i are the transverse momentum (p_T), rapidity, and azimuthal angle of the i^{th} object, respectively. An R=0.4 is taken for the radius parameter. The value of p= -1 defines the anti-k_T implementation, where p is the relative power of the energy as a function of geometrical scale.

The clustering is performed by iterating over all particles i, in order of highest to lowest p_T. A second iteration is performed over all particles j, $j \neq i$, and the distances are calculated. If $d_{ij} < d_{i,B}$ the j^{th} object is merged into object i. If $d_{ij} > d_{i,B}$, object i is a final state jet and is no longer included in the iterations. The distances are recalculated and the procedure is repeated until there are no objects left [11].

The performance of the anti-k_T algorithm is such that low-p_T particles tend to cluster with high-p_T ones rather than clustering amongst themselves. This works well in a situation where there are many soft jets and a few hard jets, as is the case in events of interest at ATLAS. The anti-k_T algorithm results in circular hard jets, with radius R, and soft jets with more complicated shapes. This feature is unique to the anti-k_T algorithm, and is an improvement over other methods like the SISCone and Cambridge/Aachen that were previously in use. Typical results are shown in Figure 4.5.

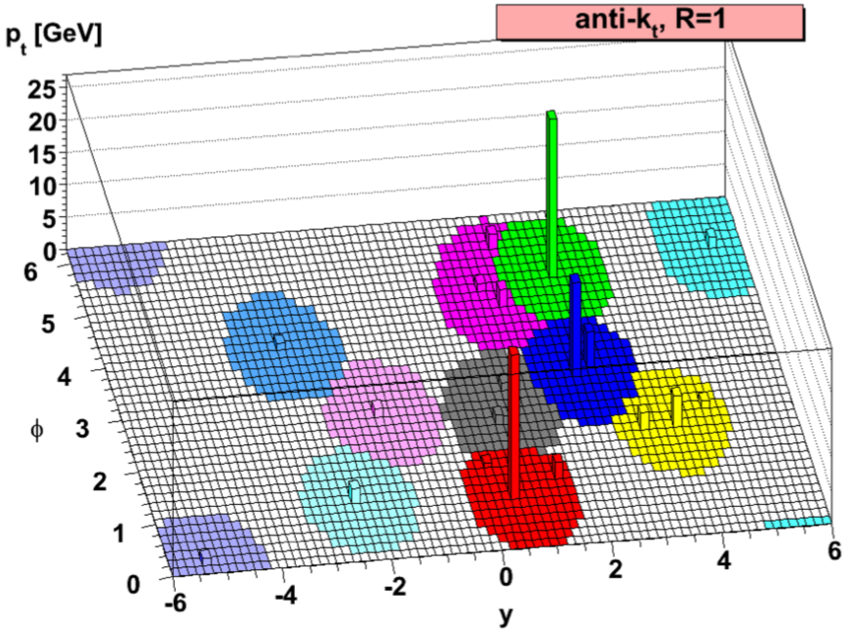

Figure 4.5: A hypothetical parton-level event generated with HERWIG, together with a number of soft ghost jets and a few high-p_T jets. The active catchment areas that result in hard jets are illustrated. The pair of jets near $\phi = 5$ and y = 2 provides an interesting example of the circularity of jets with respect to their momentum. The magenta cresent-shaped jet is much softer than the jet in green. Anti-k_T, rather than placing the boundary between two neighboring jets roughly midway between them, generates instead a circular hard jet. The circular hard jet(in green) cuts out a crescent-shaped region from the soft jet(in pink) [11].

4.7 B-tagging

The ability to identify jets originating from bottom quarks is important to many analyses at ATLAS. The algorithms take advantage of the B-hadron lifetime and variables like the impact parameter (IP) of the jet's tracks and the tracks' secondary verticies(SV).

The transverse impact parameter d_0 is the distance of closest approach between the track and the primary vertex in the r-ϕ plane. The corresponding z coordinate of closest approach $|z_0|sin\theta$ is the longitudinal impact parameter. The reference point from which the impact parameters and vertex displacements are measured is the primary interaction point (primary vertex) of the proton-proton collision [38].

An impact parameter-based algorithm IP3D, which employs a likelihood ratio method, was used in the low pile-up ATLAS data-taking conditions of 2010. Afterwards, SV-based algorithms were developed to further increase discrimination power between b-jets and light jets. SV0 was used in 2010 and following that SV1, which took advantage of three features of b-jet vertex properties. These features are the invariant mass of all tracks associated to the vertex, the ratio of the sum of the energies of the tracks in the vertex to the sum of the energies of all tracks in the jet, and the number of two-track verticies.

After IP3D, SV0, and SV1, ATLAS developed a new algorithm called JetFitter, which was used early into the 2011 analyses. JetFitter and JetFitterCombNN exploit the jet substructure by looking at the topology of b-hadron decays within the jet. The IP3D, SV1, and JetFitter algorithms can be combined by adding the output weights of the individual tagging algorithms. The MV1 b-tagging algorithm is one such amalgamated algorithm. MV1 is based on a neural network using, as inputs, the output weights of the JetFitter+IP3D, IP3D and SV1 algorithms [38].

In the analysis described in Chapter 7, the MV1 b-tagging algorithm is used. The working point, MV1 > 0.601713, has a b-jet efficiency of 69.6%, a purity of 0.912, a light quark rejection factor of 134, a charm quark rejection factor of 5 and a τ rejection factor of 13 [38].

Chapter 5

Tau Reconstruction and Identification

This chapter is dedicated to hadronically-decaying τ reconstruction and identification methods. There is a single τ reconstruction algorithm that seeds three τ identification(ID) algorithms, cut-based ID, projective likelihood (LLH) ID, and ID with boosted decision trees (BDT). The electron veto, described in Chapter 6, is also part of the Tau ID procedure.

5.1 Tau Reconstruction and Tau Energy Scale

The τ reconstruction algorithm is seeded from jets reconstructed with the anti-k_t algorithm, described in Section 4.7, with R = 0.4, from topological clusters of calorimeter cells. The clusters are calibrated using the Local Hadron Calibration (LC). Jets in $|\eta| < 2.5$ with $p_T > 10$ GeV are considered for seeding reconstructed τs [12].

Tracks are associated to each τ candidate in the area within $\Delta R < 0.2$ from the core cone axis, shown in Figure 5.1, and must pass the following threshold and quality criteria:

- $p_T > 1$ GeV
- $d_0 < 1$ mm

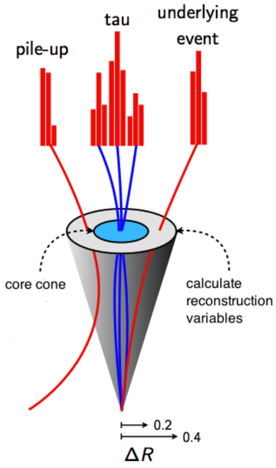

Figure 5.1: A cartoon of a τ cone. Note that pile-up and the underlying event also come into play when constructing the τ candidate. The number of tracks within the core cone classifies τs as either single or multi-prong. Tracks within the isolation annulus, defined as $0.2 < \Delta R < 0.4$ from the τ candidate axis, are also used in the calculation of discriminating variables. Image Courtesy: Ryan Reece, University of Pennsylvania

- $|z_0 \sin\theta| < 1.5$ mm
- at least two hits in the Pixel layer and at least seven hits in the Pixel and SCT layers combined

where d_0 is the distance of closest approach of the track to the reconstructed primary vertex after projecting both onto the transverse plane and z_0 is the longitudinal distance of closest approach [12].

The reconstructed four-momentum of the τ candidate is defined in terms of three degrees of freedom: p_T from tracking in the Inner Detector, and η and ϕ. The η and ϕ are taken from the sum of the four-vectors of the constituent topological clusters, described below, after corrections by the energy calibration procedure. During this calculation the topological clusters and the τ candidate are taken to be massless. Thus, with this definition, the τ p_T and E_T are identical, and sometimes used interchangeably with τ analyses at ATLAS.

Hadronic τ decays consist of a well-known, and distinct from typical jet composition, combinations of charged and neutral pions. Therefore the Tau Energy Scale(TES) for τs is calibrated independent of the jet energy scale [39]. The LC scale, used as the initial τ calibration, accounts for the energy deposits outside the reconstructed clusters and applies calibration weights to compensate for them. The LC improves τ energy resolution but does not fully restore the τ energy scale. The TES is an additional correction that is applied, derived from simulation samples of processes with τ final states, and verified in data. The TES looks at clusters only within the smaller τ cone of $\Delta R < 0.2$, thus reducing pile-up dependence, and from these clusters creates a new four-vector. A τ response curve is derived, as the ratio of the reconstructed τ energy at LC scale divided by the true τ visible energy. This provides the additional τ energy calibration factor that is applied on the τ four-vector [12].

5.2 Tau Identification

This section describes the QCD jet discrimination methods used in Tau ID. Three working points: loose, medium and tight are provided for each Tau ID method, which yield signal efficiencies of about 60%, 45% and 30%, respectively.

The cut-based Tau ID was developed for early data-taking and analysis at ATLAS, and has since been made more pile-up robust. This was done by parameterizing the variables in this ID algorithm by the p_T of the τ candidate. Two of the three variables in the cut-based Tau ID quantify the width of the hadronic shower, making use of the narrow signature of τ cones compared to those of QCD jets. In this thesis, the cut-based Tau ID was used only in the development of the misidentification probabilities in Section 6.2. More complex multivariate Tau ID algorithms were developed to increase signal efficiency for a given background rejection factor.

The LLH Tau ID for jet discrimination uses a log-likelihood ratio between signal and background as the discriminant. The likelihood function is a product of the one-dimensional probability density functions, $p_{x_i}^{S(B)}$, of each of the identification variables x_i. Each of the $p_{x_i}^{S(B)}$s is the fraction of events per bin in a histogram of the x_i distribution. The resulting log-likelihood ratio is shown in Figure 5.2.

The BDT for jet discrimination is trained using a package for multivariate analysis in the ROOT analysis toolkit, and BDT theory and implementation is described in Chapter 6. The BDT method uses a series of discriminating variables and defines a score between 0 and 1, which describes an event's signal-ness or backround-ness. Distributions of the jet BDT score are shown in Figure 5.2.

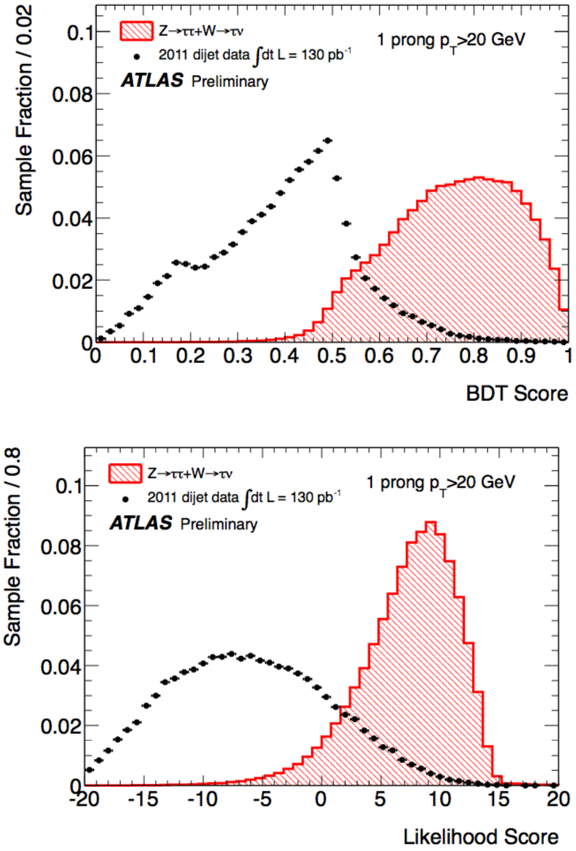

Figure 5.2: The BDT(top) and LLH(bottom) ratios for reconstructed τ candidates from dijet (background) data samples and MC τ (signal) samples [12].

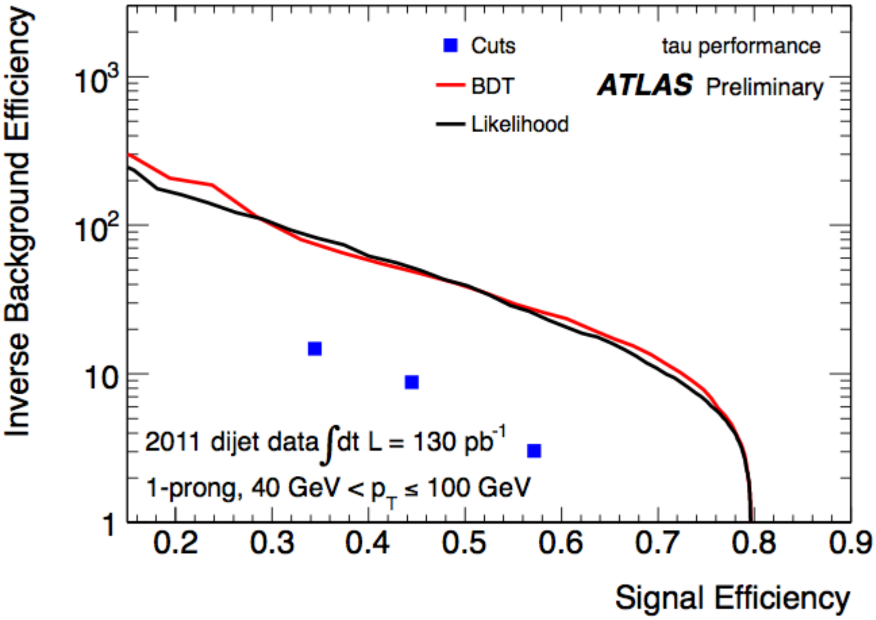

Figure 5.3: The performance of the jet discriminants for Tau ID on 1-prong reconstructed τ candidates from a sample of dijet events [12].

This thesis makes use of both the LLH and BDT Tau identification algorithms for jet discrimination, though results shown in Chapter 8 use the BDT jet Tau ID.

Chapter 6

Electron Vetoes as Part of Tau Identification

The characteristic signature of hadronically decaying 1-prong τ leptons can be mimicked by electrons. Thus electrons can constitute a significant fraction of the τ candidates after the jet related backgrounds are suppressed by kinematic, topological and τ identification criteria. Despite the similarity of τ lepton and electron signatures, there are several properties that can be used to distinguish between them. The most useful are the different interactions in the TRT between pion and electron tracks and the fact that the shower produced by a pion from a τ decay in the calorimeter tends to be longer and wider than an electron-induced shower. These and other properties can be used to define tau identification discriminants specialized in rejecting electrons.

This section describes the cut-based electron veto, followed by my work quantifying the misidentification probabilities, and finally my contributions creating, developing, and implementing the first two versions of the multivariate electron veto at ATLAS that were used in 2011 physics analyses with τs.

6.1 Cut-Based Electron Veto

A dedicated cut-based electron veto is available, along with a jet discriminator, as part of the ATLAS τ ID. The cut-based electron veto is based on the following variables:

- E_{max}^{strip}: The maximum energy deposited in the strip layer of the electromagnetic calorimeter, not associated with that of the leading track.

- $\frac{E_{EM}}{p^{Ltrk}}$: The ratio between the energy deposited in the electromagnetic calorimeter and the momentum of the leading track.

- $\frac{E_{Had}}{p^{Ltrk}}$: The ratio between the energy deposited in the first layer of the hadronic calorimeter and the leading track momentum.

- $\frac{N_{HT}}{N_{LT}}$: The ratio of high-threshold to low-threshold hits in the TRT, for the region of $|\eta| < 1.7$ only.

The distributions of these variables in data and MC are given in Figure 6.1. They are defined algebraically in Section 6.4.1. Good agreement is observed between data and MC for the three variables E_{max}^{strip}, $\frac{E_{EM}}{p^{Ltrk}}$ and $\frac{E_{Had}}{p^{Ltrk}}$. In the TRT ratio distribution, $\frac{N_{HT}}{N_{LT}}$, a significant shift to higher values is observed in the data. This shift can mainly be attributed to electron candidates falling in the TRT region with $|\eta| > 0.8$. This issue was addressed by the TRT performance group, and fixed in later releases of ATLAS software.

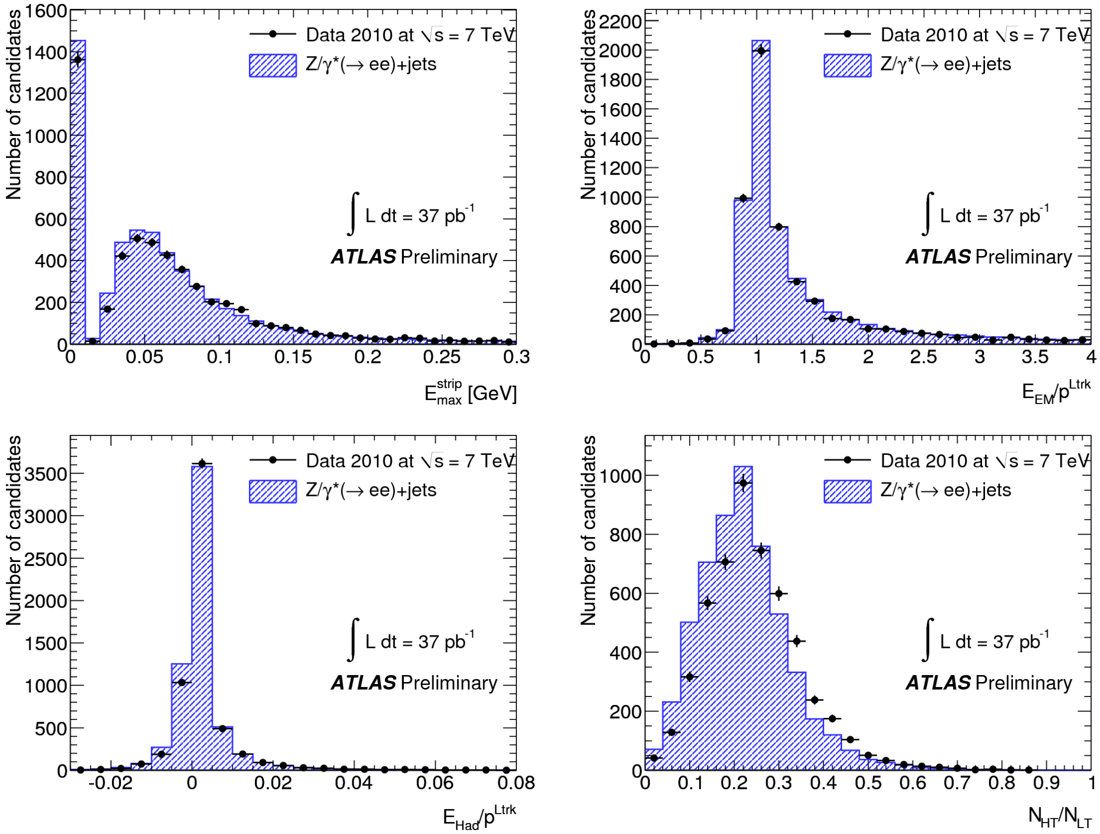

Figure 6.1: The four variables used in the cut-based electron veto. The dots are 2010 data and the shaded areas represent the signal prediction from MC simulation after $Z \to ee$ selection. Backgrounds investigated included W and Z→ $\tau\tau$ events and QCD jet events, which were found to be negligible [13].

6.2 Misidentification Probabilities

The tag-and-probe method is commonly used to calculate efficiencies and fake rates. The two physics objects, the "tag" and the "probe," occur in the same process and are related to each other in some uniform way like, for example, results from a decay. The tag object is required to pass strict quality criteria, ensuring the object is well understood. The complementary physics object, the probe, is largely unbiased in order to probe the efficiency of a selection or veto. In the scenario below, two electrons are required to form a same-flavor, opposite-sign pair within some mass-window of the Z-mass. The tag and probe objects are bound together by some relationship, in this case, a reconstructed invariant mass $M_{ee} \approx M_Z$ if they come from a true Z→e e process.

6.2.1 Tag and Probe with the Cut-Based Electron Veto

In order to measure the performance of the electron veto in data, a tag-and-probe method is used based on Z→e e events. The full event selection, method and results are described in [12] and [13].

Events are selected that pass the electron trigger requirements on the Event Filter level with a threshold of $E_T \geq 15$ GeV and medium identification criteria. The electron candidate, the tag, firing the trigger is required to have $p_T > 30$ GeV and $|\eta| < 2.47$, excluding the transition crack region in the electromagnetic calorimeter and calorimeter regions that are known to be not fully operational. This tag electron has to satisfy tight identification criteria and has to be isolated, within a cone of $\Delta R < 0.4$, from the other objects in the event. Finally, the product of the electric charge of the tag and probe objects is required to be negative, ensuring that they are opposite sign.

A reconstructed τ candidate with $p_T > 15$ GeV and $|\eta| < 2.5$ is selected as the probe. It has to have exactly one track associated to it as is expected for electrons. Note that three-prong τ candidates are unlikely to be electrons. The p_T distribution of the probe at the τ energy scale is given in Figure 6.3, and shows good agreement between simulation and data. The invariant mass of the tag and the probe electron after the event selection is displayed in Figure 6.4. Note the lack of a peak in same sign tag and probe pairs in Figure 6.5.

In case more than one pair of tag-and-probe objects is found in the event, the pair with the highest scalar sum of E_T is chosen. In addition, the invariant mass of the tag-and-probe pair, calculated using the energy at the electromagnetic scale, is required to fall inside the mass window $80 < \mathcal{M}_{ee} < 100$ GeV. In order to suppress remaining backgrounds, mainly from W → e ν processes, $E_T^{miss} \leq 20$ GeV is required, where the missing energy in the event is calculated from the vector sum of all calorimeter cells associated to clusters in the region $|\eta| < 4.5$, corrected for identified muons.

The probe candidates, satisfying the criteria above, are then subjected to the τ identification algorithms and to the electron veto in order to determine the misidentification probability of electrons as hadronically decaying τ leptons. The misidentification probability is defined as:

$$f_{\mathrm{ID}} = \frac{\text{Number of probe candidates passing electron veto and } \tau \text{ ID}}{\text{Number of probe candidates}}.$$

In general, the influence of pile-up on the misidentification probability of electrons as τ leptons in 2010 data was found to be small. The misidentification probability remained nearly flat with the number of pile-up verticies.

6.2.2 Results

The probabilities are provided for loose and tight working points for two types of τ ID: cut-based and BDTj. They are shown in Figure 6.6 as a function of p_T and in Figure 6.7 as a function of pseudorapidity.

6.2.3 Scale Factors with the Cut-Based Electron Veto

Scale factors, used to compensate for differences in simulation and 2010 data, were also computed and provided for the Tau Working Group. They were used in a number of analyses throughout the Tau Working Group as a source of the systematic uncertainty of the method.

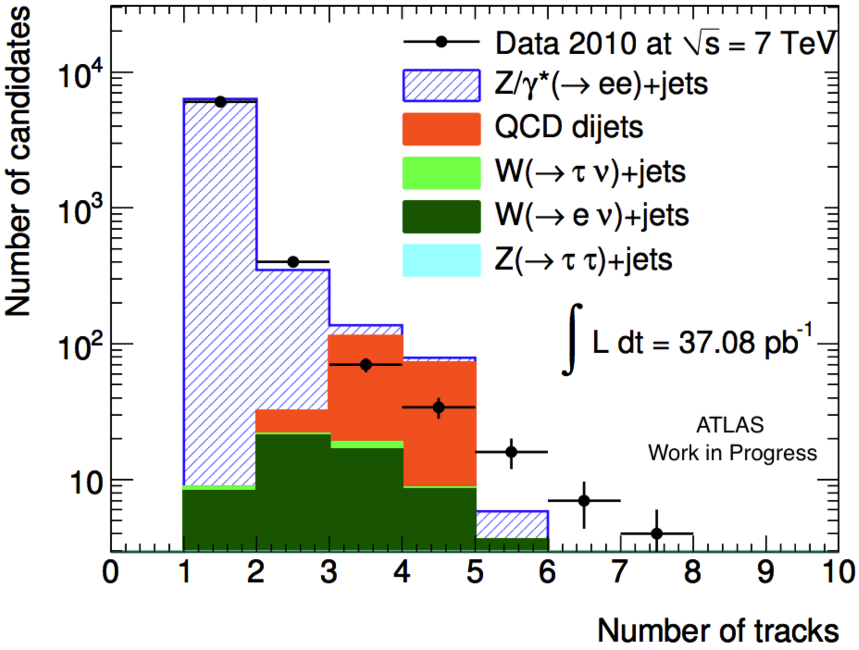

Figure 6.2: The number of tracks associated to the probe candidate before the requirement of exactly one track. The dots are the data and the predictions from MC are displayed as shaded histograms. This shows that the single track reconstructed τ candidate category is the one most contaminated by electrons.

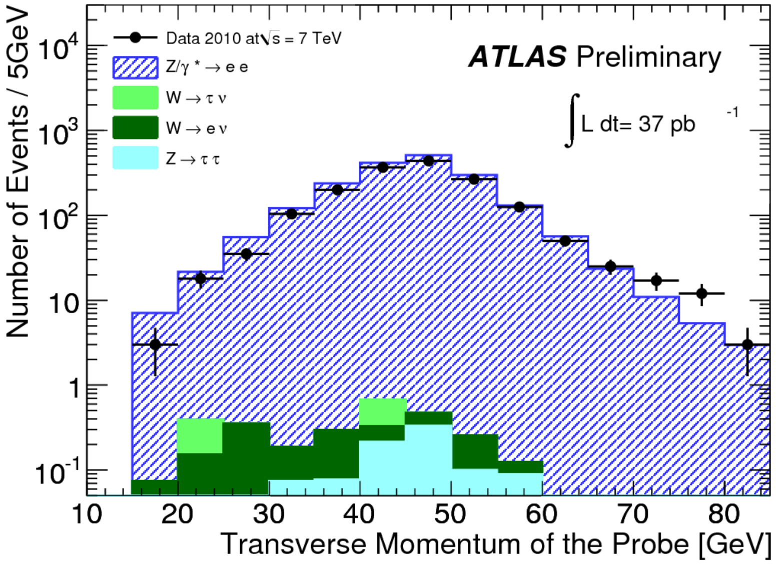

Figure 6.3: Distribution of the p_T of the probe object. The dots are the data and the predictions from MC are displayed as shaded histograms.

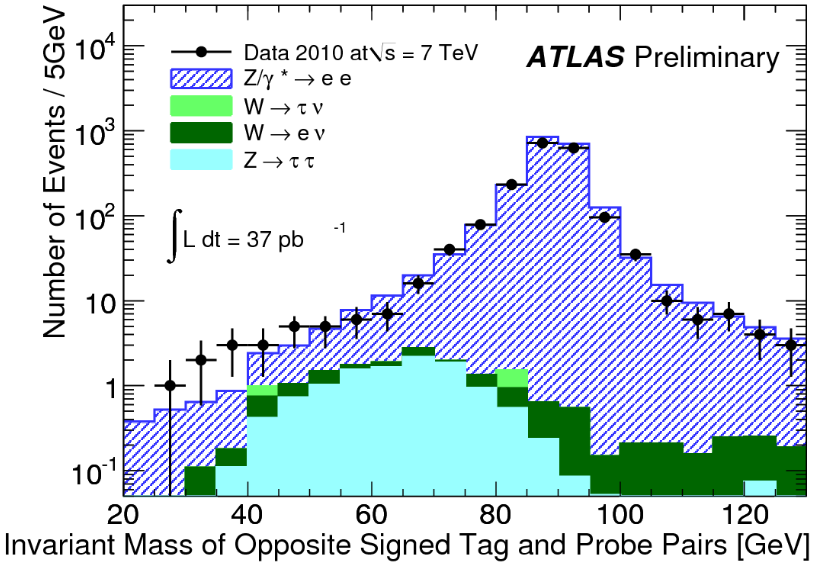

Figure 6.4: Distribution of the invariant mass of the tag-and-probe pair, calculated at the electromagnetic scale. The dots are the data and the predictions from MC are displayed as shaded histograms.

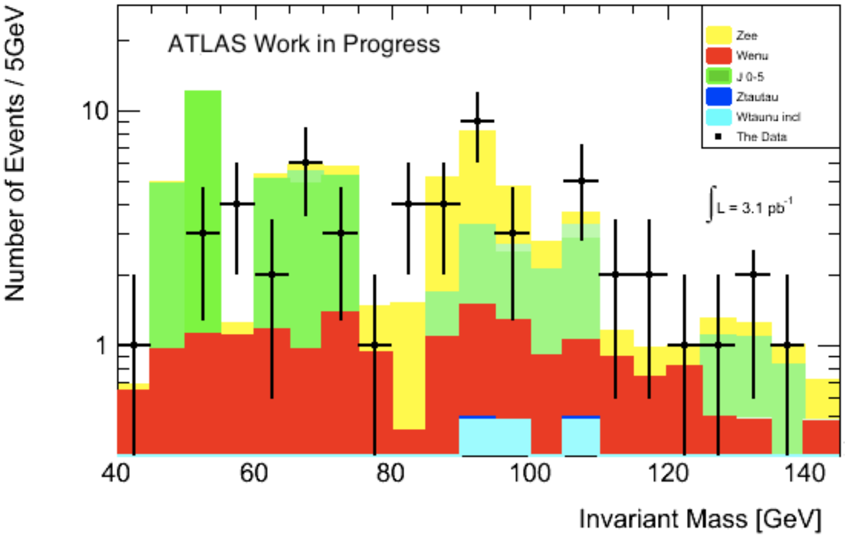

Figure 6.5: Distribution of the invariant mass of same-signed tag-and-probe pairs.

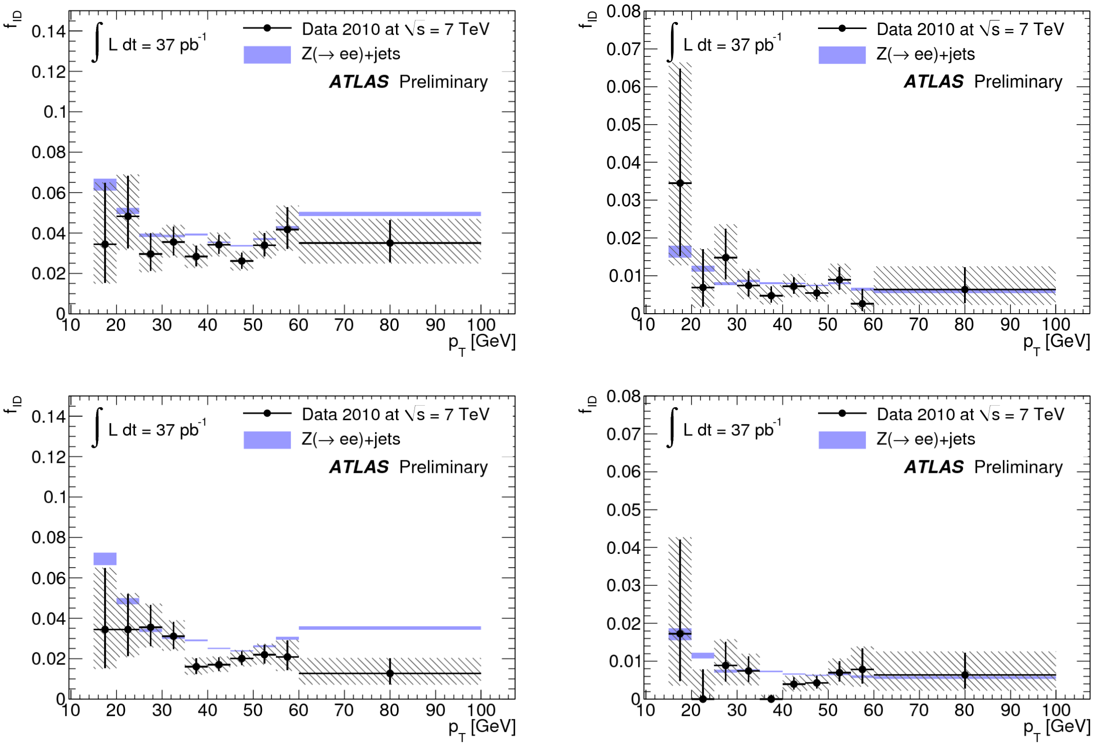

Figure 6.6: Misidentification probabilities as a function of p_T of the probe object. Top: additionally applied cut-based Tau ID, Bottom: additionally applied BDTj Tau ID , Left:Loose working point Right:Tight working point.

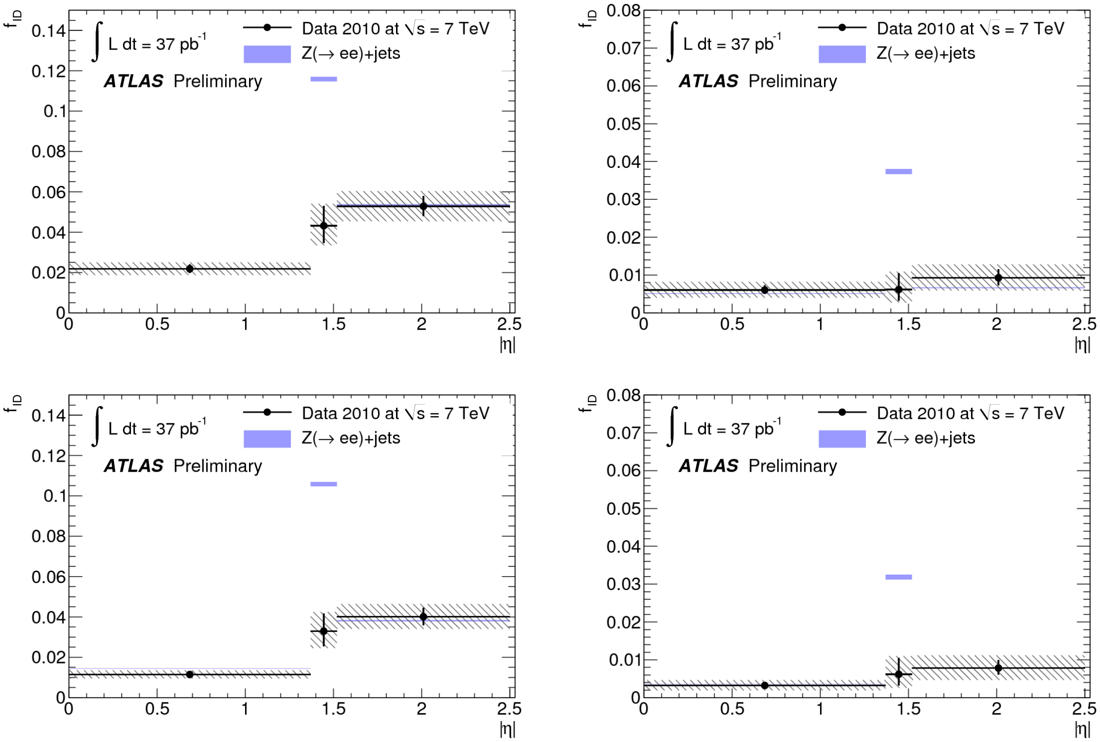

Figure 6.7: Misidentification probabilities as a function of the probe object's location in the ATLAS Detector. Top: additionally applied cut-based Tau ID, Bottom: additionally applied BDTj Tau ID, Left: Loose working point, Right: Tight working point. The mismatch between data and MC for the crack region in $|\eta|$ was known and corrected for in later releases of ATLAS software.

6.3 The Multivariate Boosted Decision Tree Method

6.3.1 Decision Tree Theory

A Decision Tree [40] is a machine-learning technique that creates a specialized set of criteria over many variables to extract small signals from larger and similar signature backgrounds. The output of the technique is a single powerful discriminator composed from a set of several weaker discriminating variables. Furthermore, whereas a cut-based analysis is able to select only a single hypercube region in phase space, the decision tree is able to split phase space into a number of hypercubes, each of which is signal- or background-like.

In general, a decision tree is a structure of cuts organized into nodes. A node is the decision point in the tree in which a variable and cut value are provided that the candidate either passes or fails. A schematic of nodes in a decision tree is shown in Figure 6.8. The pass or failure determines which node the candidate will encounter next. A tree begins at a root node and branches off to two secondary nodes corresponding to the pass or fail of the root node cut. Each of these nodes carries a cut qualification and a tested candidate would again advance from this node either to the left or right daughter node. Each cut path eventually stops at some terminal node with a qualifier value that will be assigned to the candidate. Repeated pass/fail decisions are taken on a single variable at a time until a stop criterion is fulfilled. Any event that fails a certain cut will continue being analyzed and will not be instantaneously disqualified as signal [41].

The technique notes the number of times each of the discriminating variables is used for making the final decision. The more nodes at which a variable is used in making the decision, the more highly-ranked the variable. This ranking can be used to determine the relative power of the discriminating variables. Each event is given a continuous decision tree score between 0 and 1.

The process of building a tree structure of cuts node-by-node is called training. Decision tree training uses input samples of known and pure signal and background training events, each with an equal weighting, w_s or w_b. A Gini index is used to quantify the separation between signal(S) and background(B) at any given node during the training. The Gini index is a function of the purity of the sample, which is a quotient of weighted sums of S and B events, given by Equation 6.1.

Purity, p:

$$p = \frac{S}{S+B} = \frac{\sum w_s}{\sum w_s + \sum w_b} \tag{6.1}$$

The tree stops growing, and the training terminates, when there become too many bins for the given training sample size.

6.3.2 Boosting

A Boosted Decision Tree (BDT) algorithm improves upon the decision tree technique from Section 6.3.1. One disadvantage of a decision tree algorithm is that small changes in the input training sample can lead to large changes in the resulting tree structure. Boosting addresses this effect by combining several decision trees and stabilizing the response of the decision trees with respect to fluctuations in the training sample, thus improving the performance with respect to a single tree [41, 40]. Boosting addresses the instances in training when a signal or background event is misclassified as the opposite.

Boosting uses the training results of the first tree to increase the importance, or weighting, of candidates that were misclassified. A new tree is then trained using these reweightings. The functional form is described in [42]. BDTs are also more stable because averaging over many trees reduces the statistical fluctuations introduced by limited training sample sizes.

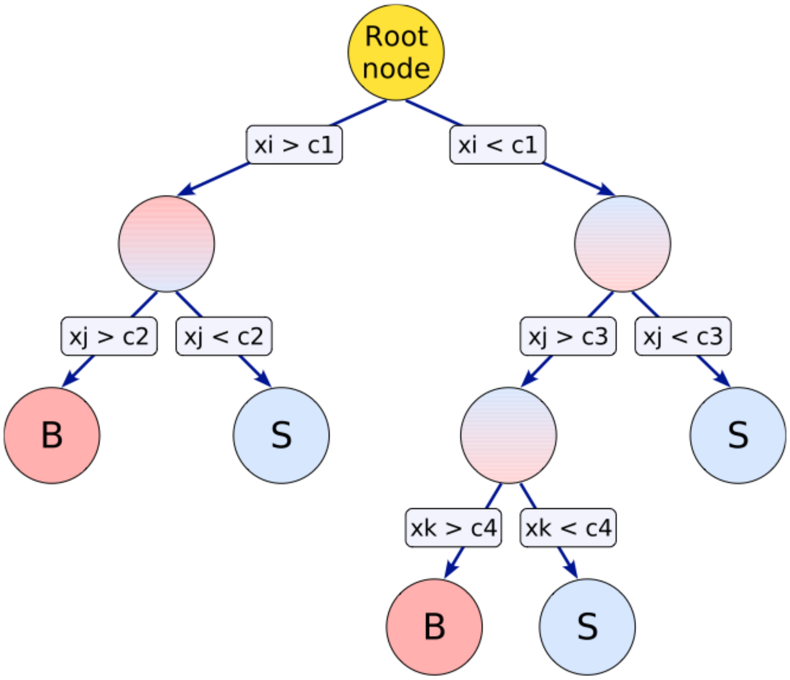

Figure 6.8: This is a schematic view of a decision tree. Starting from the root node, a sequence of binary splits using the discriminating variables $\{x_i, x_j, x_k \ldots\}$ is applied to the data. The determining variable used at each split is the one that gives the best separation between signal and background at that node. Thus different variables are used at a different number of nodes. The nodes at the bottom of the tree are labeled "S" for signal and "B" for background depending on the majority content of events in the respective nodes. The event is revealed to be more signal-like or more background-like with successive iterations of decisions [40].

AdaBoost [40], the boosting algorithm used in this thesis, has a strong ability to identify the instances of trees that have mislabeled input or are ambiguous and difficult to categorize in the training. Several parameters are used to tune the structure and degrees of freedom of the BDT, and are described in Section 6.3.3.

6.3.3 Parameters used for this BDT study

A large number of algorithm parameters [40] are available to finely-tune the BDT algorithm to the specific type of problem at hand. For this electron veto, the parameters were set to the following:

- NTrees=50 : Number of trees used and averaged-over in the boosting
- AdaBoost parameter β =0.2: Controls the strength of the re-weighting in the boost
- UseYesNoLeaf=False : Uses the purity as classification of the leaf node, as in Equation 6.1
- nEventsMin=200 : The minimum number of events required in the last node below which node splitting does not occur and the training terminates
- nCuts= ∞: No limit on the maximum number of steps during node cut-optimization
- Prune Method= No Pruning : The method used for removing statistically insignificant branches
- MaxDepth=1000000 : The maximum allowed depth of a decision tree

6.4 Using the Boosted Decision Tree as an Electron Veto

This section describes the electron discriminant using BDTs in Tau ID. The goal in developing a discriminant is to maximize the acceptance of true signal (τs) and minimize the acceptance of true background(electrons). If a simple cut-based selection is used, many true signal events would not pass the ideal criteria of standard cuts and many true background events would successfully pass the criteria by chance. A BDT is able to salvage some of the signal candidates that would otherwise be lost, thus maximizing the acceptance. Simultaneously the BDT gets rid of background events that would otherwise pass, in a more straightforward veto. As described previously, the BDT does this by reconsidering candidates for further analysis. In this case, the BDTe is used to as a discriminant to separate signal candidates, which are single-prong τ_{had}s, and the background, which are electrons.

I developed two versions of the BDTe at ATLAS, for Spring 2011 and for Fall 2011, for two rounds of ATLAS analysis cycles and data-format productions. The second version of the BDTe was tuned to accommodate for the modifications made in ATLAS-defined variables.

The BDT electron (BDTe) discriminant is optimized using MC simulated $Z \rightarrow \tau\tau$ events for signal and MC simulated $Z \rightarrow ee$ events for background. The signal candidates are required to match to a true hadronically decaying τ lepton and background candidates are required to match to a true electron, both within $\Delta R < 0.2$. All candidates are required to have $p_T > 20$ GeV. No medium or tight electron overlap removal has been performed in classifying these reconstructed τ candidates, though in later versions this was changed.

The signal efficiency used for the performance evaluation for the Spring 2011 edition is defined in the following equation:

Signal efficiency:

$$\varepsilon_{\text{sig}}^{\text{1-prong}} = \frac{\left(\text{\# of true 1-prong taus reconstructed as 1-prong tau candidates passing loose cut-based tau ID and BDTe}\right)}{\left(\text{\# of true 1-prong taus reconstructed as 1-prong tau candidates passing loose cut-based tau ID}\right)}$$

6.4.1 Tau Identification Variables used in BDTe

The BDTe uses discriminating variables that are calculated during the reconstruction [12, 43, 44].

The following variables were used in the BDTe training and discrimination: f_{HT} , f_{EM}, 1 / f_{track}, R_{track}, f_{PS}, f_{iso} , $f_{\text{EM}}^{\pi^{\pm}}$, and R_{had}. Their distributions are provided and shown in Figures 6.9, 6.10, and 6.11. In Figure 6.9, the distributions are shown for all four regions of η in BDTe training, as an example.

A tag and probe method in Z→ ee was used to obtain an electron-enriched sample in data. Three samples of reconstructed τ candidates, MC τs, MC electrons, and electrons from data, are shown in Figures 6.9, 6.10, and 6.13. The distributions from the electrons in data are in good agreement with the distributions from electrons in MC, giving confidence that the BDTe method can be trusted and used in physics analyses.

Hadronic radius "hadRadius" R_{had} : Transverse energy weighted shower width in the hadronic calorimeter

$$R_{\text{Had}} = \frac{\sum_{i\in\{\text{Had}\}}^{\Delta R_i<0.4} E_{\text{T},i}^{\text{EM}}\,\Delta R_i}{\sum_{i\in\{\text{Had}\}}^{\Delta R_i<0.4} E_{\text{T},i}^{\text{EM}}},$$

where i runs over cells in the hadronic calorimeter and also the final layer of the EM calorimeter. The energy is calibrated at the EM scale. Only cells in a cone of $\Delta R < 0.4$ around the cluster barycenter are considered.

Track radius "trkAvgDist" (R_{track}): p_T weighted track width:

$$R_{\text{track}} = \frac{\sum_i^{\Delta R_i<0.4} p_{\text{T},i}\,\Delta R_i}{\sum_i^{\Delta R_i<0.4} p_{\text{T},i}},$$

where i runs over all core and isolation tracks of the τ candidate, within $\Delta R_i < 0.4$. ΔR_i is defined relative to the τ jet seed axis and $p_{\text{T},i}$ is the track transverse momentum. Note that for candidates with only one track in the core cone and isolation annulus, R_{track} simplifies to the ΔR between the track and the axis of the seed jet.

Leading track momentum fraction "etOverPtLeadTrk" (f_{track}):

$$f_{\text{track}} = \frac{p_{\text{T},1}^{\text{track}}}{\sum_{j\in\{\text{all}\}}^{\Delta R_j<0.4} E_{\text{T},j}^{\text{EM}}},$$

where $p_{\text{T},1}^{\text{track}}$ is the transverse momentum of the leading p_T core track of the τ candidate and j runs over all cells in $\Delta R < 0.4$. The cell calibration at the EM scale is used.

Note that for candidates with one track, f_{track} is the fraction of the candidate's momentum attributed to the track, compared to the total momentum of the candidate, which can have contributions from the calorimeter deposits from π^0s and other neutrals.

Core energy fraction "centralityFraction" (f_{core}): Fraction of transverse energy in the core ($\Delta R < 0.1$) of the τ candidate:

$$f_{\text{core}} = \frac{\sum_{i\in\{\text{all}\}}^{\Delta R_i<0.1} E_{\text{T},i}^{\text{EM}}}{\sum_{j\in\{\text{all}\}}^{\Delta R_j<0.4} E_{\text{T},j}^{\text{EM}}},$$

where i runs over all cells associated with the τ candidate within $\Delta R < 0.1$ of the τ jet seed axis and j runs over all cells in $\Delta R < 0.4$. The cell calibration at the EM scale is used.

Electromagnetic fraction "EMFractionAtEMScale" (f_{EM}): Fraction of transverse energy of the τ candidate deposited in the EM calorimeter:

$$f_{\mathrm{EM}} = \frac{\sum_{i \in \{\mathrm{EM}\ 0-2\}}^{\Delta R_i < 0.4} E_{\mathrm{T},i}^{\mathrm{EM}}}{\sum_{j \in \{\mathrm{all}\}}^{\Delta R_j < 0.4} E_{\mathrm{T},j}^{\mathrm{EM}}},$$

where $E_{\mathrm{T},i}$ ($E_{\mathrm{T},j}$) is the transverse energy, calibrated at the EM energy scale, deposited in cell i (j), and i runs over the cells in the first three layers of the EM calorimeter, while j runs over the cells in all layers of the calorimeter.

TRT HT fraction "TRT Ratio" (f_{HT}): The ratio of high-threshold to low-threshold hits (including outlier hits), in the Transition Radiation Tracker (TRT), for the leading p_T core track. Since electrons are lighter than pions and have higher Lorentz γ factors, they are more likely to produce the transition radiation that causes high threshold hits in the TRT. This variable is the most powerful discriminator between hadronic 1-prong τ candidates and electrons and appears highest in the rankings shown in Section 6.4.2.

Ring isolation "isolFraction" (f_{iso}):

$$f_{\mathrm{iso}} = \frac{\sum_{i \in \{\mathrm{all}\}}^{0.1 < \Delta R < 0.2} E_{\mathrm{T},i}^{\mathrm{EM}}}{\sum_{j \in \{\mathrm{all}\}}^{\Delta R < 0.4} E_{\mathrm{T},j}^{\mathrm{EM}}}.$$

where i runs over calorimeter cells in the associated topocluster of the τ candidate in an annulus within $0.1 < \Delta R < 0.2$ around the seed and j runs over cells in a cone of $\Delta R < 0.4$. The energy is calibrated at the electromagnetic scale.

The following three variables are powerful in π^0 reconstruction, thus making them powerful discriminators between τs, which have π^0s as decay products, and electrons, which do not.

Electromagnetic energy over momentum of track system ($f_{\mathrm{P}}^{\mathrm{EM}}$):

$$f_{\mathrm{P}}^{\mathrm{EM}} = \frac{\sum_{l=0}^{N_{\mathrm{clus}}} E_{l}^{\mathrm{EM}}}{\sum_{i}^{\Delta R < 0.2} p_{i}^{\mathrm{trk}}}.$$

where l runs over the calorimeter clusters associated to the τ candidate, E_l^{EM} denotes the cluster energy deposited in the electromagnetic part of each cluster (presampler and first two layers) and i runs over tracks associated to the τ candidate in the core region. The cluster energy is calibrated at the LC scale.

Presampler strip energy fraction "PSSEOverCaloE" (f_{PS}):

$$f_{\mathrm{PS}} = \frac{\sum_{l=0}^{N_{\mathrm{clus}}} E_l^{\mathrm{PS}}}{\sum_{l=0}^{N_{\mathrm{clus}}} E_l}.$$

where l runs over calorimeter clusters associated to the τ candidate, E_l^{PS} denotes the part of the cluster energy, calibrated at the LC scale, deposited in the Presampler layer of calorimeter and E_l is the total energy of the calorimeter cluster.

EM energy of charged pions over EM energy "ChPiEMEOverCaloEME" ($f_{\mathrm{EM}}^{\pi^\pm}$):

$$f_{\mathrm{EM}}^{\pi^\pm} = \frac{\sum_{i}^{\Delta R<0.2} p_i^{trk} - \sum_{l=0}^{N_{\mathrm{clus}}} E_l^{\mathrm{Had}}}{\sum_{l=0}^{N_{\mathrm{clus}}} E_l^{\mathrm{EM}}}.$$

where l runs over calorimeter clusters associated to τ candidate, E_l^{Had} denotes the part of cluster energy deposited in the hadronic part of each cluster, E_l^{EM} is the cluster energy deposited in the electromagnetic part of each cluster (presampler and first two layers) and i runs over tracks associated to the τ candidate in the core region. All clusters are calibrated at the LC energy scale.

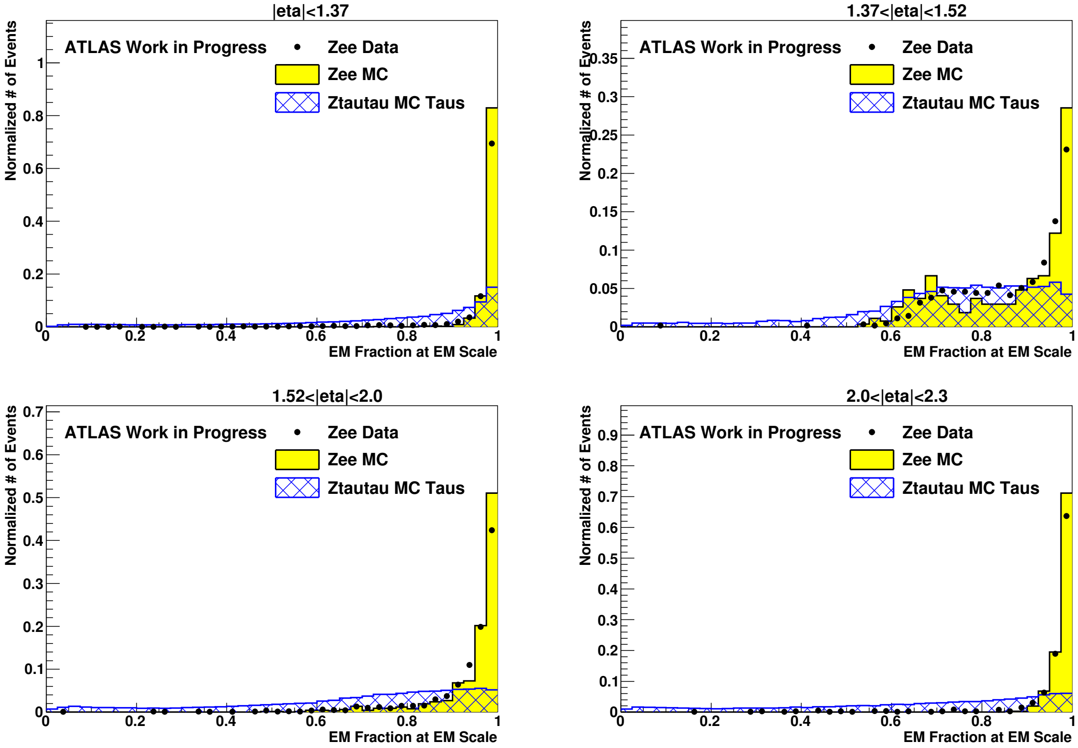

Figure 6.9: The variable EM Fraction at EM Scale, for the four regions of BDTe training. These are with 1-prong reconstructed τ candidates of $20 < p_T < 35$ GeV.

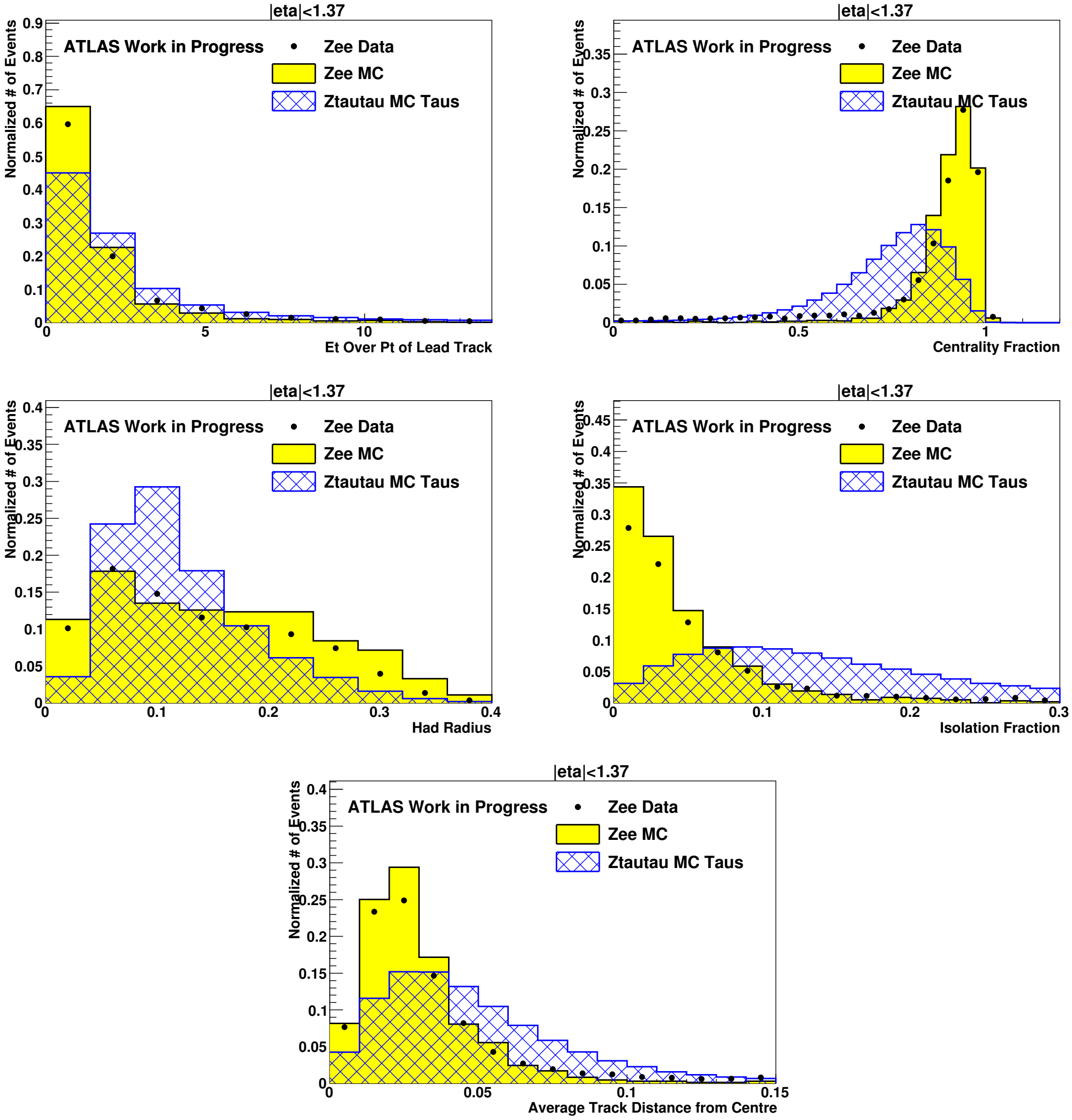

Figure 6.10: The distributions of 1-prong reconstructed τ candidates of $20 < p_T <$ 35 GeV in the barrel region of the ATLAS detector for f_{track} (top row,left), f_{core} (top row, right), R_{had}(second row, left) , f_{iso}(second row, right), and R_{track}(third row). The solid yellow distribution is for reconstructed τ candidates from a Z→ee MC sample, the hashed blue distribution is for reconstructed τ candidates from a Z→ $\tau\tau$ MC sample, and the dots are with 2010 ATLAS data passing a tag and probe selection. The tag and probe pairs have a reconstructed invariant mass 80 GeV $< M_{ee} <$ 100 GeV, which is around M_Z.

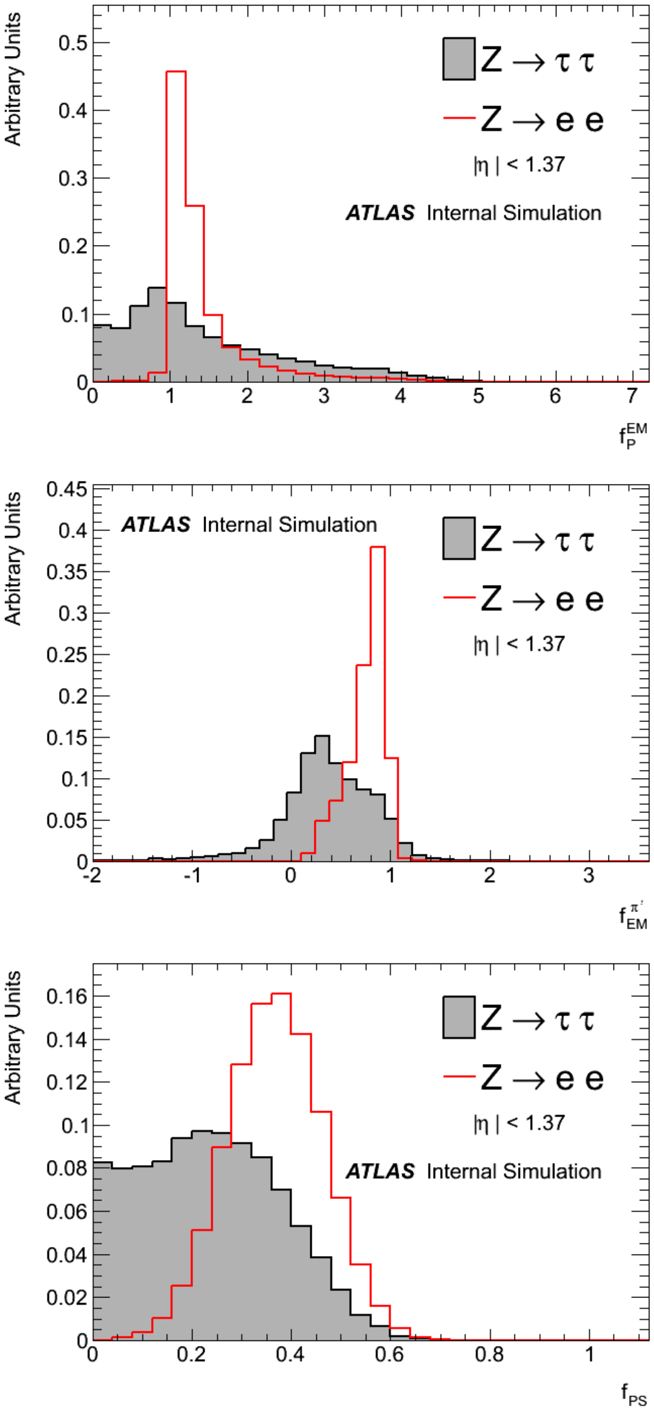

Figure 6.11: Three variables used in the BDTe training are specifically aimed at π^0 identification, thus playing a powerful role in discrimination of hadronically-decaying τs and electrons. These distributions are of reconstructed τ candidates with $p_T \geq$ 20 GeV located in the barrel region. Simulation is used for the distributions in these figures, with samples of Z bosons providing both τs and electrons [14].

6.4.2 BDTe performance results

After the training, the following performance studies were done to understand the power of the BDTe.

The variable rankings of the BDTe training, as described in section 6.3.1, are provided for the 4 regions in ATLAS in Figure 6.12.

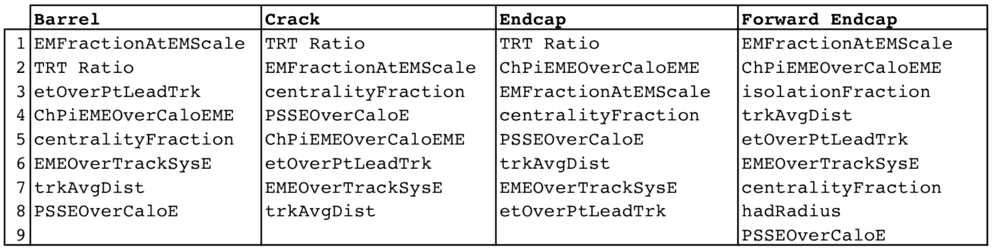

	Barrel	**Crack**	**Endcap**	**Forward Endcap**
1	EMFractionAtEMScale	TRT Ratio	TRT Ratio	EMFractionAtEMScale
2	TRT Ratio	EMFractionAtEMScale	ChPiEMEOverCaloEME	ChPiEMEOverCaloEME
3	etOverPtLeadTrk	centralityFraction	EMFractionAtEMScale	isolationFraction
4	ChPiEMEOverCaloEME	PSSEOverCaloE	centralityFraction	trkAvgDist
5	centralityFraction	ChPiEMEOverCaloEME	PSSEOverCaloE	etOverPtLeadTrk
6	EMEOverTrackSysE	etOverPtLeadTrk	trkAvgDist	EMEOverTrackSysE
7	trkAvgDist	EMEOverTrackSysE	EMEOverTrackSysE	centralityFraction
8	PSSEOverCaloE	trkAvgDist	etOverPtLeadTrk	hadRadius
9				PSSEOverCaloE

Figure 6.12: These are the variable rankings in order of relative importance. The more powerful the variable in making the decision between signal and background, the earlier it appears on the list. The rankings are provided in four regions: $|\eta| < 1.37$ (barrel) , $1.37 < |\eta| < 1.52$ (crack) , $1.52 < |\eta| < 2.0$ (endcap), and $|\eta| > 2.0$ (forward endcap).

The BDTe is effective in decreasing the number of electrons classified as reconstructed τ candidates, as shown in Figure 6.13.

The separation power of the BDTe discriminant is shown in Figure 6.14.

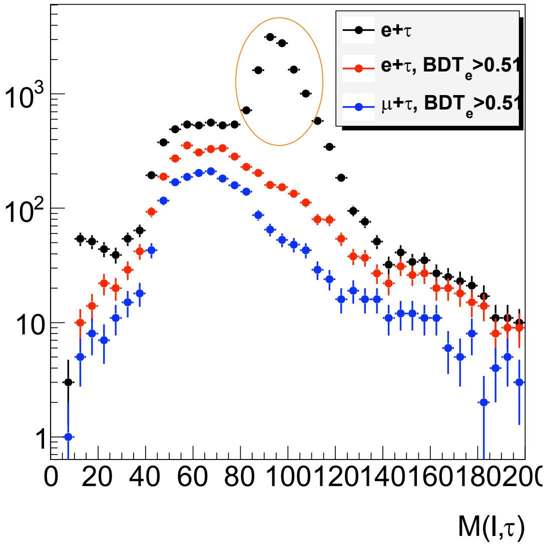

Figure 6.13: This plot shows the invariant mass between the lepton (e or μ) and the reconstructed τ candidate in 2011 data. After the application of the BDTe on the reconstructed τ candidates, the electron enriched (Z →ee) peak, containing reconstructed τ candidates (likely electrons faking τs), at 90 GeV is decimated.

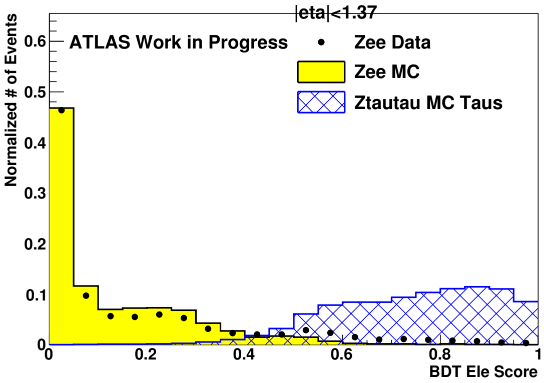

Figure 6.14: The BDTe score of 1-prong reconstructed τ candidates of $20 < p_T < 35$ GeV in the barrel region of the ATLAS detector.

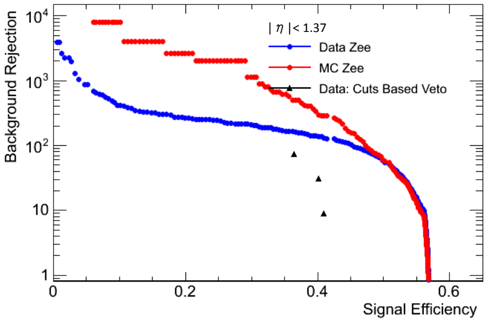

Figure 6.15: The curve of background rejection as a function of signal efficiency is shown. Each point describes signal candidates with a BDTe score larger than some value, which is then incremented. Increasing the BDTe score cut value increases background rejection and decreases the signal efficiency [14].

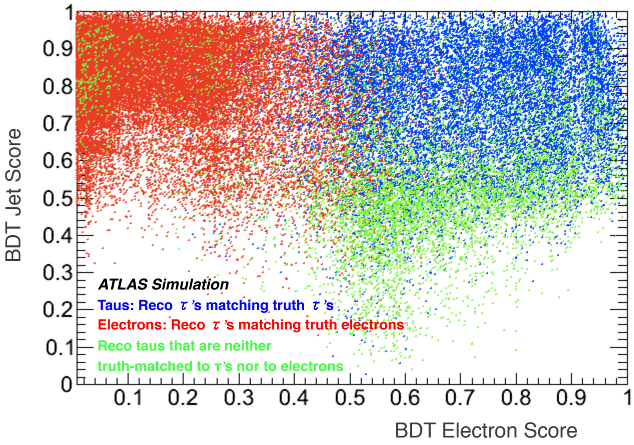

Figure 6.16: Shown is ATLAS simulation of objects passing loose τ candidate reconstruction. The reconstructed τ candidates have a single-track with $|\eta| \leq 2.3$ and $p_T \geq 20$ GeV. Reconstructed τ candidates are divided into three categories: those τ_{reco} within Δ R ≤ 0.2 of truth-level τs (in blue),those τ_{reco} within ΔR ≤ 0.2 of truth-level electrons (in red), and those τ_{reco} neither matched to truth-level τs or truth-level electrons (in green). A QCD-initiated jet is one type of object that could fall into the last category(green). The behavior is as expected for the three categories: truth-level electrons have low BDT Electron Score, truth-level τs have high BDT Electron Score. As electrons and jets leave quite disparate signatures within ATLAS, electrons have a high BDT Jet Score and jets have a high BDT Electron Score.

Chapter 7

Top to Tau Event Selection

The event selection described this chapter is optimized to select for $t\bar{t} \rightarrow \tau_{had}$+$\mu$+ $bb\nu\nu$ events at ATLAS, as shown in Figure 7.1.

Previous analyses, such as the so-called "ratio method", attempted to observe a preference for decays to the third generation in this channel and are described in [45] and [46]. Since W bosons decay to the three lepton generations equally, an excess would be evidence of physics beyond the SM and could point to the $H^{\pm}$, which violates lepton universality and favors τ leptons.

Event yield ratios between $t\bar{t} \rightarrow e\ +\ \tau_{had}$ and $t\bar{t} \rightarrow e\ +\ \mu$/e , as well as between $t\bar{t}$ $\rightarrow \mu\ +\ \tau_{had}$ and $t\bar{t} \rightarrow \mu\ +\ e/\mu$, final states were measured in data and compared to predictions from simulation. A limit was placed using these ratios with event yields, $\mathcal{N}$, of:

$$\text{BR}(\text{t}\rightarrow H^{\pm}_{130\ GeV}\ b) < 3.6\ \%$$

using the ratio $R_{e+\mu}$ where

$$R_{e+\mu} \equiv \mathcal{N}(t\bar{t} \rightarrow \tau_{had} + e + bb\nu\nu) + \mathcal{N}(t\bar{t} \rightarrow \tau_{had} + \mu + bb\nu\nu)/\mathcal{N}(t\bar{t} \rightarrow l + l' + bb\nu\nu),$$

for l $\in \{e, \mu\}$ and l$\neq l'$ [46].

The analysis described here uses μ+τ_{had} events to go beyond event yields and search for a $H^{\pm}$ by way of τ polarimetry.

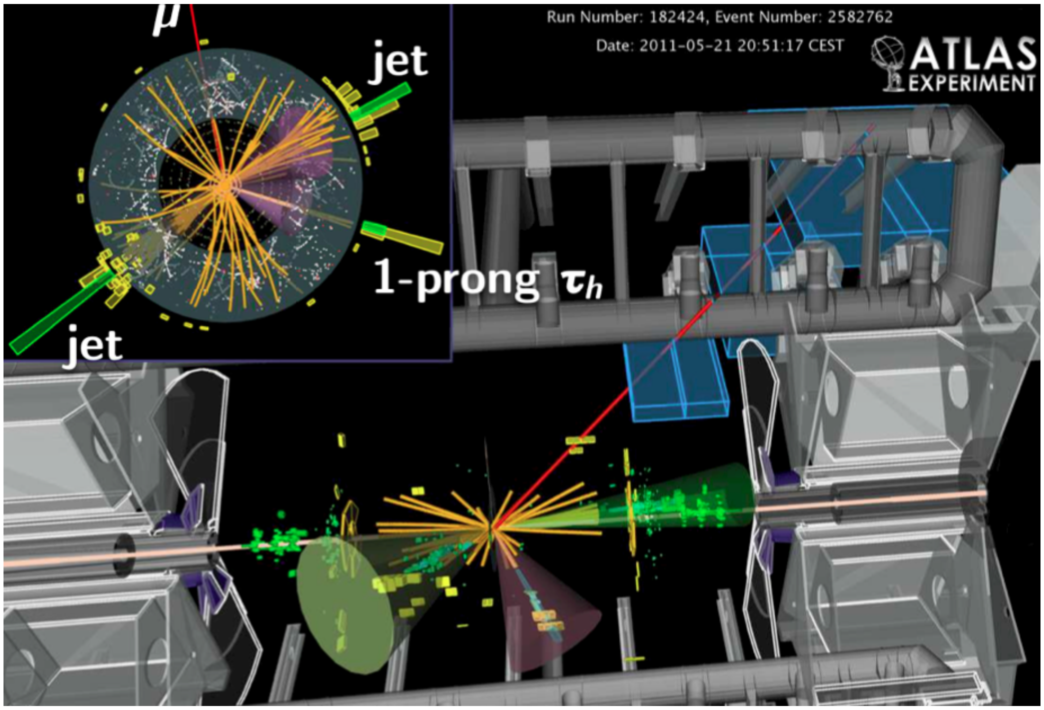

Figure 7.1: An event display of a $t\bar{t} \rightarrow \mu+$ 1-prong $\tau_{had} +$ $bb\nu\nu$ decay candidate, the signal for the event selection.

7.1 Monte Carlo Corrections

A number of corrections are applied to make the Monte Carlo(MC) samples comparable to the data.

- Pile-up Corrections: Simulation samples were overlaid with additional pile-up interactions. However, the distribution of average number interactions per bunch crossing, $< \mu >$, in MC does not exactly match the conditions delivered by the LHC beam, thus MC events are re-weighted to match the data-taking conditions. The $< \mu >$ profile is shown in Figure 3.11.
- Muon-Related Corrections: Scale factors (SFs) are applied to MC events to correct for discrepancies with measured trigger and muon ID efficiencies. These SFs, generally very near 1, are determined using a tag-and-probe study of the

Z decays. The SFs are parameterized by η and p_T. The closer the SFs are to 1, the smaller the MC mismodeling.

Additionally, the muon p_T resolution in MC differs from that measured in data. To correct for this difference, the muon p_T in MC is smeared and the resolution decreased.

- Liquid Argon Hole Related Corrections: An electronics failure in the LAr barrel calorimeter resulted in a long, thin dead region with coordinates $(0.0, -0.8) < \eta, \phi < (1.4, -0.8)$. This failure effected 84% of the dataset used in this analysis. Thus events with any good electrons or good jets falling inside the dead region are vetoed. Jet p_T in data is also increased by a correction factor to account for the unmeasured energy in the hole [47].

7.2 Samples

The processes, generators and corresponding cross sections are summarized in Table 7.1.

Name	Process	Generator	Cross Section
"T1"	SM $t\bar{t} \rightarrow WbWb \rightarrow \geq 1$ lepton	`MC@NLO`	89.7 pb
charged Higgs	$t\bar{t} \rightarrow H^- bWb$	`PYTHIA`	9.0 pb
charged Higgs	$t\bar{t} \rightarrow H^+ bWb$	`PYTHIA`	9.0 pb

Table 7.1: Monte Carlo $t\bar{t}$ events used in this analysis. Note the Charged Higgs samples are simulated for $m_{H^\pm} = 130$ GeV and have BR($H^\pm \rightarrow \tau\nu$)=100%. The "T1" sample does not include the fully-hadronic $t\bar{t}$ decay modes.

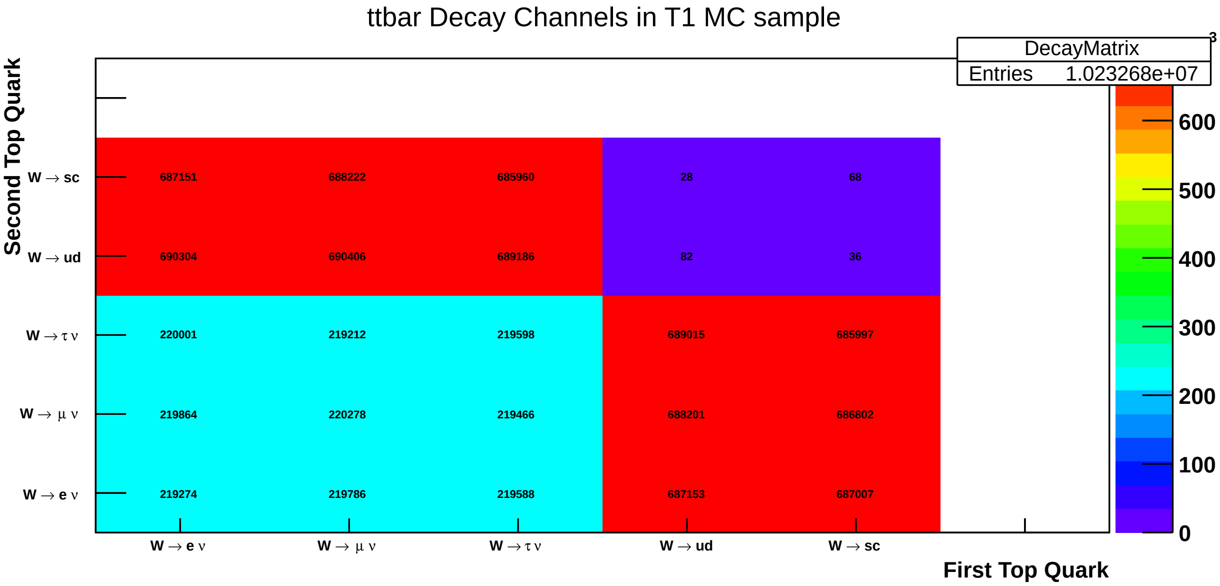

Figure 7.2: The decay processes in SM $t\bar{t}$ with ≥ 1 lepton MC sample. Each $t\bar{t}$ event decays to two W bosons, which can then decay leptonically or hadronically. Note the $W \rightarrow qq'$ modes are three times as populated, for the three possible color charges.

7.3 Particle Selection

A standard set of object selections is performed. Due to the complex nature of the final state, overlap removals are crucial.

7.3.1 Object Selection

Muons pass the following quality and identification criteria:

- reconstructed and passing the most stringent combined muon ID algorithm
- $|\eta| < 2.5$
- Combined number of pixel hits and crossed dead pixel sensors > 1
- Combined number of SCT hits and crossed dead SCT sensors > 5
- Combined number of pixel holes and SCT holes < 3

- TRT $|\eta|$-dependent quality criteria on combined number of TRT Hits and TRT Outliers
- tracking isolation: the sum p_T of additional tracks in a $\Delta R < 0.3$ cone around the muon is <2.5 GeV
- calorimeter isolation: the sum E_T of additional clusters in a $\Delta R < 0.3$ cone around the muon is < 4 GeV
- does not overlap with a jet to avoid contamination of prompt muons from heavy flavor quark jets
- $p_T > 25$ GeV

Electrons in this analysis pass the following criteria:

- reconstructed and passing the most stringent electron ID algorithm
- $p_T > 25$ GeV
- $|\eta| < 2.47$ and not in the crack region

Taus:

- passing calorimeter-seeded reconstruction and Tau ID, as described in Chapter 5
- $p_T > 25$ GeV
- $|\eta| < 2.3$
- One or three tracks
- Muon veto to reject muons that have deposited sufficient energy in the calorimeter to have been identified as τs
- Medium BDTe electron veto, as described in Sections 6.4 and 6.4.2

Jets in this analysis pass the following criteria:

- reconstructed with `AntiKt4Topo_em` algorithm, as described in Section 4.6
- $p_T > 20$ GeV
- $|\eta| < 2.4$
- Jet Vertex Fraction (JVF) > 0.75; the JVF measures the probability that a jet originated from the hard scatter interaction
- For b-tagged jets, "b-jets", are those with MV1 weight at least 0.601713, as described in Section 4.7

7.3.2 Overlap Removal

ATLAS reconstruction can assign the same energy deposition and set of tracks multiple times as a variety of different physics objects. To ensure that particles in the analysis are uniquely assigned, the following overlap removal procedure is therefore performed on every event. Note that discarded objects cannot form the set of particles that define the $t\bar{t}$ signal selection. The overlap removal procedure is implemented in the following order:

- Track of Electron-Muon overlap: The entire event is discarded if any selected electron shares a common track as the inner track of a muon with $p_T > 15$ GeV, and no isolation criteria is required here.
- Muon-Jet overlap: The muon is discarded if $\Delta R(\mu, jet) < 0.4$.
- Tau-muon overlap: The τ is discarded if $\Delta R(\tau, \mu) < 0.2$.
- Tau-electron overlap: The τ is discarded if $\Delta R(\tau, e) < 0.2$. To calculate the ΔR for this overlap, η^{track} is used.

- Electron-jet overlap: The electron is discarded if $\Delta R(e, jet) < 0.2$,
- Jet-Tau overlap: The jet is discarded if $\Delta R(jet, \tau) < 0.2$.

7.4 Event Selection

The $t\bar{t} \rightarrow \mu + \tau +\ bb\nu\nu$ event selection is as follows:

c0: GRL Event passing Good Runs List (GRL): it is identified as containing good quality data. In Monte Carlo, events are reweighted for pile-up and generator-specific weightings

c1: Trigger Event passes the lowest unprescaled single-muon trigger of p_T >18 GeV

c2: Primary Vertex Event has a primary vertex with at least four tracks

c3: LAr Hole Event must not have physics objects reconstructed in the LAr hole and event must not have a selected electron that shares the same track as that of a low-p_T muon. Overlap removal is performed on objects at this stage.

c4: No Bad Jets Event does not contain any jets of $p_T > 20$ GeV with poor quality criteria

c5: One Muon Event contains exactly one muon with $p_T > 25$ GeV, with that muon passing the trigger

c6: ≥ 2 Jets Event contains at least two jets of good criteria

c7: B-tagging Event contains exactly two jets passing MV1 b-tagging criteria

c8: No Electrons Event contains exactly no electrons of $p_T > 20$ GeV

c9: Tau Event contains at least 1 reconstructed τ candidate

c10: Tight Tau Event contains exactly 1 τ candidate passing "tight" BDTj Tau ID

c11: MET Event has at least 40 GeV of MET

The event selection cutflows are summarized in Table 7.2 for data, Table 7.3 for SM $t\bar{t}$ MC and Table 7.4 for charged Higgs $t\bar{t}$ MC with $m_{H^\pm}$= 130 GeV.

Cut	Event Yield
GRL	2.05441E+08
Trigger	1.66446E+08
Primary Vertex	1.66430E+08
LAr Hole	1.66430E+08
No Bad Jets	1.65532E+08
One Muon	2.18456E+07
$\geq$ 2 Jets	5.95621E+06
B-tagging	1.59114E+06
No Electrons	42431
Tau	7490
Tight Tau	215
MET	148

Table 7.2: The cutflow for the Muon+Tau channel in 4.6 fb^{-1} of 2011 ATLAS data. Note these numbers in the cutflow are numbers of events,; there is no event reweighting for the data.

Note in Chapter 8, two additional requirements on top of set of cuts in this section are imposed for the signal selection: a 1-prong requirement on reconstructed τ candidates and an opposite sign relation between the muon and τ.

Cut	T1 weighted	T1 number of events
GRL	7.92418e+06	1.02393e+07
Trigger	2.26536e+06	2.91433e+06
Primary Vertex	2.26536e+06	2.91432e+06
LAr Hole	2.26536e+06	2.91432e+06
No Bad Jets	2.23649e+06	2.87685e+06
One Muon	1.39558e+06	1.78623e+06
$\geq$ 2 Jets	1.38659e+06	1.77464e+06
B-tagging	1.32928e+06	1.70233e+06
No Electrons	473735	602986
Tau	n.a.	168018
Tight Tau	4315.1	5406
MET	3095.62	3813

Table 7.3: The cutflow for the SM $t\bar{t}$ with ≥ 1 lepton MC Muon+Tau channel. The cutflows are shown with(left) and without(right) MC weightings. The integrated luminosity of the MC sample is about 118 fb^{-1}.

Cut	charged Higgs weighted	charged Higgs number of events
GRL	250027	249999
Trigger	38391.5	38350
Primary Vertex	38391.5	38350
LAr Hole	38391.5	38350
No Bad Jets	37890.3	37844
One Muon	19588.8	19568
$\geq$ 2 Jets	19367.4	19347
B-tagging	17781.5	17766
No Electrons	5090.27	5068
Tau	283.084	1538
Tight Tau	n.a.	282
MET	227.831	227

Table 7.4: The cutflow for the charged Higgs MC Muon+Tau channel. The cutflows are shown with(left) and without(right) MC weightings. The integrated luminosity of the MC sample is dependent on the BR($t \rightarrow H^{\pm}b$) used in the calculation. If BR($t \rightarrow H^{\pm}b$) = 5% is used in the calculation, the resulting $\mathcal{L}$ is about 30 fb^{-1} for this sample.

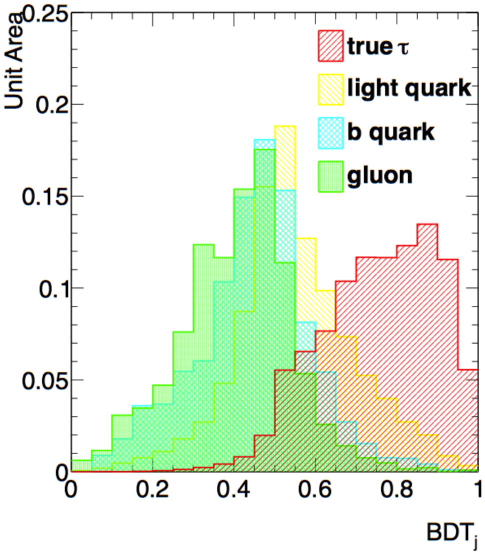

Figure 7.3: The BDTj distributions for truth-level particles reconstructed as τs. The entire $t\bar{t} \rightarrow \mu + \tau + bb\nu\nu$ selection is applied from Section 7.4, except for the MET$>$ 40 GeV cut, which was excluded to increase statistics.

7.5 Systematics

Systematical uncertainties were considered for both the event selection described in this chapter and for the limit setting.

The event selection and detector-related systematic uncertainties on the acceptance of the event selection are the same as described in [15, 16] and are shown in Figure 7.4. The systematic uncertainty on the shape of the templates is also assessed, and described in Section 8.4.

The systematic uncertainties on the acceptance include trigger efficiencies, particle reconstruction and identification efficiencies, and energy and momentum resolution [15, 16]. The final systematic on the charged Higgs simulation signal acceptance is $\{+12\% \; -14\%\}$ and on the SM $t\bar{t}$ simulation signal acceptance is {+13%, -14%}.

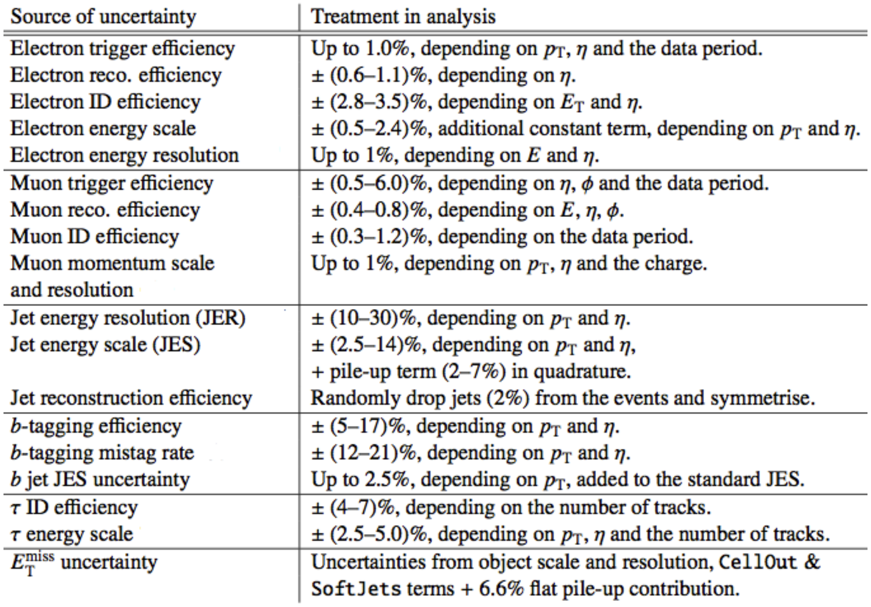

Source of uncertainty	Treatment in analysis
Electron trigger efficiency	Up to 1.0%, depending on p_{T}, η and the data period.
Electron reco. efficiency	± (0.6–1.1)%, depending on η.
Electron ID efficiency	± (2.8–3.5)%, depending on E_{T} and η.
Electron energy scale	± (0.5–2.4)%, additional constant term, depending on p_{T} and η.
Electron energy resolution	Up to 1%, depending on E and η.
Muon trigger efficiency	± (0.5–6.0)%, depending on η, ϕ and the data period.
Muon reco. efficiency	± (0.4–0.8)%, depending on E, η, ϕ.
Muon ID efficiency	± (0.3–1.2)%, depending on the data period.
Muon momentum scale and resolution	Up to 1%, depending on p_{T}, η and the charge.
Jet energy resolution (JER)	± (10–30)%, depending on p_{T} and η.
Jet energy scale (JES)	± (2.5–14)%, depending on p_{T} and η, + pile-up term (2–7%) in quadrature.
Jet reconstruction efficiency	Randomly drop jets (2%) from the events and symmetrise.
b-tagging efficiency	± (5–17)%, depending on p_{T} and η.
b-tagging mistag rate	± (12–21)%, depending on p_{T} and η.
b jet JES uncertainty	Up to 2.5%, depending on p_{T}, added to the standard JES.
τ ID efficiency	± (4–7)%, depending on the number of tracks.
τ energy scale	± (2.5–5.0)%, depending on p_{T}, η and the number of tracks.
$E_{\mathrm{T}}^{\mathrm{miss}}$ uncertainty	Uncertainties from object scale and resolution, `CellOut` & `SoftJets` terms + 6.6% flat pile-up contribution.

Figure 7.4: The main systematic uncertainties that impact the acceptance [15, 16].

Chapter 8

Charged Higgs Limit Setting

This chapter summarizes the limit setting procedure. Section 8.1 describes the potential of the technique. Sections 8.2,8.3 and 8.4 describe the construction of both signal and background templates. The actual signal extraction is done with a log likelihood fit; this is described in Section 8.5.

8.1 Generator-Level Υ Distributions

Generator-level distributions of the charged asymmetry τ polarization observable are shown for samples of left-handed and right-handed 1-prong τs, from the $t\bar{t} \to WWbb \to \tau_L + \mu\ + bb\nu\nu$ and $t\bar{t} \to WH^{\pm}bb \to \tau_R + \mu\ + bb\nu\nu$ processes, respectively. These samples are described in Table 7.1 and are also used to optimize the event selection.

The effect of ATLAS reconstruction on the Υ distribution for τs from the charged Higgs sample is shown in Figure 8.2. Note the generator-level peak at $\Upsilon = 1.0$ for the case of $\tau \to \pi^{\pm}\nu$ smears out after the object undergoes detector simulation and τ reconstruction.

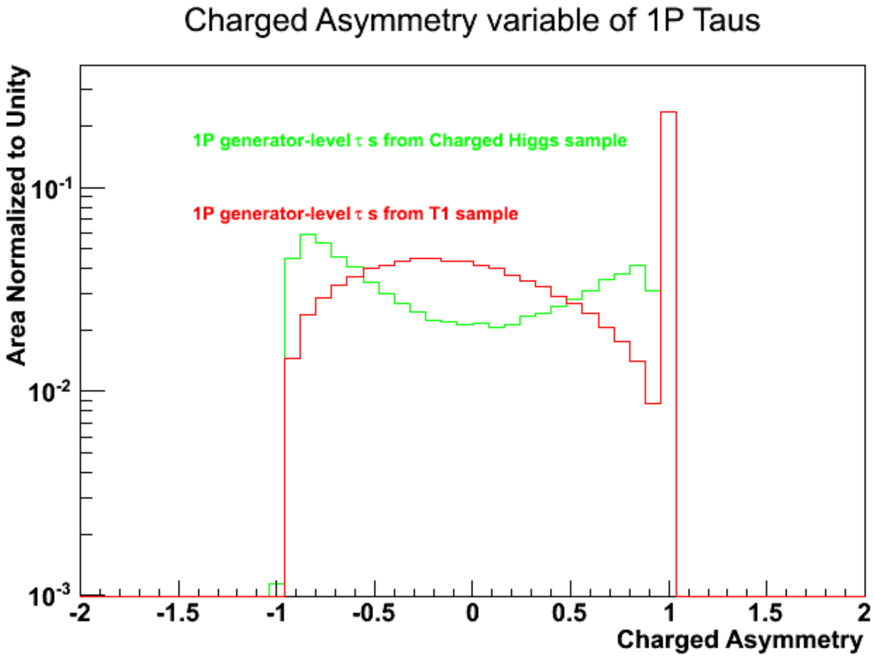

Figure 8.1: Generator-level 1-prong τ_{had}s from t $\rightarrow H^{\pm}b$, in green, and SM t$\rightarrow Wb$, in red, MC samples. No event selection has been imposed on these samples of τs.

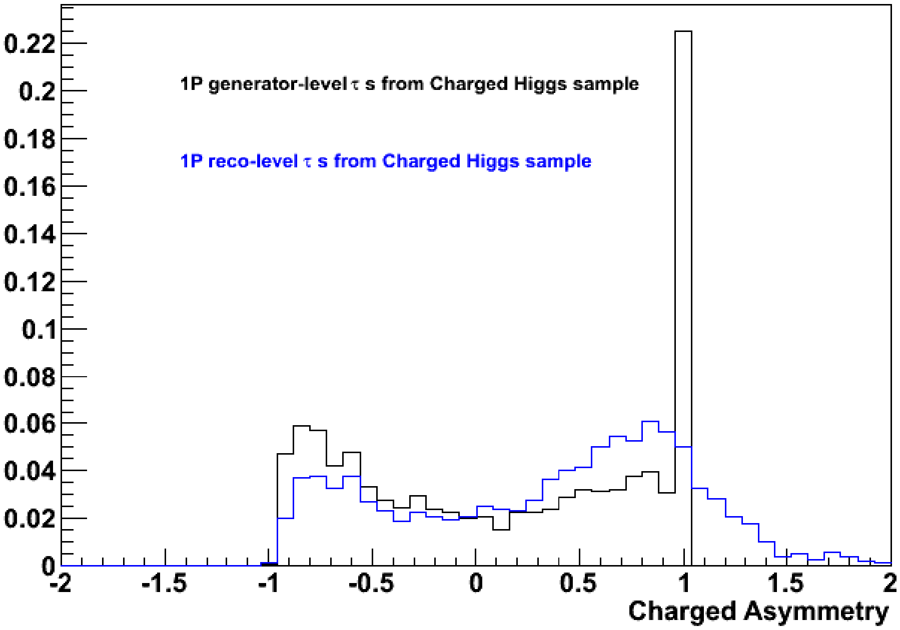

Figure 8.2: The normalized generator-level Υ distribution, in black, of 1-prong τ_{had}s from $H^{\pm} \rightarrow \tau\nu$. The distribution of the same τs at reconstruction-level is shown in blue.

8.2 Signal and $t\bar{t}$ Background Υ Modeling

To obtain the signal $t\bar{t} \to WH^{\pm}bb \to \tau_R + \mu \; + bb\nu\nu$ and SM $t\bar{t}$ background Υ shape templates, the event selection prescription is followed as in Section 7.4. In addition to the event selection, a 1-prong requirement is imposed on reconstructed τ_{had} candidates. The reconstructed muon and reconstructed τ_{had} candidate are also required to have opposite signed electric charge. Figure 8.3 shows the normalized templates, highlighting the shape difference.

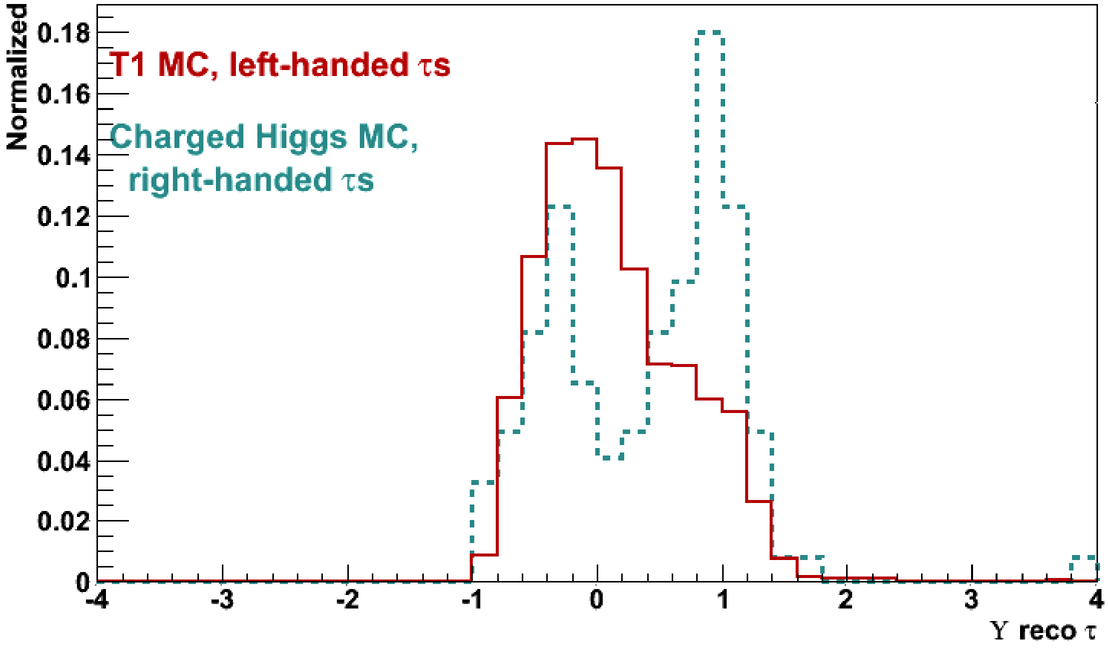

Figure 8.3: The normalized Υ distributions after full event selection for reconstructed 1-prong τ candidates. These two distributions serve as two templates for the fit described in Section 8.5. In dotted blue is the signal template of τs from charged Higgs simulation of $t\bar{t} \to \tau + \mu + \; bb\nu\nu$ event, where the τ originates from a $H^{\pm} \to \tau\nu$ decay. In red is the background template of τs from SM $t\bar{t} \to \tau + \mu + \; bb\nu\nu$ simulation. Note the reconstructed τ candidates in these templates are within events with a generator-level 1-prong τ_{had}.

8.3 Data-Driven QCD Estimate

In this analysis there is a substantial W+jet background component where a jet in the event is misidentified as a τ. After $t\bar{t} \to WWbb \to \tau + \mu + \ bb\nu\nu$, the next largest background is events in which a jet is reconstructed as a τ candidate. The background Υ shape and contribution from misidentified jets cannot be reliably modeled in the simulation and is therefore measured in data. This section describes the "jets-faking-taus" template.

8.3.1 W+Jets

The "W+jets" events that pass the charged Higgs $t\bar{t}$ signal selection, described in Section 7.4, can come from processes like the diagrams shown in Figure 8.5. The muon comes from the W decay and the three jets provide the fake τ and two fake b-tagged jets. Another selection is developed to select W+jets events in order to obtain the Υ template jets that fake τs.

The similarity of jets in both samples allows for a targeted understanding of the principal backgrounds. The same data-taking period and data quality requirements are used as in Section 7.4. Additionally, the same muon trigger is used for obtaining jets from W+jets events, with W $\to \mu\nu$, as is used for the event selection in Chapter 7. The nominal selection is given in Table 8.1 and the resulting Υ distribution is shown in Figure 8.6.

Note the final cut in the nominal W+jets selection, MET $>$ 40 GeV, is applied to reduce the Z$\to \tau\tau$ and multijet contributions. Finally, where indicated, a Tau ID cut is also applied to obtain the final selection. The results of additional studies on the Υ behavior of jets are shown in the Appendix.

Cut	Description
c1	Event passes GRL and the lowest unprescaled single-muon trigger of $p_T^{trigger}$ >18 GeV
c2	Event has a primary vertex with at least four tracks
c3	Event is not in the LAr hole and event does not have an electron sharing the same track as that of a low-p_T muon
c4	Event does not contain any jets of p_T > 20 GeV with poor quality criteria
c5	Event has exactly 1 muon with p_T >25 GeV and no additional muons with p_T >15 GeV
c6	Event has MET > 40 GeV

Table 8.1: The nominal selection for the W+jets selection in 2011 ATLAS data. Any additional cuts applied on top of the nominal selection for investigations documented in this chapter and the Appendix, such as number of b-tagged jets in the event and Tau ID, are noted where appropriate. Because the $t\bar{t}$ cross section is far smaller than that of jet production, the amount of $t\bar{t}$ contamination in this sample is small.

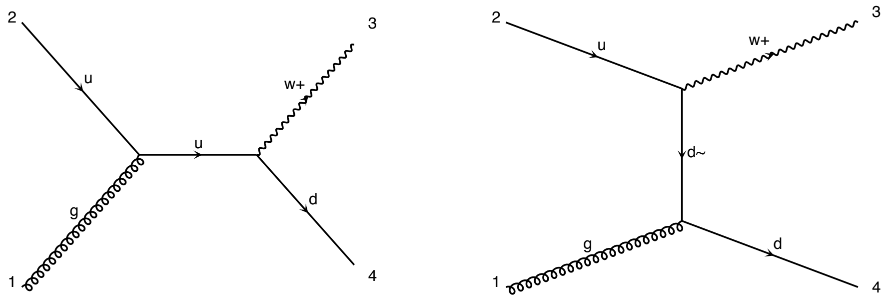

Figure 8.4: Leading W+1 jet diagrams. The charge of the outgoing quark is opposite to the charge of the lepton resulting from a W→ $l\nu$ decay. This is the dominant contribution to events in the jets-faking-taus template with the W+jets selection in Table 8.1 [6].

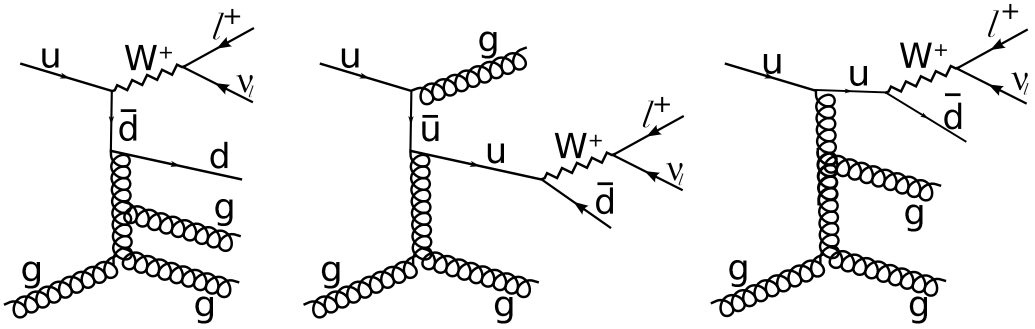

Figure 8.5: Leading W+3jet diagrams [6]. These are the dominant processes in the charged Higgs signal selection described in Section 7.4. Note that the diagram on the left produces a quark with opposite sign from the W boson and the charged lepton [6].

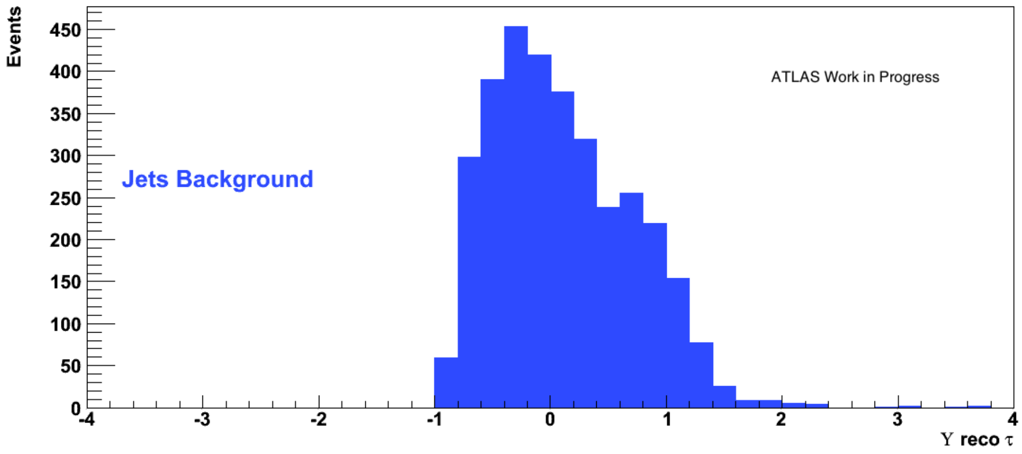

Figure 8.6: The data-driven jets-faking-taus ϒ template, which comes from reconstructed 1-prong τ candidates passing the W+jets selection in Table 8.1 as well as tight BDT Tau ID.

8.3.2 ABCD method

The normalization of the jets-faking-taus ϒ template is obtained with an "ABCD" method. The method takes advantage of two uncorrelated variables to estimate the background level by extrapolating from background-dominated regions. Note that only for the context of this section, "signal" refers to the SM production of τs within

$t\bar{t}$ decays.

In addition to the signal-dominated region defined by the signal selection in the data, three background-dominated control regions are defined by inverting one or two requirements, as described below and shown in Figure 8.7.

Events are divided into four categories after passing all cuts from Section 7.4, modulo the Tau ID and MET cuts, which are used to partition the ABCD regions:

- Region A (mostly signal): Events with a reconstructed τ candidate passing tight Tau ID and MET $>$ 40 GeV
- Region B (control; signal+background): Events with a reconstructed τ candidate passing loose & failing medium Tau ID and MET>40 GeV
- Region C (control; signal+background): Events with a reconstructed τ candidate passing tight Tau ID and MET<30 GeV
- Region D (control; mostly background): Events with a reconstructed τ candidate passing loose & failing medium Tau ID and MET<30 GeV

The results are shown in Tables 8.2 and 8.9.

If the assumption is taken that the likelihood of a jet passing a particular level of Tau ID and the MET per event are uncorrelated, and the contributions of signal and EW background events in the control regions B,C,D are negligible, the following relation in the data holds [48]:

$$\frac{N^A}{N^D} = \frac{N^B}{N^D} \cdot \frac{N^C}{N^D} \ , \tag{8.1}$$

where N_A is shorthand for the amount of background in region A, and not the total number of events in A. We take $N^A \equiv N_{background\ in\ A}$. The backgrounds are assumed to be jets. However, the assumption that the control regions are completely background-dominated can be refined. To quantify the signal level in the four regions of the ABCD grid, the coefficients for the ratios of simulated signal ($t\bar{t}$) events are defined:

$$c_i \equiv \frac{N^i_{sig} + N^i_{EW}}{N^A_{sig} + N^A_{EW}} \ , \tag{8.2}$$

where $i \in \{A, B, C, D\}$. With these coefficients, we can define corrected values for the calculation in equation 8.1 by replacing $N^i \rightarrow N^i_{corrected}$, where we take

$$N^i_{QCD} = N^i - c_i(N^A - N^A_{QCD}). \tag{8.3}$$

In this context N_{QCD} refers to non-$t\bar{t}$ jet backgrounds. The N^i comes from data and we solve for N^A_{BG}, where each of the quantities comes from the data and has a component of N^A_{BG}:

$$N^A_{BG} = \frac{N^B_{corrected} \cdot N^B_{corrected}}{N^D_{corrected}} \tag{8.4}$$

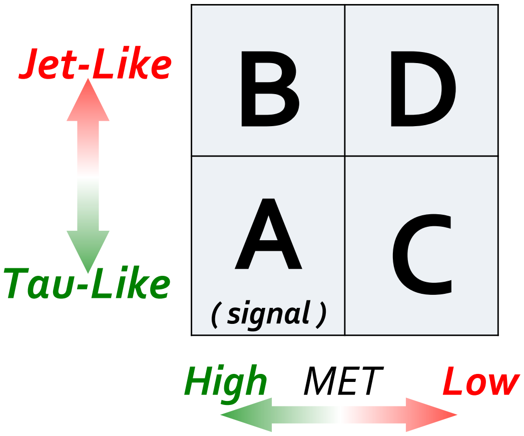

Figure 8.7: The four ABCD regions. Region A is dominated by signal.

124	54
B	D
A	C
148	41

Table 8.2: From 4.6 fb^{-1} of 2011 $\sqrt{s}$=7 TeV data, the numbers of events for the $\mu+\tau$ ABCD matrix passing the selection, before requirements on Tau ID and MET.

69	32
B	D
A	C
89	29

Table 8.3: From 4.6 fb^{-1} of 2011 $\sqrt{s}$=7 TeV data, the numbers of events for the $\mu+\tau$ ABCD matrix. The same cuts as in the previous ABCD Table 8.2 with an additional single prong requirement on the τ candidate, are applied to each of the four ABCD regions.

64	26
B	D
A	C
87	25

Table 8.4: From 4.6 fb^{-1} of 2011 $\sqrt{s}$=7 TeV data, the numbers of events for the $\mu+\tau$ ABCD matrix. The same cuts as in the previous ABCD Table 8.3 with an additional opposite sign charge requirement between the τ candidate and muon, are applied to each of the four ABCD regions. Applying the OS requirement results in Region D having the largest decrease in events, as expected.

3885	1140
B	D
A	C
3813	975

Table 8.5: From SM $t\bar{t}$ MC, the numbers of $t\bar{t} \rightarrow \mu + \tau\ + bb\nu\nu$ events in the ABCD matrix passing the selection, before requirements on Tau ID and MET.

2491	676
B	D
A	C
2576	624

Table 8.6: From the SM $t\bar{t}$ MC sample, the numbers of $t\bar{t} \to \mu + \tau_{had} + bb\nu\nu$ events in the ABCD matrix. The same cuts as in the previous ABCD Table 8.5 with an additional single prong requirement on the tau candidate, are applied to each of the four ABCD regions.

2174	587
B	D
A	C
2467	583

Table 8.7: From the SM $t\bar{t}$ MC sample, the numbers of $t\bar{t} \to \mu + \tau_{had} + bb\nu\nu$ events in the ABCD matrix. The same cuts as in the previous ABCD Table 8.6 with an additional opposite sign charge requirement between the τ candidate and muon, are applied to each of the four ABCD regions.

739	141
B	D
A	C
1782	353

Table 8.8: From the SM $t\bar{t}$ MC sample, the numbers of $t\bar{t} \to \mu + \tau_{had} + bb\nu\nu$ events in the ABCD matrix, where events contain a hadronically-decaying τ at truth-level. Note that this T1 ABCD matrix will be used for further analysis.

c_i	$\frac{N^i}{N^A}$
c_A	1.0, by definition
c_B	$\frac{N^B}{N^A} = 739/1782 = 0.41$
c_C	$\frac{N^C}{N^A} = 353/1782 = 0.197$
c_D	$\frac{N^D}{N^A} = 141/1782 = 0.07$

Table 8.9: The coefficients based on the ABCD matrix of the SM $t\bar{t}$ MC sample, calculated from ABCD Table 8.8.

$i \in \{A, B, C, D\}$	A	B	C	D
N^i (Data)	87	64	25	26
N^i_{signal} ($t\bar{t}$ MC)	1782	739	353	141
c_i, calculated	1.0	0.41	0.197	0.07
N^i_{QCD}, calculated	20.2	36.6	11.8	21.3

Table 8.10: Estimated sample compositions and c_i factors, extracted from Table 8.4 and Table 8.8. N^A_{QCD} is calculated from Equation 8.4. Once N^A_{QCD} is calculated, N^B_{QCD}, N^C_{QCD} and N^D_{QCD} are calculated from Equation 8.3.

The samples listed in Table 8.11 are used to determine the electroweak signal contamination in the ABCD matrix. After truth-matching and the full event selection, 0 events remain for all samples.

Process	Number of Events	σ [pb]	k-factor	Integrated Luminosity
$Z \rightarrow \tau\tau$ + 1 jet	3261047	133.94	1.25	19.47 fb^{-1}
$Z \rightarrow \tau\tau$ + 2 jets	998960	40.295	1.25	19.83 fb^{-1}
$Z \rightarrow \tau\tau$ + 3 jets	495950	11.029	1.25	35.97 fb^{-1}
$W \rightarrow \mu\nu$ + 2 jets	2910420	376.08	1.19	6.50 fb^{-1}
$W \rightarrow \mu\nu$ + 3 jets	776101	100.72	1.19	6.475 fb^{-1}
$W \rightarrow \mu\nu$ + 4 jets	192293	25.99	1.19	6.21 fb^{-1}

Table 8.11: The samples' integrated luminosities are calculated as $\mathcal{L} = \frac{N}{\sigma \cdot k-factor}$ [2].

8.4 Systematics on the Method

The systematic uncertainty on the shape of the MC templates is also examined, in addition to systematic uncertainties on the acceptance as described in Section 7.5. The largest uncertainty on the template shape is due to the Tau Energy Scale(TES). A variation in TES systematically impacts the observable, as Υ is inversely correlated to the visible τ E_T measured in the ATLAS calorimeters. The TES is varied by ±3.5% to match the uncertainty in the quantity and the resulting shape difference, for the same set of τs, is shown in Figure 8.8.

In the actual treatment of TES, both the shape and acceptance change. This is illustrated in Figures 8.9 and 8.10.

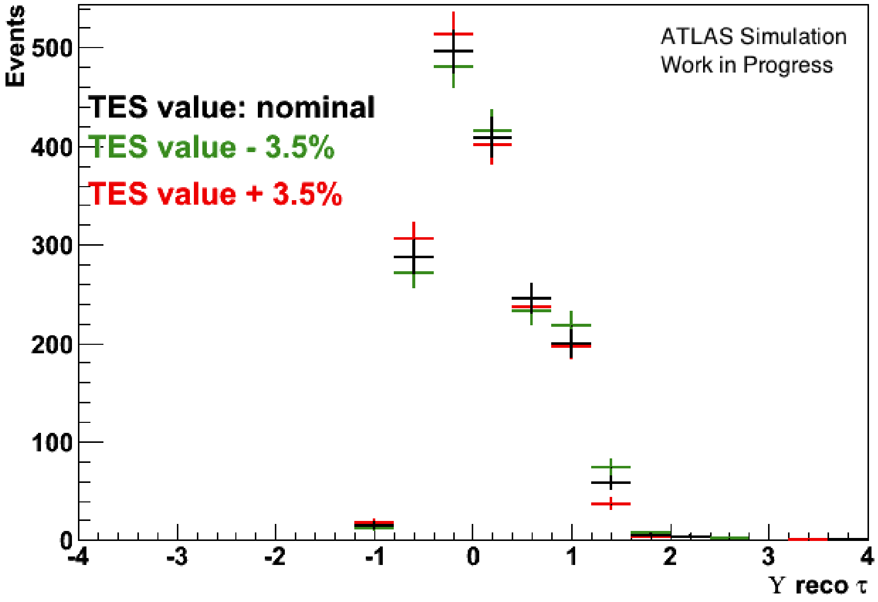

Figure 8.8: The resulting shape difference of the Υ observable as a result of the variation on the TES of ±3.5% in the SM $t\bar{t} \rightarrow \mu + \tau + \ bb\nu\nu$ MC sample, using the same set of events. Υ is inversely correlated with calorimeter-based E_T, thus a 3.5% enhancement in the TES (in red) shifts the distribution slightly lower than the nominal while a 3.5% decrease in the TES (in green) shifts the distribution slightly higher than the nominal distribution(in black).

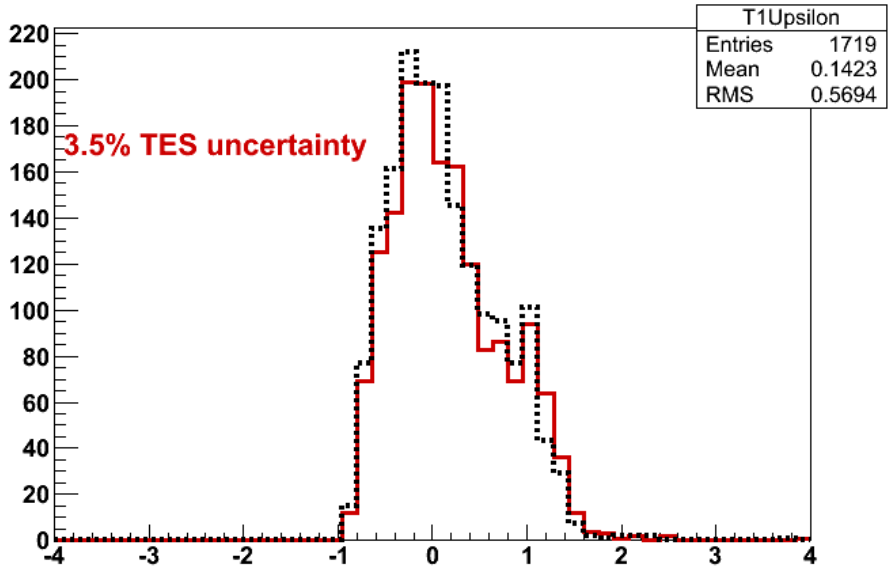

Figure 8.9: The resulting shape and event yield differences of the Υ observable as a result of the variation on the TES of 3.5% in the $t\bar{t} \rightarrow \mu + \tau + \ bb\nu\nu$ MC sample. Both the τ p_T threshold and the Υ distribution are modified as a result of the TES variation.

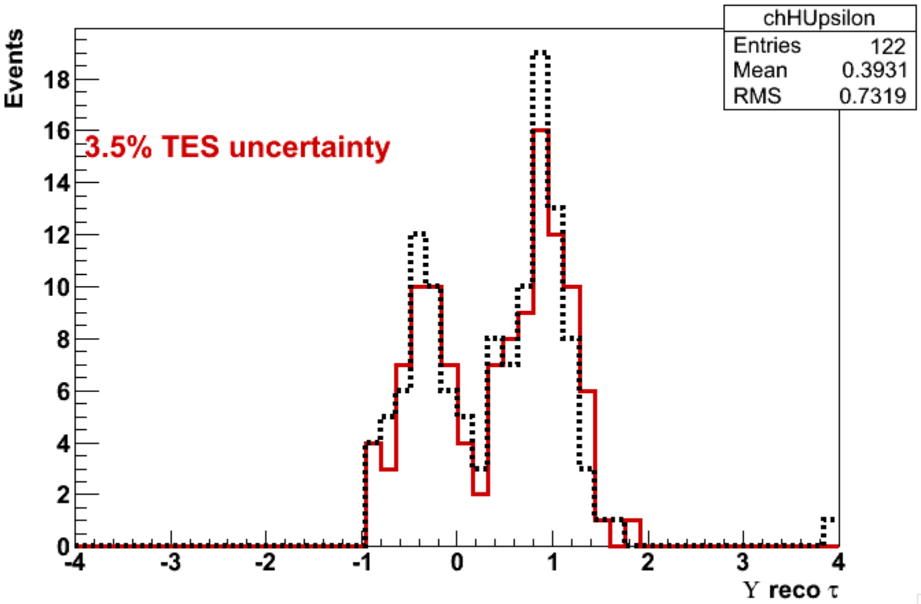

Figure 8.10: The resulting shape and event yield differences of the Υ observable as a result of the variation on the TES of 3.5% in the charged Higgs MC sample. Both the τ p_T threshold and the Υ distribution are modified as a result of the TES variation.

The modified Υ templates from Figures 8.9 and 8.10 are included in the limit setting uncertainties.

8.5 Limit Setting with Templates

After constructing the signal (τs from $t\bar{t} \rightarrow H^{\pm}Wbb$) and background ($\tau$s from SM $t\bar{t}$ and jets-faking-taus) shapes, the normalization for each component template must be determined. This is done by maximizing the extended likelihood function [49]. The extended likelihood function is derived from the classical likelihood.

If a random generation of a single number x from a distribution f has a likelihood proportional to $f(x)$, then the classical likelihood $\mathcal{L}_{classical}$ for a sample with multiple points is the product of the function evaluated at every point in the ensemble.

The *extended* likelihood, $\mathcal{L}$ is defined as

$$\mathcal{L} = \tfrac{e^{-\nu}\nu^{N}}{N!}\ \mathcal{L}_{classical}$$

where N is the total size of the sample and ν is the expected number of events. The fitted yields are identical in both classical and extended likelihood formalisms but the errors on the yields differ. A discussion of the difference between the result obtained from maximizing $\mathcal{L}_{classical}$ and $\mathcal{L}$ is [50].

8.5.1 Likelihood

Given the templates above and the normalization of N_{QCD} a trial function, $f(\Upsilon)$, can be constructed as:

$$f(\Upsilon) = N_{signal} f_{signal}(\Upsilon)\ +\ N_{SMttbar} f_{SMttbar}(\Upsilon) + N_{QCD} f_{QCD}(\Upsilon),$$

where the discriminating variable is Υ,

$f_{signal}(\Upsilon)$ is the charged Higgs MC template,

$f_{SMttbar}(\Upsilon)$ is the SM $t\bar{t}$ MC background template,

and $f_{QCD}(\Upsilon)$ is the data-driven jets-faking-taus background template.

N_{QCD} is a fixed value, since the jets-faking-taus level is not allowed to float. However the other two values, $N_{signal}, N_{SMttbar}$, are floating and will be determined from the fit. These values, which are the global fit parameters, are the values that maximize the Likelihood function; in other words they are set to be the certain combination of signal and background template best describing the data shape $f_{Data}(\Upsilon)$, which has 87 total events.

The likelihood function is constructed to be the product over each bin:

$$\mathcal{L} = \prod_{i=0}^{49} f(\Upsilon_i) = \prod_{i=0}^{49} (N_{signal} f_{signal}(\Upsilon_i) \ + \ N_{SMttbar} f_{SMttbar}(\Upsilon_i) \ + \ N_{QCD} f_{QCD}(\Upsilon_i))$$

In an unbinned fit, the template fitting algorithm has access to each of the 87 Υ values in f(Υ). In an binned fit, the template fitting algorithm only has access to a histogram given the overall shape and normalization of f(Υ). In this analysis, an binned fit is performed.

The likelihood provided above is single-dimensional and mostly pedagogical. It does not exactly describe this analysis, which does a multidimensional fit. A multidimensional likelihood, built with more variables, must be constructed to incorporate the nuisance parameters as well [51]. To do this, new notation is introduced.

It is common to introduce a continuous signal strength parameter, μ, which can be thought of as the ratio of observed to expected signal events. A value of $\mu = 0$ corresponds to the background-only hypothesis, in other words that there is no room for the charged Higgs template in the distribution. A value of $\mu = 1$ corresponds to the nominal signal+background hypothesis. Therefore the coefficient μS corresponds to N_{signal}, while B is analogous to some combination of $N_{SMttbar}$ *and* N_{QCD}. Equivalent to the likelihood, $\mathcal{L}$, $\mathcal{P}(n_b|\mu)$ is the probability of 87 events given a value of μ. It can be written as the product of the Poisson probability of getting n_i events in bin i given the signal and background values in bin i:

$$\mathcal{L} \equiv \mathcal{P}(n_b|\mu) = \mathrm{Pois}(n_1|\mu S_1 + B_1)\mathrm{Pois}(n_2|\mu S_2 + B_2)...\mathrm{Pois}(n_{87}|\mu S_{87} + B_{87})$$

$$= \mathcal{N}_{com} \prod_{i \in bins} Pois(n_i | \mu \nu_i^{signal}(\vec{\alpha}) + \nu_i^{bkg}(\vec{\alpha})\ )$$

where $\mathcal{N}_{com}$ is a constant combinatorial factor that can be neglected. The per-bin terms $\nu_i^{signal}(\vec{\alpha})$ and $\nu_i^{bkg}(\vec{\alpha})$ are functions of the nuisance parameters $\vec{\alpha} = \{\alpha_1, \alpha_2 ...\}$. The signal and background histograms, the νs, relate to the shape templates bin-by-bin:

$$\nu_i^{signal}(\vec{\alpha}) = \omega S f_S(\Upsilon_i), \text{ where S stands for signal}$$

$$\nu_i^{bkg}(\vec{\alpha}) = \omega \dot{B} f_B(\Upsilon_i), \text{ where B stands for the jets-faking-taus and SM } t\bar{t} \text{ backgrounds,}$$

where i is the index of the bin containing Υ_i and ω is the unit width of each bin. Since the templates $f(x)$ are normalized, the values of S and B are

$$S = \Sigma_i \nu_i^{signal}\ ,\ B = \Sigma_i \nu_i^{bkg}$$

A marked Poisson model can be computed for $\mathcal{P}(n_b|\mu)$ by including the Poisson probability for obtaining 87 events when μS+B events are expected in total [52]. Additionally, the probability density of obtaining Υ_i based on the relative mixture of $f_S(\Upsilon)$ and $f_B(\Upsilon_i)$ for a given μ is incorporated to give the final form for $\mathcal{P}(n_b|\mu)$:

$$\mathcal{L} \equiv \mathcal{P}(n_b|\mu) = Pois(87|\mu S + B) \cdot \prod_{i \in bins} \frac{\mu \nu_i^{signal} + \nu_i^{bkg}}{\mu S + B}$$

Finally, a global multidimensional maximization is done on the likelihood with respect to the global fit parameters, $N_{signal}\ and\ \vec{\alpha}$:

$$\frac{\partial \mathcal{L}}{\partial N_{signal}} = \frac{\partial \mathcal{L}}{\partial \vec{\alpha}} = 0$$

This maximization is done in multidimensional parameter space for $N_{signal}, \vec{\alpha}$. Note that $N_{SMttbar}$ is not a free parameter but rather constrained to N_{signal} by the relation $BR(t \to Wb) + BR(t \to H^{\pm}b) = 1$. Roughly speaking, the fit attempts, though does not guarantee, to meet the condition of $N_{signal} + N_{SMttbar} = 87 - N_{QCD}$.

Equivalently speaking, the extremization can also be done with respect to the fit parameter, μ by $\frac{\partial \mathcal{P}(n_b|\mu)}{\partial \mu}=0$.

The likelihood extremization calculates the most likely value of the likelihood as a percentage, which can be related to the most likely value of N_{signal}:

$$\frac{BR(t \to H^{\pm}b)}{BR(t \to H^{\pm}b)+BR(t \to Wb)}$$

In this analysis HistFactory is used to perform the fit [53]. It is a tool developed by ATLAS colleagues and it interfaces with statistical packages used in High Energy Physics [52]. The core functionality of HistFactory is to build the likelihood function given the templates and the data sample; the actual extremization is carried out with the MINUIT program from within the tool.

8.5.2 Experimental Uncertainties

The following uncertainties, and nuisance parameters associated with the systematics in the analysis, are incorporated into the likelihood template fitting:

- Statistical uncertainty of 5% on each bin in the jets-faking-taus template to represent the available statistics in the distribution that produced the template shape.

- Systematic uncertainty on the level of jets-faking-taus template, from ABCD method. The uncertainty is $-32\%, +92\%$, and comes from propagating the statistical uncertainty in region D of Table 8.4. The nuisance parameter associated to this is α_{QCD}.

- Systematic uncertainty on the acceptance of SM $t\bar{t} \to \tau + \mu$ sample. The uncertainty is $\{+13\%, -14\%\}$, and comes from the systematics in Table 7.4 [15], [16]. The nuisance parameter associated with this is $\alpha_{SMttbar}$.

- Systematic uncertainty on the acceptance of $t\bar{t} \to WH^{\pm}bb \to \tau + \mu$ sample. The uncertainty is $\{-14\%, +12\%\}$, and comes from the systematics in Table 7.4 [15], [16]. The nuisance parameter associated with this is α_{chH}.
- Systematic uncertainty on the luminosity delivered to ATLAS by the LHC, ± 3.9%.

8.5.3 Result of the Fit

The result of the likelihood extremization with the templates and associated uncertainties is shown in Figure 8.11.

Figure 8.11 includes all of the uncertainties described in Section 8.5.2. However, the TES systematic described in Section 8.4 is evaluated separately.

TES systematic is evaluated by performing the fit a second time using the TES-varied templates shown in Section 8.4. It is input separately and results in a fit difference of 0.4% from Figure 8.11. Adding in quadrature with the uncertainty calculated by the fit, gives a total uncertainty of :

$$\sqrt{6.7^2 \ + \ 0.4^2} \approx 6.7.$$

Thus the largest systematic on the method, the TES, is a small effect. This is an expected conclusion, given the stability of the templates in Figures 8.9 and 8.10 under the TES variation.

8.6 Resulting Templates

In Sections 8.2 and 8.3, the signal and two background templates are derived. They are presented in Figures 8.3 and 8.6. The resulting extremization of the likelihood, Figure 8.11, provides the preferred relative normalizations.

In Figure 8.12 the purely SM scenario templates, with no charged Higgs template contribution, are overlaid with data.

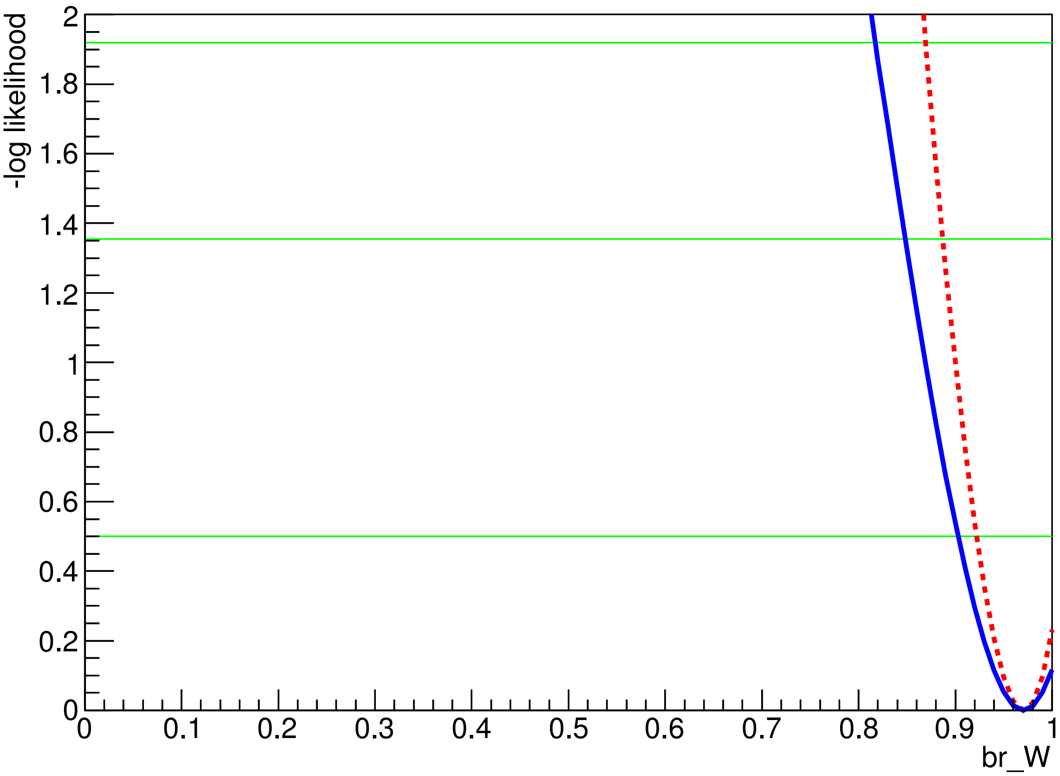

Figure 8.11: The result of the fit from HistFactory using the likelihood extremization. The horizontal green lines show roughly the 1, 2, and 3σ values. The red dotted curve shows the $-log(\mathcal{L})$ curve after including only statistical errors, whereas the blue curve is after the inclusion of both statistical and systematic errors. The $-log(\mathcal{L})$ is minimized at BR(t→ Wb)= 97.2% with a symmetric errors of $\pm 1\sigma = 6.7\%$ and asymmetric MINOS errors of $\{-7.0,\ \textit{at limit}\}$. The charged Higgs contribution is consistent with 0. At the 2σ line, the value of the blue curve is at BR(t→ Wb)=84.0%. Thus at the 95% confidence level, this analysis places a limit of BR(t→ $H^{\pm}b$) $<$ 16 %.

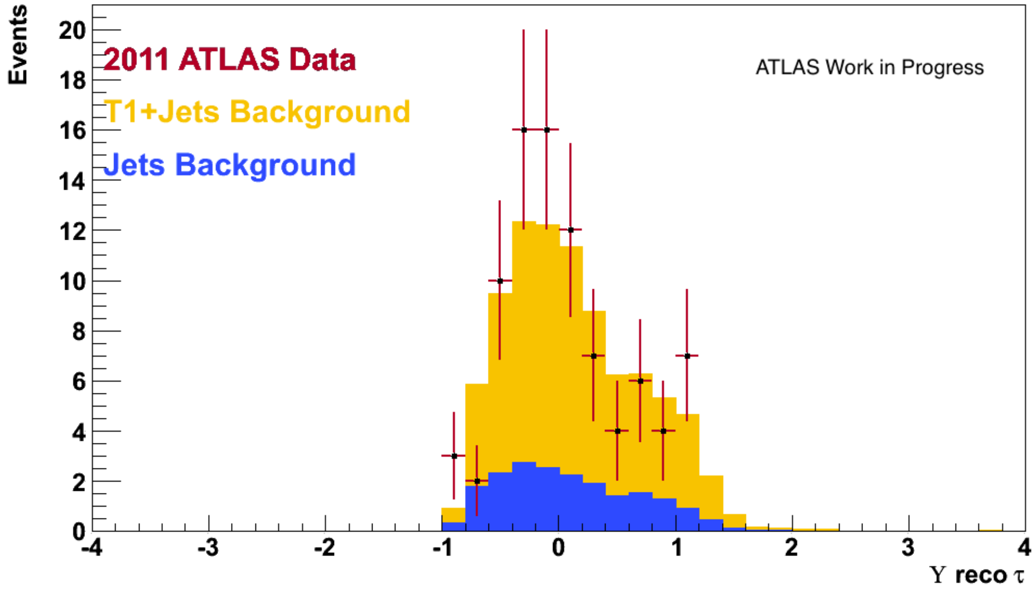

Figure 8.12: The data-driven jets-faking-taus and the stacked SM $t\bar{t}$ background templates are shown, along with 2011 ATLAS Data. The normalization in this figure assumes a purely SM scenario of BR$(t \to Wb) = 100\%$. The data is consistent with a purely SM $t\bar{t}$ scenario.

The Appendix Section A.3 shows Υ distributions with a preferred value of charged Higgs content obtained by the likelihood extremization.

Chapter 9

Conclusions

A charged Higgs boson search has been performed in $t\bar{t}$ events in the decay mode $t \to H^{\pm}b$ assuming BR($H^{\pm} \to \tau\nu$) = 100%. A total of 4.6 fb^{-1} of $\sqrt{s} = 7$ TeV proton-proton collision data at the LHC was recorded in 2011 with the ATLAS detector and used for this purpose.

The results are shown in Figure 8.11 and Figure A.8. At the 95% confidence level, this analysis places the constraint:

$$\mathrm{BR}(\mathrm{t} \to H^{\pm}_{130GeV}\ b \quad \to \quad \tau\nu\ b) < \ 16\%$$

Chapter 6 described the development and implementation of a powerful multivariate discriminant for electron rejection in Tau ID. Chapters 7 and 8 detailed the method of obtaining templates for signal and SM background process of τ_{Right} and τ_{Left}, respectively. In addition, a detailed explanation of obtaining the jets-faking-taus background template was given.

As an independent technique to the more standard cut-and-count procedures, this thesis explored τ polarimetry as a discriminating technique for the first time in a charged Higgs search. Along with a cut-and-count procedure, this new technique can improve searches for physics beyond the SM. The technique presented in this thesis will serve as a guide for future analyses at hadron colliders.

Bibliography

[1] Halzen and Martin. *Quarks and Leptons: An Introductory Course in Modern Particle Physics*. John Wiley and Sons, Inc., 1984.

[2] J Beringer et al. Particle Data Group. *Phys. Rev.*, D86:010001, 2012.

[3] David Griffiths. *Introduction to Elementary Particles*. John Wiley and Sons, Inc., 2nd edition, 2008.

[4] Abdelhak Djouadi. The Anatomy of ElectroWeak Symmetry Breaking II. The Higgs Bosons in the Minimal Supersymmetric Model. *Phys. Rept.*, 459:1–241, 2008.

[5] S. Heinemeyer, O. Stal, and G. Weiglein. Interpreting the LHC Higgs Search Results in the MSSM. *Phys. Lett. B*, 710:201–206, 2012.

[6] Johan Alwall, Michel Herquet, Tim Stelzer, et al. MadGraph 5 : Going Beyond. *JHEP*, 1106:128, 2011.

[7] The ATLAS Collaboration. Measurement of Tau Polarization in $W \to \tau\nu$ Decays with the ATLAS Detector in pp Collisions at $\sqrt{s} = 7$ TeV. Technical Report ATLAS-CONF-2012-009, CERN, Geneva, Mar 2012.

[8] R Bailey and P Collier. Standard Filling Schemes for Various LHC Operation Modes. Technical Report LHC-PROJECT-NOTE-323, CERN, Geneva, Sep 2003.

[9] `https://twiki.cern.ch/twiki/bin/view/AtlasPublic`.

[10] `http://www.atlas.ch`.

[11] Matteo Cacciari, Gavin Salam, and Gregory Soyez. The Anti-kt Jet Clustering Algorithm. *Journal of High Energy Physics*, (04):63, 2008.

[12] The ATLAS Collaboration. Performance of the Reconstruction and Identification of Hadronic Tau Decays with ATLAS. Technical Report ATLAS-CONF-2011-152, CERN, Nov 2011.

[13] The ATLAS Collaboration. Measurement of the Misidentification Probability of Tau Leptons from Hadronic Jets and from Electrons. Technical Report ATLAS-CONF-2011-113, CERN, Geneva, Aug 2011.

[14] The ATLAS Collaboration. Performance of the Reconstruction and Identification of Hadronic Tau Decays in ATLAS with 2011 Data. Technical Report ATLAS-CONF-2012-142, CERN, Geneva, Oct 2012.

[15] S Behar, C Buszello, P Czodrowski, A Ferrari, M Flechl, et al. Search for a charged Higgs boson decaying via $H^{\pm} \to$ tau(had) nu+lepton in ttbar events using 4.6 fb^{-1} of pp collision data recorded at $\sqrt{s} = 7$ TeV with the ATLAS detector — Supporting note. Technical Report ATL-COM-PHYS-2012-083, CERN, Geneva, Jan 2012. Supporting note of HIGG-2012-09.

[16] S Behar, C Buszello, P Czodrowski, A Ferrari, M Flechl, et al. Search for a charged Higgs boson decaying via $H^{\pm} \to$ tau(had) nu+lepton in ttbar events using 4.6 fb^{-1} of pp collision data recorded at $\sqrt{s} = 7$ TeV with the ATLAS detector – Supporting note. Technical Report ATL-PHYS-INT-2012-046, CERN, Geneva, 2012.

[17] Donald H. Perkins. *Introduction to High Energy Physics*. Cambridge University Press, 4th edition, 2000.

[18] Neil D. Christensen, Tao Han, and Tong Li. Pair Production of MSSM Higgs Bosons in the Non-decoupling Region at the LHC. 2012.

[19] Stephen P. Martin. A Supersymmetry primer. 1997.

[20] LHCb collaboration. First evidence of the $B_s^0 \to \mu^+\mu^-$ decay. Technical Report LHCB-PAPER-2012-043, CERN, Geneva, Nov 2012.

[21] Jacob Searcy. *Measurement of the top quark pair production cross section in pp collisions 7 TeV in the lepton plus tauChannel with ATLAS*. PhD thesis, University of Oregon, 2012.

[22] Martin L. Perl. The Discovery of the Tau Lepton. Stanford Linear Accelerator Center SLAC-PUB-5937, September 1992.

[23] D0 Collaboration. Search for charged Higgs bosons in top quark decays. *Phys.Lett. B*, 682:278–286, 2009.

[24] The ATLAS Collaboration. Measurement of τ polarization in $W \to \tau\nu$ decays with the ATLAS detector in pp collisions at $\sqrt(s) = 7$ TeV. *Eur.Phys.J.*, C72:2062, July 2012.

[25] Private correspondence with Dr. Robert Cahn and Dr. Maxwell Scherzer, 2013.

[26] K Hagiwara, A Martin, and D Zeppenfeld. Tau Polarization Measurements at LEP and SLC. *Physics Letters B*, 235:198 – 202, 1990.

[27] O Brunin, P Collier, P Lebrun, S Myers, et al. LHC Design Report. CERN, 2004.

[28] Lyndon Evans and Philip Bryant. LHC Machine. *Journal of Instrumentation*, 3(08), 2008.

[29] The ATLAS Collaboration. The ATLAS Experiment at the CERN Large Hadron Collider. *JINST 3*, (S08003), 2008.

[30] *ATLAS detector and physics performance: Technical Design Report.* Technical Design Report ATLAS. CERN, Geneva, 1999.

[31] The ATLAS Collaboration. *Expected performance of the ATLAS experiment: detector, trigger and physics.* Number CERN-OPEN-2008-020. CERN, 2008.

[32] F Djama. Commissioning and operation of the ATLAS Pixel Detector at the CERN LHC collider. *Journal of Instrumentation*, 6(01):C01082, 2011.

[33] The ATLAS Collaboration. Particle Identification Performance of the ATLAS Transition Radiation Tracker. Technical Report ATLAS-CONF-2011-128, CERN, Geneva, Sep 2011.

[34] John David Jackson. *Classical Electrodynamics.* pages 646 to 652. John Wiley and Sons, Inc., 3rd edition, 1999.

[35] John Stupak III. *A Search for First Generation Leptoquarks in 7 TeV pp Collisions with the ATLAS Detector.* PhD thesis, SUNY Stony Brook, 2012.

[36] The ATLAS Collaboration. Expected electron performance in the ATLAS experiment. Technical Report ATL-PHYS-PUB-2011-006, CERN, Apr 2011.

[37] The ATLAS Collaboration. Reconstruction and Calibration of Missing Transverse Energy and Performance in Z and W events in ATLAS Proton-Proton Collisions at 7 TeV. Technical Report ATLAS-CONF-2011-080, CERN, Jun 2011.

[38] The ATLAS Collaboration. Commissioning of the ATLAS high-performance b-tagging algorithms in the 7 TeV collision data. Technical Report ATLAS-CONF-2011-102, CERN, Geneva, Jul 2011.

[39] The ATLAS Collaboration. Determination of the Tau Energy Scale and the Associated Systematic Uncertainty in proton-proton collisions at 7 TeV with the ATLAS detector at the LHC in 2011. Technical Report ATLAS-CONF-2012-064, CERN, Geneva, 2012.

[40] A Höcker, J Stelzer, F Tegenfeldt, H Voss, et al. TMVA - Toolkit for Multivariate Data Analysis with ROOT: Users guide. Technical Report CERN-OPEN-2007-007, CERN, Mar 2007.

[41] Jennifer Godfrey. Using Boosted Decision Trees for Tau Identification in the ATLAS Experiment. Master's thesis, Simon Fraser University, 2009.

[42] Yoav Freund and Robert E. Schapire. A Short Introduction to Boosting. ATT Labs, 1999.

[43] E Barberio, S Bedikian, E Coniavitis, M Dam, E N Dawe, et al. Performance of the Reconstruction and Identification of Hadronic Tau Decays with ATLAS. Technical Report ATLAS-COM-CONF-2011-179, CERN, Geneva, Oct 2011.

[44] S Bedikian, T Bristow, E Coniavitis, M Dam, E N Dawe, et al. Performance of the Reconstruction and Identification of Hadronic Tau Decays in ATLAS with 2011 Data. Technical Report ATL-COM-PHYS-2012-605, CERN, Geneva.

[45] The ATLAS Collaboration. Search for charged Higgs bosons decaying via $H^{\pm} \rightarrow \tau\nu$ in ttbar events using 4.6 fb^{-1} of pp collision data at $\sqrt{s} = 7$ TeV with the ATLAS detector. Technical Report ATLAS-CONF-2012-011, CERN, Geneva, Mar 2012.

[46] The ATLAS Collaboration. Search for charged Higgs bosons through the violation of lepton universality in $t\bar{t}$ events using pp collision data at $\sqrt{s} = 7$ TeV with the ATLAS experiment. Technical Report CERN-PH-EP-2012-347, CERN, Dec 2012.

[47] The ATLAS Collaboration. Data-Quality Requirements and Event Cleaning for Jets and Missing Transverse Energy Reconstruction with the ATLAS Detector in Proton-Proton Collisions at a Center-of-Mass Energy of 7 TeV. Technical Report ATLAS-CONF-2010-038, CERN, Geneva.

[48] The ATLAS Collaboration. Measurement of the $W \to \tau\nu$ Cross Section in pp Collisions at $\sqrt{s} = 7$ TeV with the ATLAS experiment. *Phys.Lett.*, B706:276–294, 2012.

[49] Louis Lyons. *Statistics for Nuclear and Particle Physicists.* Cambridge University Press, 1989.

[50] Louis Lyons, Wade Allison, and Jaime Panella Comellas. Maximum Likelihood or Extended Maximum Likelihood? An Example from High Energy Physics. *Nuclear Instruments and Methods in Physics Research Section A: Accelerators, Spectrometers, Detectors and Associated Equipment*, 245:530 – 534.

[51] Louis Lyons. Discovery or Fluke: Statistics in Particle Physics. *Physics Today*, 65(7):45–51, 2012.

[52] Private correspondence with George Lewis, a HistFactory author, 2012.

[53] Kyle Cranmer, George Lewis, et al. HistFactory: A tool for creating statistical models for use with RooFit and RooStats. Technical Report CERN-OPEN-2012-016, New York University, 2012.

Appendix A

Appendix

Sections A.1 and A.2 of this Appendix follow from Section 8.3. Section A.3 follows from Section 8.6.

A.1 Investigation of Tau ID in W+Jets

A data-driven sample of jets is selected with which to investigate the Tau ID behavior in Υ.

The three Tau ID algorithms, Likelihood(LLH) in Figure A.1, Boosted Decision Tree (BDT) in Figure A.2, and Cut-based in Figure A.3, are each applied to reconstructed τ candidates. The selection is the W+jets signal selection from Table 8.1. The resulting Υ shape and event yield is investigated for the varying types of Tau ID. Samples of reconstructed τ candidates are divided into four mutually-exclusive categories of Tau ID working points:

- Those failing loose Tau ID
- Those passing loose and failing medium Tau ID
- Those passing medium and failing tight Tau ID
- Those passing tight Tau ID

The distribution of reconstructed τ candidates passing tight BDT Tau ID, in Figure A.2 is used as the jets-faking-taus template.

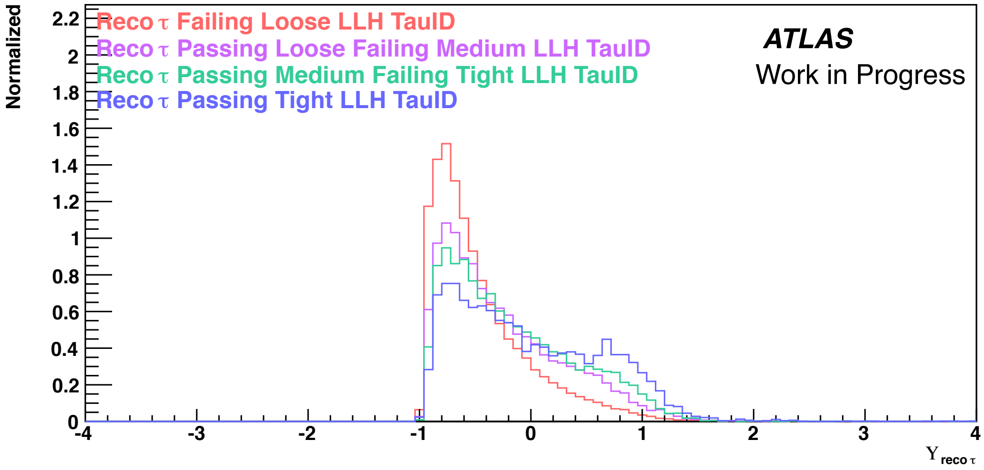

Figure A.1: Reconstructed τ candidates in a W+jets sample of varying tightness LLH Tau ID.

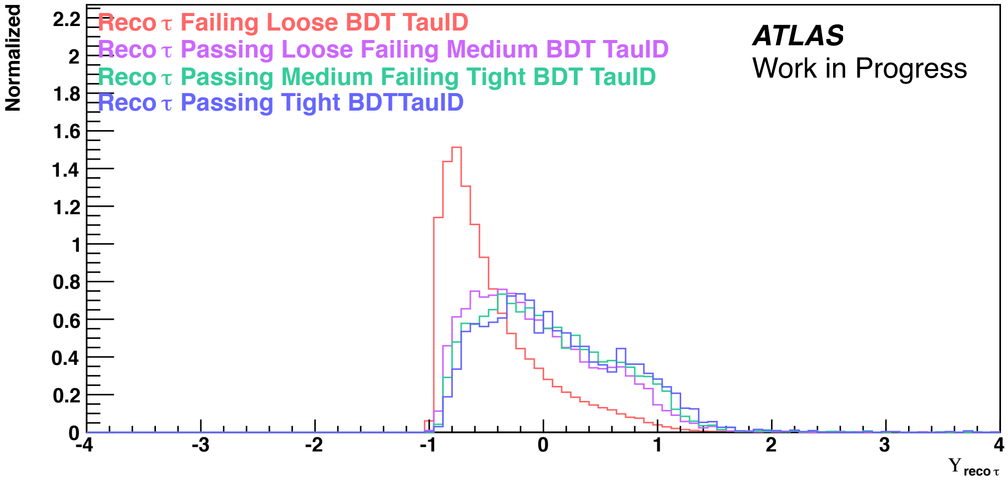

Figure A.2: Reconstructed τ candidates in a W+jets sample of varying tightness BDT Tau ID. The distribution in blue, τ_{reco}s passing tight Tau ID is used as the jets-faking-taus template.

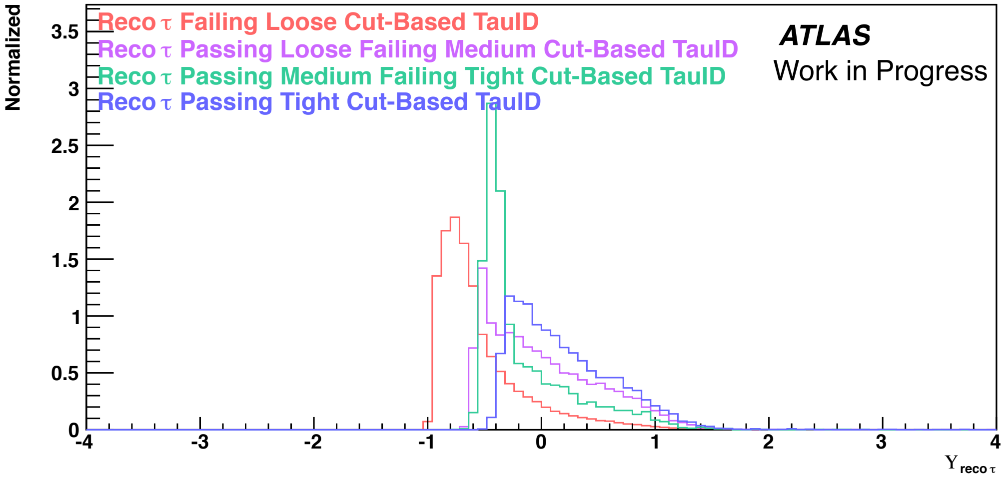

Figure A.3: Reconstructed τ candidates in a W+jets sample of varying tightness cut-based Tau ID.

A.2 Additional Investigations in W+Jets

Additional studies of the Υ observable in W+jets selection with the 4.6 fb^{-1} of 2011 ATLAS data are shown.

The effects of additional cuts on top of the nominal selection, Table 8.1 in Section 8.3.1, are investigated. Figure A.4 shows the effect of a cut on the charge between the μ and τ_{reco}.

The effect of the MET cut in the selection is shown in Figure A.5.

The effect of b-tagging requirements on the selection is shown in Figure A.6.

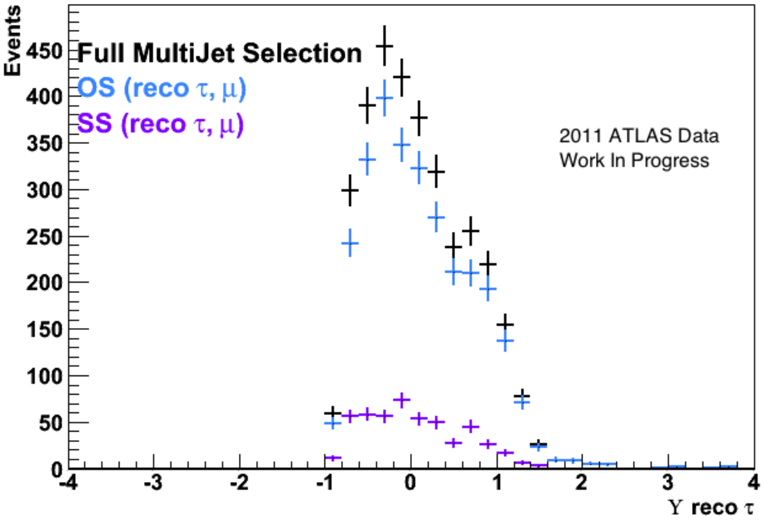

Figure A.4: The Charged Asymmetry distributions of tight BDT τ_{reco}s in events passing the nominal selection (in black) and an additional requirement of charge between the μ and τ_{reco}: opposite sign (OS) in blue, and same sign (SS) in purple, is shown in the data. Note the sum of the OS events and SS events is the total nominal selection. The OS distribution is 85% and the SS distribution is 15% of the nominal selection with exactly 1 τ_{reco} passing tight BDT Tau ID.

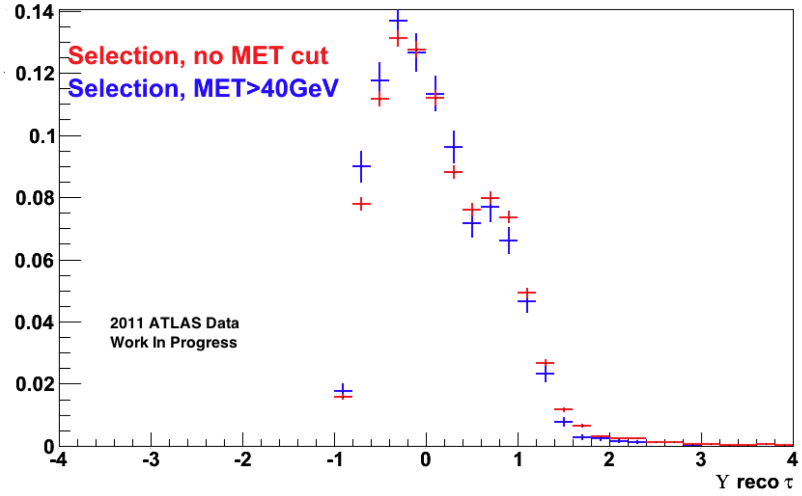

Figure A.5: Charged Asymmetry distributions are shown of τ_{reco}s passing tight BDT Tau ID with and without the MET cut in the W+jets nominal selection. These data-driven jets-faking-taus distributions are normalized to equal areas and show the effect of the MET>40 GeV cut in the nominal selection, Table 8.1. The efficiency of this MET cut is 0.18.

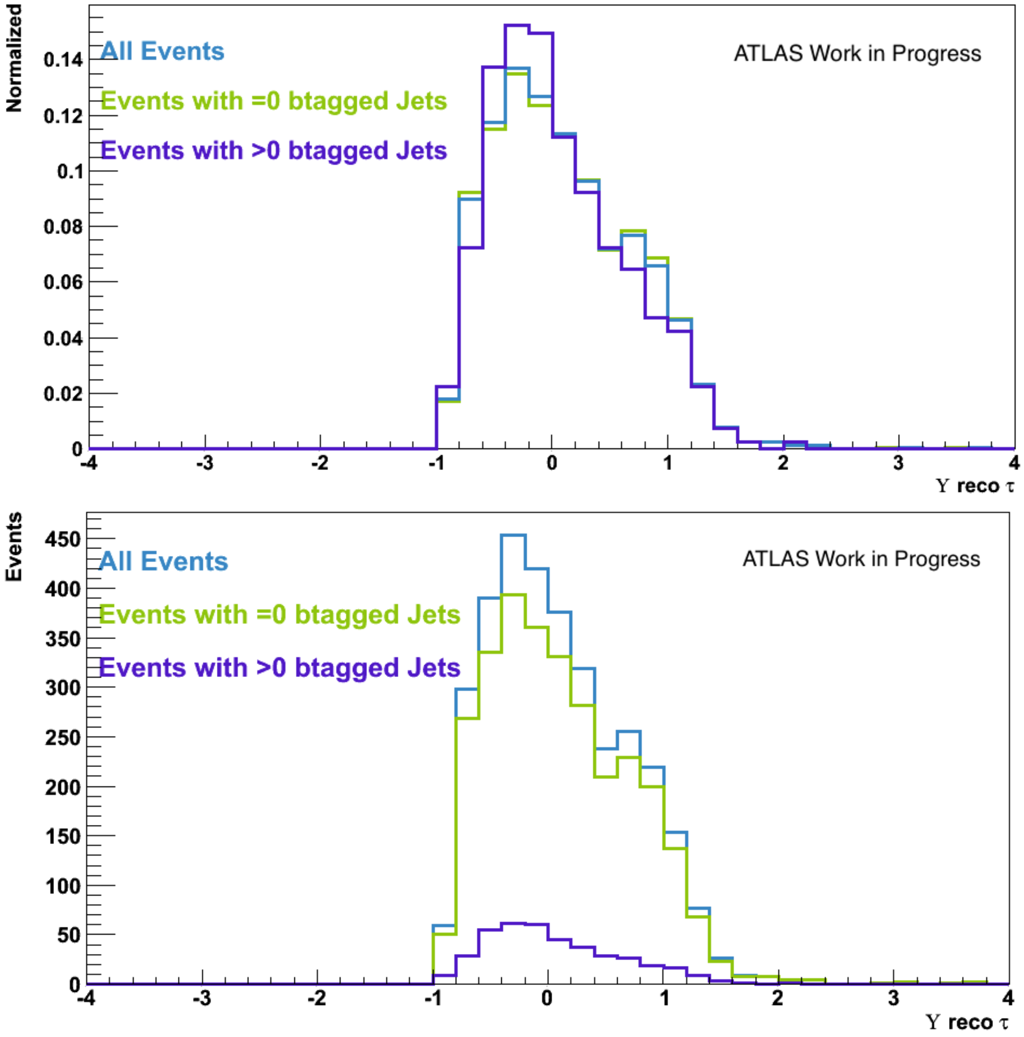

Figure A.6: The Charged Asymmetry distributions in W+jets normalized to equal areas(top) and total events(bottom) is shown in the data. Both distributions have passed the nominal selection and the BDT tight Tau ID. The blue distribution has no requirements on the number of b-tagged jets in the event. The green distribution is of events containing 0 b-tagged jets. The purple distribution is of events containing at least 1 b-tagged jet, indicating a sample with higher $t\bar{t}$ content and possibly a higher content of true τs. The shape Υ remains largely unchanged in the three cases, and the blue distribution is used as the jets-faking-taus template.

A.3 Charged Higgs Content

Following the results of Chapter 8, the Υ templates with the normalization given by extremizing the likelihood function are presented.

The Υ distributions with charged Higgs content with the preferred value of BR($t \rightarrow H^{\pm}b$) = 3% is shown for individual templates in Figure A.7 and templates stacked in Figure A.8. They show that there is room in the fit for a charged Higgs contribution. The result, however, is consistent with the SM.

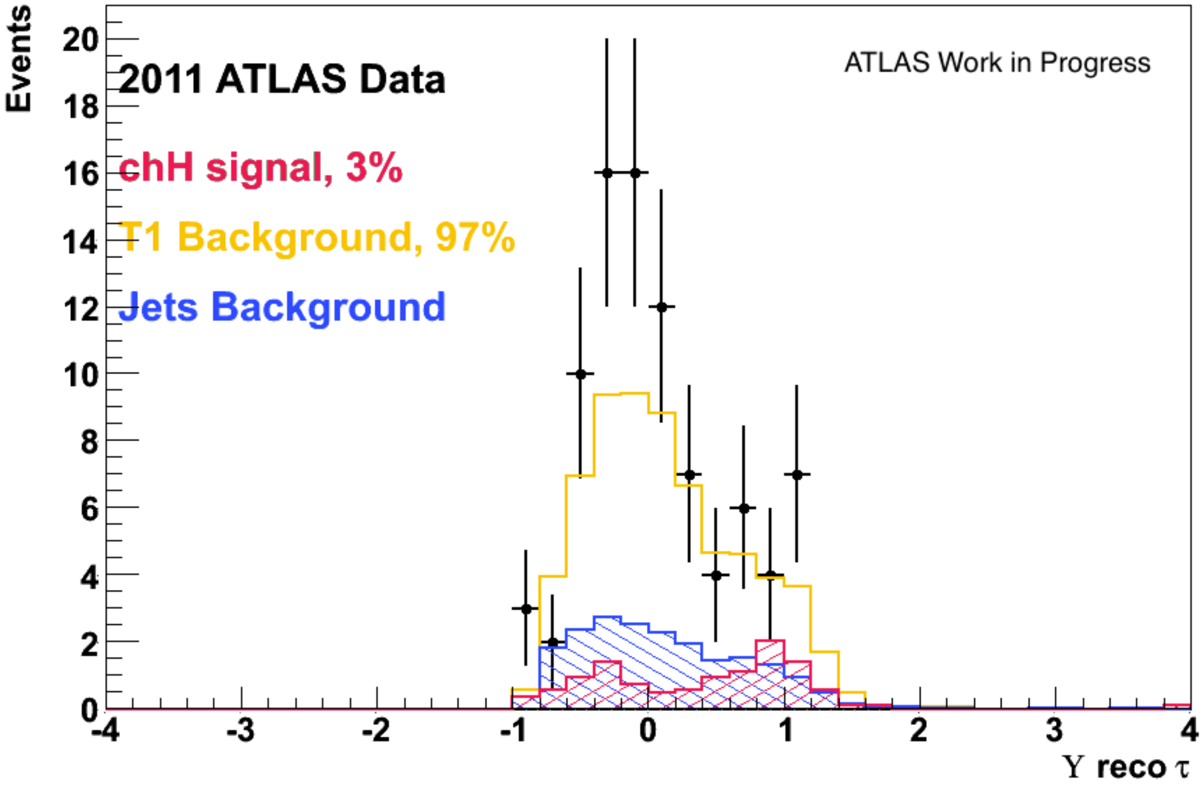

Figure A.7: All templates and data are shown, including normalizations given by the fitting routine result. The likelihood is extremized for the scenario of BR($t \rightarrow Wb$) = 97% ± 7% and BR($t \rightarrow H^{\pm}b$) = 3%, with errors encompassing the SM value of 0%. The result is consistent with the SM scenario.

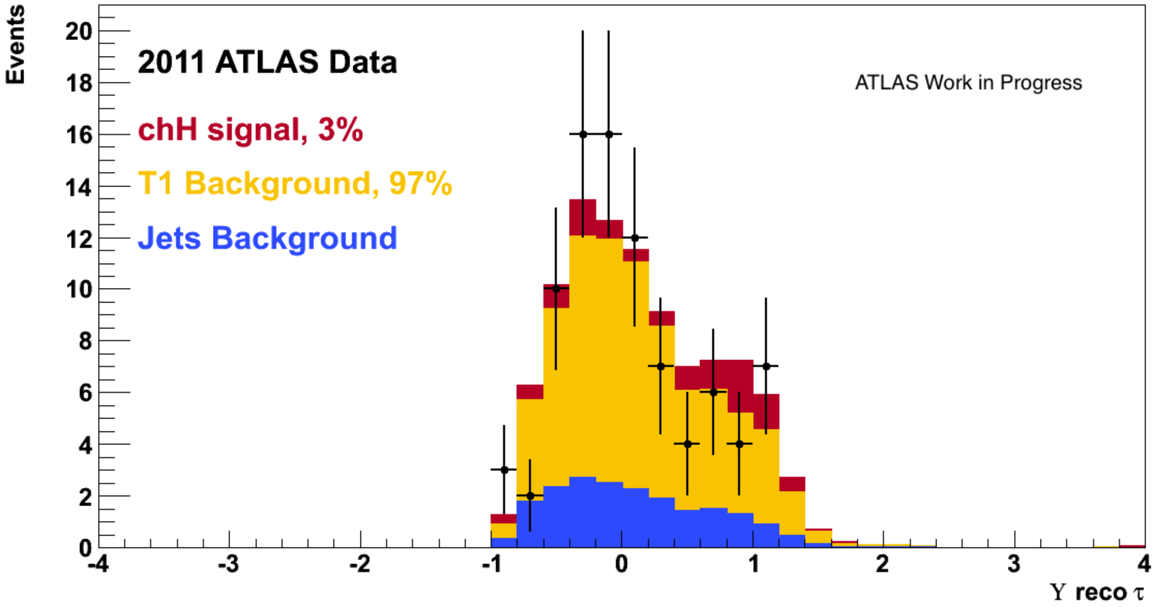

Figure A.8: The resulting shape of the stacked signal and background ϒ templates is shown and compared to ϒ observed in data. The most likely case for the provided templates, is determined by the likelihood extremization, is BR($t \to H^{\pm}b$) = 3%, with errors encompassing the SM value of 0%, and BR($t \to Wb$) = 97% ± 7%. The result is consistent with the SM scenario.